Di Franco

Electrochemical fabrication of metal/oxide/conducting polymer junctions for electronic devices

Ministero dell'Istruzione dell'Università e della Ricerca

Università degli Studi di Palermo
Dottorato in Ingegneria Chimica e dei Materiali

Electrochemical fabrication of metal/oxide/conducting polymer junctions for electronic devices

PhD thesis of **Di Franco Francesco**
SSD **ING-IND/23**

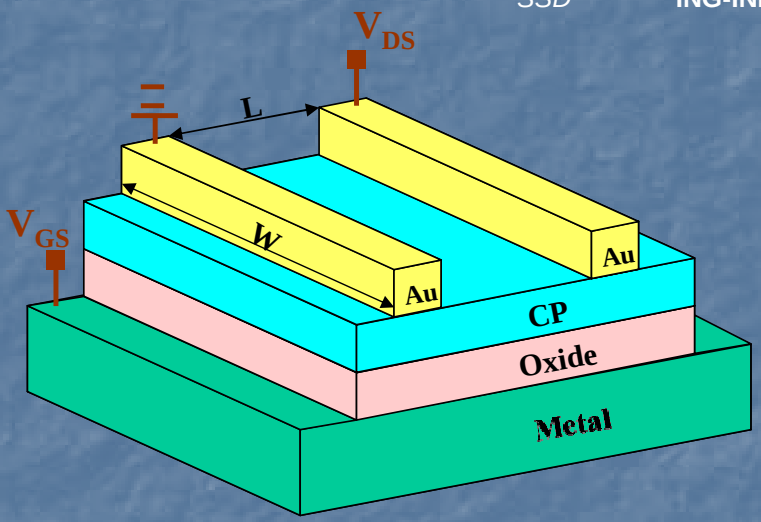

Supervisors
Prof. Monica Santamaria

Prof. Francesco Di Quarto

Head of the PhD board
Prof. Alessandro Galia

2014 - Ciclo XXIV

Electrochemical Fabrication of Metal/Oxide/Conducting Polymer Junctions for electronic devices

PhD Thesis of Francesco Di Franco

SSD ING/IND-23 (Chimica Fisica Applicata)

Supervisors

Prof. Monica Santamaria

_____

Prof. Francesco Di Quarto

_____

Head of the PhD Board

Prof. Alessandro Galia

_____

Contents

1 Synopsis

The metal/oxide/conducting polymer junctions are hybrid inorganic/organic structures usually employed in several electronic devices such as electrolytic capacitor, inorganic-organic thin field effect transistors, organic light emitting diode, sensors and solid state photovoltaic or photo-electrochemical cells [1.1]. This widespread fields of application are mainly due to the possibility to simply modify the electronic properties of conducting polymer, that can show a semiconducting or metallic behaviour depending on the degree of doping. For instance, in solid state electrolytic capacitors, which are passive components in electronic circuits, conducting polymers are used in their metallic state to form a so called Metal/Insulator/Organic Metal junction (MIM_{org}) [1.2], while they work in their semiconducting state in Metal/Oxide/Organic Semiconductor junction (MOS_{org}), to be integrated in Field Effect Transistors, active components of electronic circuits [1.3].

The performances of both electrolytic capacitor and FET are mainly controlled by dielectric properties of the employed oxides. The use of high k material is mandatory in order to get solid state electrolytic capacitor with high specific capacitance, and to reduce the operating voltage of Thin Film Transistor. But, in the same time, it is important to keep very low the leakage current that can have detrimental effects on the dielectric. Promising candidates with high dielectric constant and low leakage current are wide band gap amorphous (no grain boundaries) oxides, more specifically, valve metals oxides, that can easily prepared by anodizing.

This work is focused on the electrochemical fabrication of metal/oxide/conducting polymer junctions to be integrated in electronic devices, i.e. solid state capacitors and thin film transistor. Thus, the first part of the research activity has been devoted to the preparation and physico-chemical characterization of high k oxides with good dielectric properties. We selected anodizing as versatile low temperature wet electrochemical process to grow anodic films of valve metals and valve metal alloys [1.4]. The anodizing of valve metal alloys gives the chance to

prepare mixed oxides, whose electronic properties can be tuned by properly selecting the partner metals and the anodizing conditions (bath compositions, and final voltages). More specifically, we prepared Nb-Ta, Nb-Al and Ti-Si mixed oxides by anodizing the corresponding magnetron sputtered alloys. Al_2O_3 and Ta_2O_5 are wide band gap (6.2 eV and 4.1 eV, respectively) insulator commonly used as dielectric in electrolytic capacitor ($\varepsilon \sim 9$ for alumina and 30 for tantala). In contrast, Nb_2O_5 is a n-type semiconductor with a lower band gap (3.4 eV) but a sensitively higher dielectric constant (~ 57). Thus, Nb-Ta and Nb-Al mixed oxides are anticipated to have properties that lie between those of pure Ta_2O_5 or Al_2O_3 and Nb_2O_5, which suggest that an improvement on the low ε value of Ta_2O_5 and Al_2O_3 and a lowering of the high leakage current of Nb_2O_5 could be achieved.

A high dielectric constant is also reported for titanium oxide (up to 53). However, anodic TiO_2 films develop with a high population density of flaws on high purity titanium in aqueous electrolytes. Previous works have shown that the development of flaws in anodic TiO_2 is associated with crystallization of the film during anodizing. The crystalline regions are reported to enable oxygen evolution, due to their increased electronic conductivity with respect to the amorphous counterpart. The consequent increased pressure can bring to film breakdown, which is detrimental for capacitors. Thus, anodic titanium oxide-based capacitors have not been realized practically despite the large permittivity of the oxide. Several strategies have been proposed in the literature to hinder or delay the onset of crystallization during anodizing of TiO_2. It is widely accepted that the onset of crystallization is delayed by the incorporation of foreign species inside the oxide. These species can be incorporated into the anodic films by alloying to titanium small amount of another element, namely silicon. Therefore, we selected to grow and characterize anodic films on magnetron sputtered Ti-Si alloys.

All the three listed systems, i.e. Nb-Ta, Nb-Al and Ti-Si mixed oxides were characterized by electrochemical, photoelectrochemical and impedance measurements. This in situ characterization, supported by ex situ, Glow Discharge Optical Emission Spectroscopy, X-ray Photoelectron Spectroscopy and Rutherford Back Scattering, allowed getting information on the solid state properties (band gap,

flat band potential, conductivity type, dielectric constant) of the mixed oxides as a function of the base alloy composition and anodizing conditions (formation voltage, growth rate, anodizing solution). Such information, which are of primarily importance in view of possible application of the oxides in electronic devices, resulted to be very useful to assess some theoretical aspects relating to the dependence of the band gap of mixed oxides on their composition as well as to influence of the amorphous nature of the film on their photo-electrochemical behaviour and on their impedance.

In 1997 a correlation between the optical band gap values of crystalline oxides and the square of the electronegativity difference of their constituents was proposed [1.5]. This correlation was extended to mixed oxides, introducing an average cationic electronegativity. Hence, a quadratic dependence of E_g on the oxide composition is predicted. The band gap values estimated for Nb-Ta and Nb-Al mixed oxides were used to test this correlation.

The other important point which was deeply studied pertains to the influence of the amorphous nature on the photo-electrochemical behaviour as well as on the impedance of the investigated anodic films. For amorphous oxides a distribution of allowed localized states inside the mobility gap is expected which has significant effect of the transport properties of the charge carriers generated under irradiation, and strongly influences the response to alternative signals employed to study the impedance of the oxides. Thus, we have described and tested the Braun-Onsager theory to model the transport of photo-carriers in a amorphous inorganic materials, and we have studied the dependence of admittance of the investigated oxides in the frame of the theory of amorphous semiconductor Schottky barrier.

In the second part of this work, the deep knowledge of the solid state properties of the investigated oxides was used to design a photoelectrochemical process able to allow the electropolymerization of Edot on a not conducting substrate. Since we will to prepare oxides with good dielectric properties, i.e. low leakage current, we expect that the electrochemical growth a polymer layer on the investigated films cannot occur. Therefore, we designed a photoelectrochemical polymerization step to allow the growth of the selected conducting polymer, namely PEDOT, on the oxides. This

step was followed by a de-doping process to bring the polymer from its metallic to its p-type semiconducting state to test the performance of the prepared metal/oxide/polymer junction in thin film transistor.

REFERENCES

[1.1] a) M. Muccini, Nature Mater., 5, (2006), 605; b) M.T. Lloyd, Y-J. Lee, R. J. Davis, E. Fang, R. M. Fleming , J. W. P. Hsu, R. J. Kline, M. F. Toney, Journal of Physical Chemistry C, Volume 113, Issue 41, (2009), 17608; c) C. Janáky, C. Visy, Analytical and Bioanalytical Chemistry, 405, (2013), 3489.

[1.2] a) P. Kathirgamanathan, S. Ravichandran, Synth. Met. 74, (1995), 165; b) Y. Kudoh, K. Akami, Y. Matsuya, Synth. Met., 102, (1999), 973; c) Y.T. Ravikiran, M.T. Lagare, M. Sairam, N.N. Mallikarjuna, B. Sreedhar, S. Manohar, A.G. MacDiarmid, T.M. Aminabhavi, Synth. Met., 156, (2006), 1139.

[1.3] a) G. Wang, T. Hirasa, D. Moses, A. J. Heeger, Synthetic Metals, Volume 146, Issue 2, (2004), 127; b) A.-L. Deman, M. Erouel, D. Lallemand, M. Phaner-Goutorbe, P. Lang, J. Tardy, Journal of Non-Crystalline Solids, Volume 354, Issues 15–16, (2008), 1598, c) Björn Lüssem, Max L. Tietze, Hans Kleemann, Christoph Hoßbach, Johann W. Bartha, Alexander Zakhidov, Karl Leo, Nature Communications, 4, (2013), Article number: 2775.

[1.4] L. Young, Anodic Oxide Films, Academic Press, New York, 1961.

[1.5] F. Di Quarto, S. Piazza, C. Sunseri, M.C. Romano, J. Phys. Chem. B, 101, (1997), 2519.

2 Theoretical Background

2.1 Introduction

In this chapter we recall some concepts relating to the characterization of the solid state properties (band gap, flat band potential, conductivity type, dielectric constant) of anodic films grown on valve metal and valve metal alloys by Photocurrent Spectroscopy (PCS) and Differential Admittance measurements. More details about these methods can be found in refs. [2.1-2.4].

2.2 The structure of M/El and SC/El interfaces at the equilibrium

The structure of the metal–electrolyte (M/El) and semiconductor– electrolyte (SC/El) interfaces has been the object of a long series of studies [2.5-2.13]. These concluded that the main differences between the structures of the two electrode–electrolyte interfaces can be traced to the different electronic properties of the electrodes [2.14–2.21]. A brief summary of the subject will be given, in order to introduce some concepts and to derive some equations for use in explaining the electrochemical and photoelectrochemical behavior of such interfaces.

The potential drop across a M/El interface, $\Delta\Phi_{M,el}$, is given by (see Fig. 2.1) :

$$\Delta\Phi_{M,el} = \{\phi_M - \phi_{el}(-x_H)\} + \{(\phi_{el}(-x_H) - \phi_{el}(-\infty)\} \qquad 2.1$$

where ϕ_M and ϕ_{el} represent the Galvani potential in the metal and electrolytic phase, respectively, whilst the notation within the brackets identifies the distance from the metal surface assumed as the origin of the x axis.

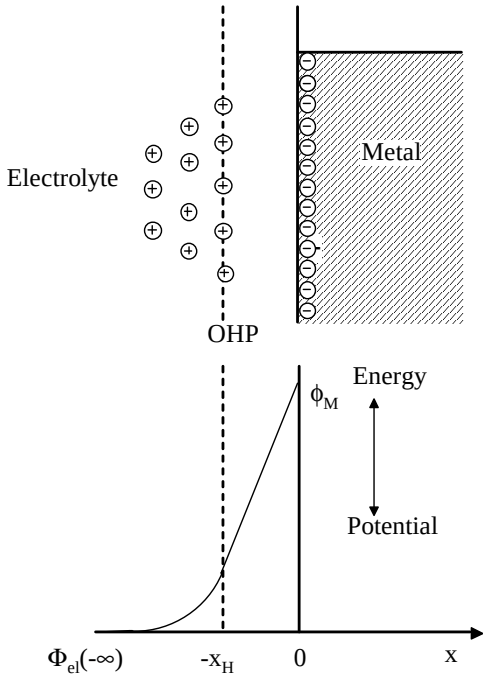

Fig. 2.1 The potential drop across a M/El interface

A positive x direction has been assumed from the surface towards the inner of metal, so that $-x_H$ is the coordinate of the outer Helmholtz plane (OHP). In absence of ions specifically adsorbed this last represents the distance of closest approach of solvated ions in solution to the metal surface. The infinite distance into the solution means simply the bulk of the solution, where the Gouy diffuse layer vanishes. In the previous relationship the Galvani potential in the bulk of the solution is usually assumed as reference potential level, being a physical quantity not accessible experimentally. This difficulty is a general one and it is avoided in electrochemistry by using a reference electrode, respect to which we can measure the Galvani potential drop at any single interface.

This implies that the measured electrode potential, U_E, is really the sum of three Galvani potential drops at the metal/solution, solution/reference electrode and reference electrode/contact metal interfaces [2.22]:

$$U_E = \Delta\Phi_{M,el} + \Delta\Phi_{el,ref} + \Delta\Phi_{ref,M'} \qquad 2.2$$

where the contact metal M' has the same physico-chemical properties of the metal M.

By considering that the Galvani potential drop at a reference electrode is constant, it comes out that any change in the electrode potential, and then any modification in the charge distribution, can be attributed to the M/El interface under study. Moreover, at the electrochemical equilibrium the potential drop at the M/El interface is entirely localized in the solution side, where the excess of ionic charge in the compact double layer (Helmholtz layer) and in the diffuse double layer (Gouy layer) counterbalances the excess of charge (opposite in sign) at the metal surface. In absence of a net circulating current across the interface, an electrical equivalent circuit consisting of two capacitors in series accounts for the electrical behaviour of such an interface [2.5-2.11]. This simple model of interface has been used frequently in studies on the double layer structure at the M/El interface. More refined models of the metal/solution interface have been proposed, and they can be found in refs. [2.12-2.13].

The SC/El interface does not present meaningful differences from the solution side, but it changes drastically from the electrode side, as reported in Fig. 2.2.

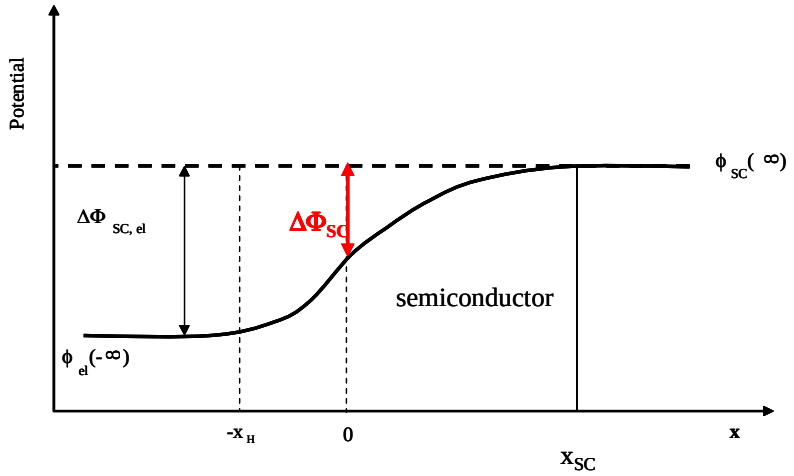

Fig. 2.2 The potential drop across a SC/El interface

In this case a new term in the Galvani potential drop appears, so that we can write :

$$\Delta\Phi_{sc,el} = \{\phi_{sc}(\infty) - \phi_{sc}(0)\} + \{\phi_{sc}(0) - \phi_{el}(-x_H)\} + \{\phi_{el}(-x_H) - \phi_{el}(-\infty)\} \qquad 2.3$$

where the first term in the right hand of eq. 2.3, $\Delta\Phi sc = \{\phi_{sc}(\infty) - \phi_{sc}(0)\}$, represents the potential drop within the SC electrode. At variance with the M/El interface, owing to the much lower concentration of mobile electrical carriers (electrons and holes for n-type and for p-type semiconductors, respectively), a space-charge region is now appearing in the interior of SC phase (see fig. 2.2).

In equilibrium conditions the potential drop inside the semiconductor can be calculated by solving the Poisson equation (see below) under the same conditions used for an ideal M/SC Schottky barrier and by taking into account that the potential drop within the semiconductor is only a part of the total potential difference measured with respect to a reference electrode. Moreover, by taking into account that in presence of a sufficiently concentrated (> 0.1 M) electrolytic solution the potential drop in the Gouy layer is negligible, the equivalent electrical circuit of the interface in electrochemical equilibrium can be represented again by two capacitors

in series: C_{SC}, for the SC space-charge layer, and C_H, for the Helmholtz layer [2.14-2.16]. The value of C_{SC} changes with the width of space-charge region within the semiconductor, x_{sc}, and it is a function of the total potential drop $\Delta\Phi_{sc}$ within the SC.

The hypothesis of absence of surface states at the SC/El interface has been made in order to simplify the analysis. In this case and for not highly doped semiconductors, the total potential drop in the SC space-charge accounts for the variation of electrode potential on going from the flat band potential conditions ($\Delta\Phi_{sc} = 0$) to depletion conditions ($\Delta\Phi_{sc} > 0$ for n-type SCs) when a space charge-region, having width x_{sc}, is formed inside the semiconductor. In the case of p-type material a space-charge layer develops inside the SC for $\Delta\Phi_{sc} < 0$.

2.3 - Determination of space-charge width in crystalline SCs and Mott-Schottky equation

In order to calculate the dependence of x_{sc} on $\Delta\Phi_{sc}$ we need to solve the Poisson equation, which relates the Galvani potential drop at a point x of the space-charge region, $\Phi(x) = \{\phi_{sc}(x) - \phi_{sc}(\infty)\}$, to the charge density inside the semiconductor, $\rho(x)$:

$$\frac{d^2\Phi}{dx^2} = -\frac{\rho(x)}{\varepsilon\varepsilon_0} \qquad 2.4$$

where ρ is the total density of charge (mobile and fixed) inside the space-charge region, ε is the dielectric constant of SC and ε_0 is the vacuum permittivity. The usual boundary conditions of zero electric field and zero Galvani potential in the bulk of semiconductor ($d\Phi/dx(\infty) = 0$ and $\Phi_{sc}(\infty) = 0$) can be assumed. This choice implies that $\Phi_{sc}(x) = \{\phi_{sc}(x) - \phi_{sc}(\infty)\}$ has opposite sign with respect to the electrochemical scale of potential.

The width of the space charge region, x_{sc}, as well as the potential distribution inside the semiconductor under reverse polarization of the SC/El junction can be easily found by using the Schottky barrier model of the junction and by solving the

Poisson eq. 2.4 under depletion approximation and in the hypothesis of homogeneously doped semiconductor with fully ionized donors N_d (for n-type SC) or acceptors N_a (for p-type SC) [2.14-2.16, 2.23]. The depletion approximation implies that the net charge density varies from the zero value of the bulk to the value $+eN_d$ (or $-eN_a$, for a p-type SC) at the depletion edge.

As a consequence of such a charge distribution, a linear variation of the electric field is obtained according to the Gauss equation, which relates the electric field intensity at the surface of the SC, E_s, to the charge density :

$$E_S = \frac{eN_d x_{SC}}{\varepsilon\varepsilon_0} \qquad 2.5$$

For an electric field varying linearly inside the space-charge region, the potential drop inside the SC can be calculated as :

$$\Delta\Phi_{SC} = \frac{E_S x_{SC}}{2} = \frac{\varepsilon\varepsilon_0 E_S{}^2}{2eN_d} \qquad 2.6$$

from which a dependence of E_s on $(\Delta\Phi_{sc})^{1/2}$ is derived.

By relaxing the depletion approximation and by taking into account a more gradual drop of the electron density at the depletion edge, we get for E_s the expression [2.23] :

$$E_S = \left(\frac{2eN_d}{\varepsilon\varepsilon_0}\right)^{1/2}\left(\Delta\Phi_{SC} - \frac{k_B T}{e}\right)^{1/2} \qquad 2.7$$

showing that the depletion approximation differs from the exact one for the thermal voltage contribution k_BT/e.

The dependence of the width of the space-charge region from the potential drop, $\Delta\Phi sc$, can be obtained by using eqs. 2.5 and 2.7 [2.23] :

$$x_{SC} = \left(\frac{2\varepsilon\varepsilon_0}{eN_d}\right)^{1/2}\left(\Delta\Phi_{SC} - \frac{k_B T}{e}\right)^{1/2} \qquad 2.8$$

This expression can be used for deriving also the dependence of the space-charge capacitance from $\Delta\Phi_{sc}$ [2.15, 2.19] :

$$C_{SC} = \frac{\varepsilon\varepsilon_0}{x_{SC}} = \left(\frac{\varepsilon\varepsilon_0 eN_d}{2}\right)^{1/2}\left(\Delta\Phi_{SC} - \frac{k_B T}{e}\right)^{-1/2} \qquad 2.9$$

The previous relationship is the well known Mott-Schottky (M-S) equation, which can be employed to derive the flat band potential, U_{FB}, of the SC/El junction. For this aim we need to relate the Galvani potential drop within the semiconductor to the measured electrode potential, U_E.

By defining the flat band potential of the SC/El junction as the electrode potential at which $\Delta\Phi_{sc} = 0$, in absence of surface states we can write at any other electrode potential :

$$\Delta\Phi_{sc} = U_E - U_{FB} \qquad 2.10$$

where U_E and U_{FB} are measured with respect to the same reference electrode. By substituting eq. 2.10 in eq. 2.9 we get the final form of the M-S equation, usually employed for getting the flat band potential and the energetics of the n-SC/El junction [2.15,2.19] :

$$\left(\frac{1}{C_{SC}}\right)^2 = \left(\frac{2}{\varepsilon\varepsilon_0 eN_d}\right)\left(U_E - U_{FB} - \frac{k_B T}{e}\right) \qquad 2.11$$

The determination of the flat-band potential is the first step in the location of the energy levels at the SC/El interface. Once U_{FB} is known, it is possible to locate the

Fermi level of the SC with respect to the electrochemical scale by means of the relationship $E_F = -|e|U_{FB}$ (rif, abs) (see ref. [2.1]).

2.4 Amorphous Semiconductor Schottky Barrier Theory

In order to understand the main differences in the behaviour of a-SC Schottky barrier (amorphous semiconductor Schottky barrier) with respect to the case of crystalline semiconductor (c-SC) it may be helpful to compare preliminarily the DOS (density of electronic states, N(E)) distribution in both materials (see fig. 2.3).

With respect to the impedance measurements the existence of deep tails of electronic states within the gap has a noticeable influence on the shape of space charge barrier as well as on the frequency response of such barrier [2.24]**.** This is better evidenced in Fig. 2.4 where the energetics of n-type a-SC/El interface is reported, under the simplifying hypothesis of constant DOS and spatially homogeneous material.

The main difference with respect to the case of crystalline SC is that the net space charge depends on both the ionized impurities and the localized states within the mobility gap.

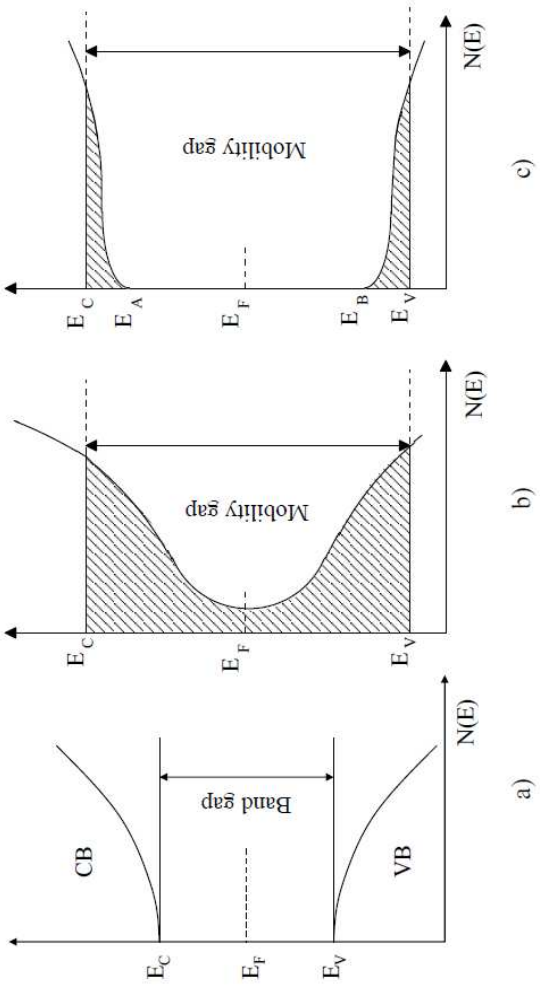

Fig. 2.3 DOS Density of electronic states as a function of energy for amorphous and crystalline semiconductor: (a) crystalline semiconductor; (b) Cohen–Fritzsche–Ovishinsky model; (c) Mott and Davis model. Hatched areas represent the localized gap states, E_C and E_V are the conduction and valence band mobility edges, respectively.

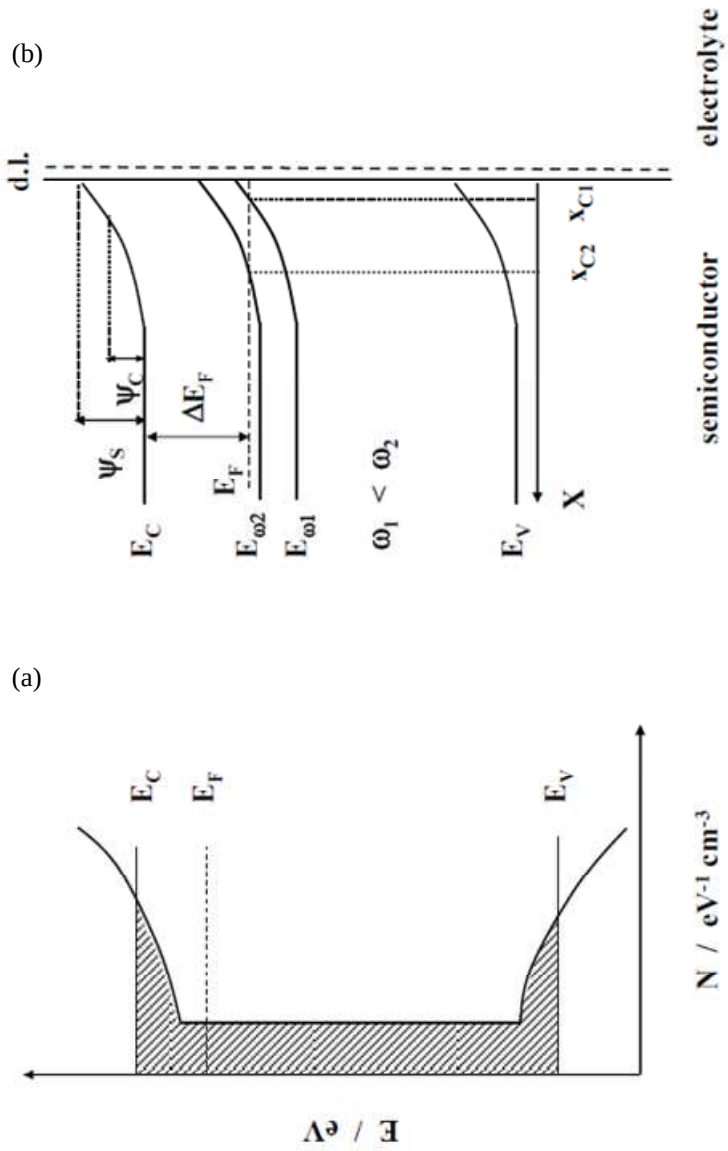

Fig. 2.4 (a) Schematic DOS distribution in a-SC and (b) energetics at an a- SC/El junction. The dashed area evidences localized electronic states.

The electronic states lying into the gap (see Fig. 2.4) do not follow instantaneously the imposed ac signal, but they need a finite response time. This response time depends on their energy position with respect to the Fermi level and it can be much longer than the period of the ac signal having angular frequency ω. In fact an exponential relaxation time, τ, for the capture/emission of electrons from electronic states E below E_F is assumed to hold according to the relationship:

$$\tau = \tau_0 \exp\left(\frac{E_C - E}{k_B T}\right) \qquad 2.12$$

where, at constant temperature, τ_0 is a constant characteristic of each material usually ranging between 10^{-14} - 10^{-10} s. This means that, at constant band bending, with changing frequency the levels which can follow the signal change too. On the other hand, at constant ac frequency, by changing the band bending the more deep levels of depleted region lying below a critical level will not change the occupancy with a.c. signal. According to eq. 2.12, by decreasing the energy of the localized state in the gap, τ increases sharply so that deep states (for which $\omega\tau >> 1$) do not respond to the ac signal.

By assuming a full response for states satisfying the condition $\omega\tau << 1$ and a null response for states having $\omega\tau >> 1$, a sharp cutoff energy level, E_ω, separating states responding from those not responding to the signal, can be defined from the condition: $\omega\tau = 1$, as:

$$E_C - E_\omega = -k_B T \ln(\omega\tau_0) \qquad 2.13$$

According to Fig. 2.4 the intersection of E_ω with the Fermi level of material determines a characteristic point in the barrier, x_C, at which corresponds a band bending ψ_C given by:

$$|e|\psi_C = |e|\psi(x_C) = -k_B T \ln(\omega\tau_0) - \Delta E_F \qquad 2.14$$

where $\Delta E_F = (E_C - E_F)_{bulk}$. x_C is now a distance in the barrier which changes with changing frequency, ω, and band bending ψ_S. In particular, x_C increases with increasing frequency, at constant polarization, or with increasing polarization at constant frequency. From the theory it comes out that the total capacitance is sum of two series contribution coming from the $x < x_C$ and $x > x_C$ regions of the a-SC. The contribution to the conductance comes mainly from the region around $x = x_C$ dividing the total response from null response regions. In the hypothesis of a constant DOS the total capacitance is given by the sum of the two contributions:

$$\frac{1}{C(\psi_S,\omega)} = \frac{1}{C(\psi_C,0)} + \frac{x_C}{\varepsilon\varepsilon_0} \qquad 2.15$$

where $C(\psi_C,0) = \sqrt{\varepsilon\varepsilon_0 e^2 N}$ and $x_C = \sqrt{\frac{\varepsilon\varepsilon_0}{e^2 N}} \ln\frac{\psi_S}{\psi_C}$. After substitution the following relationship is obtained for the total capacitance:

$$C_{LBB}(\psi_S,\omega) = \sqrt{\varepsilon\varepsilon_0 e^2 N}\left(1 + \ln\frac{\psi_S}{\psi_C}\right)^{-1} \qquad 2.16$$

whilst the parallel conductance of the junction is given by:

$$G_{LBB}(\psi_S,\omega) = \frac{\omega\pi kT}{2}|e|\psi_C\sqrt{\varepsilon\varepsilon_0 e^2 N}\left(1 + \ln\frac{\psi_S}{\psi_C}\right)^{-2} \qquad 2.17$$

The analytical solutions for the admittance components of the junction have been derived under conditions that $\psi_S > \psi_C \geq 3k_BT/e$ and at not too high band bending (Low Band Bending regime, $e\psi_S < (E_g/2 - \Delta E_F)$ [2.25-2.29 and refs. therein]

It has been shown that $G(\psi_S, \omega)$ has a spectroscopic character with respect to the distribution of electronic states within the gap, whilst variations in DOS cause only minor changes in the $C(\psi_S, \omega)$ vs potential plots provided that the DOS varies

little over an energy range of k_BT. In previous equations ε_0 is the vacuum permittivity, e the absolute value of the electronic charge, ε the film dielectric constant and ψ_S the potential drop inside the a-SC as above.

In high band bending region, i. e. for $\psi_S > V_g = (E_g/2 - \Delta E_F)/e$, when a deep depletion region at the surface of a-SC/El junctions appears, according to refs. [2.30-2.32] (see Fig. 2.5) the total capacitance of barrier can be modelled as a two series capacitance:

$$\frac{1}{C(\psi_S,\omega)} = \frac{1}{C(\psi_g,\omega)} + \frac{x_g}{\varepsilon\varepsilon_0} \qquad 2.18$$

where the first term of eq. 2.18 represents the low band bending contribution calculated at the electrode potential where the Fermi level crosses the mid gap energy and coincides with eq. 2.15 after notation substitution. The second term represents the capacitance of the deep depletion region going from the surface to the point x_g of the junction (see Fig. 2.5), where a parabolic potential distribution exists, and is frequency independent.

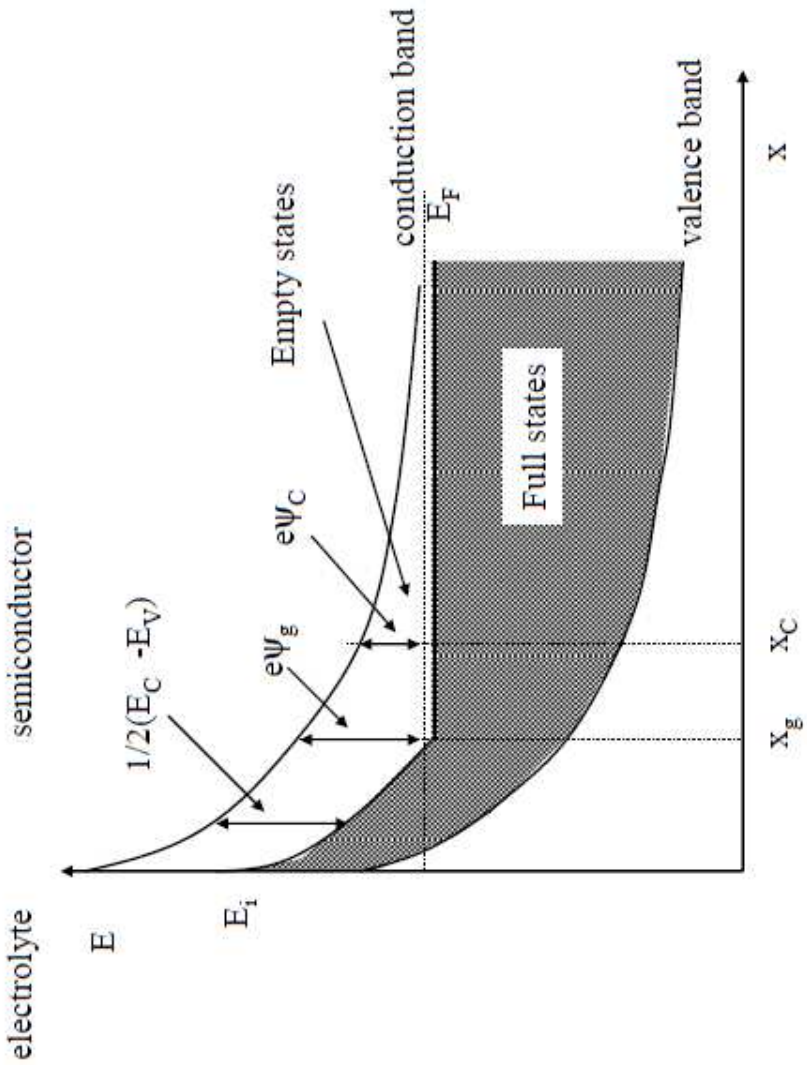

Fig. 2.5 Energy band diagram for an a-SC Schottky barrier under depletion conditions in the high band-bending region.

In the hypothesis of constant DOS an analytical expression has been derived for x_g by Da Fonseca et al. [2.33], which allows to get the following analytical expression for the total capacitance:

$$\frac{1}{C_{HBB}(\omega,\psi_S)} = \frac{1}{\sqrt{\varepsilon\varepsilon_0 e^2 N}}\left(\ln\frac{\psi_g}{\psi_C} + \sqrt{1+\frac{2}{\psi_g}\left(\psi_S-\psi_g\right)}\right) \qquad 2.19$$

It comes out from eq. 2.19 that at high band bending the capacitance changes as the square root of the band bending as soon as the term $2\,\psi_S/\psi_g$ becomes much higher than 1. If this occurs a square root dependence from electrode potential can appear in the capacitance behaviour which could account for the M-S like behaviour observed, sometimes, for a-SC/El junctions at high band bending.

Under the hypothesis of constant DOS, N(E) = N, it is also straightforward to derive from the general expression of $G(\psi_S, \omega)$, [see refs. 2.31-2.32] the following equation for the conductance of the barrier [2.25]:

$$G_{HBB}(\omega,\psi_S) = \pi^2 f\frac{kT}{|e|\psi_C}\sqrt{\varepsilon\varepsilon_0 e^2 N}\left(\ln\frac{\psi_g}{\psi_C} + \sqrt{1+\frac{2}{\psi_g}\left(\psi_S-\psi_g\right)}\right)^{-2} \qquad 2.20a$$

More generally for non constant DOS :

$$G_{HBB}(\omega,\psi_S) = \pi^2 f\frac{kT}{|e|\psi_c}\sqrt{\varepsilon_0\varepsilon_r e^2 N_{av}}\frac{N(E_F-e\psi_C)}{N_{av}}\left[\ln\frac{\psi_g}{\psi_c} + \sqrt{1+\frac{2}{\psi_g}\left(\psi_s-\psi_g\right)}\right]^{-2} \qquad 2.20b$$

Eqs. 2.19 and 2.20 have been derived under the same conditions valid for the LBB expression and they coincide with the previous ones for $\psi_S \leq \psi_g$.

2.5 Photocurrent vs. potential curves for crystalline SC/El junctions: the Gärtner-Butler model

The first attempt to model the photocurrent behaviour of a SC/El junction under illumination can be ascribed to M.A. Butler [2.34], who adapted a previous model developed by Gärtner for the M/SC Schottky barrier [2.35] to the case of a SC/El interface. A close similarity between the Schottky barrier junction and the SC/liquid interface was assumed in the model. The quantitative fitting of the experimental photocurrent *vs* potential curves for n-type single crystal WO_3/electrolyte junction under monochromatic irradiation, performed through the Butler-Gärtner model, attracted the attention of many electrochemists, who devised in the Butler-Gärtner mathematical treatment an alternative way to get the flat band potential of the junction, circumventing some of the difficulties related to the M-S analysis. In this section we will derive the theoretical expressions for the photocurrent in a crystalline SC/El junction as a function of the electrode potential in the frame of the Gärtner-Butler model. The results will be used for getting also the relationship between band gap of photoelectrodes and quantum efficiency of the junction at constant potential.

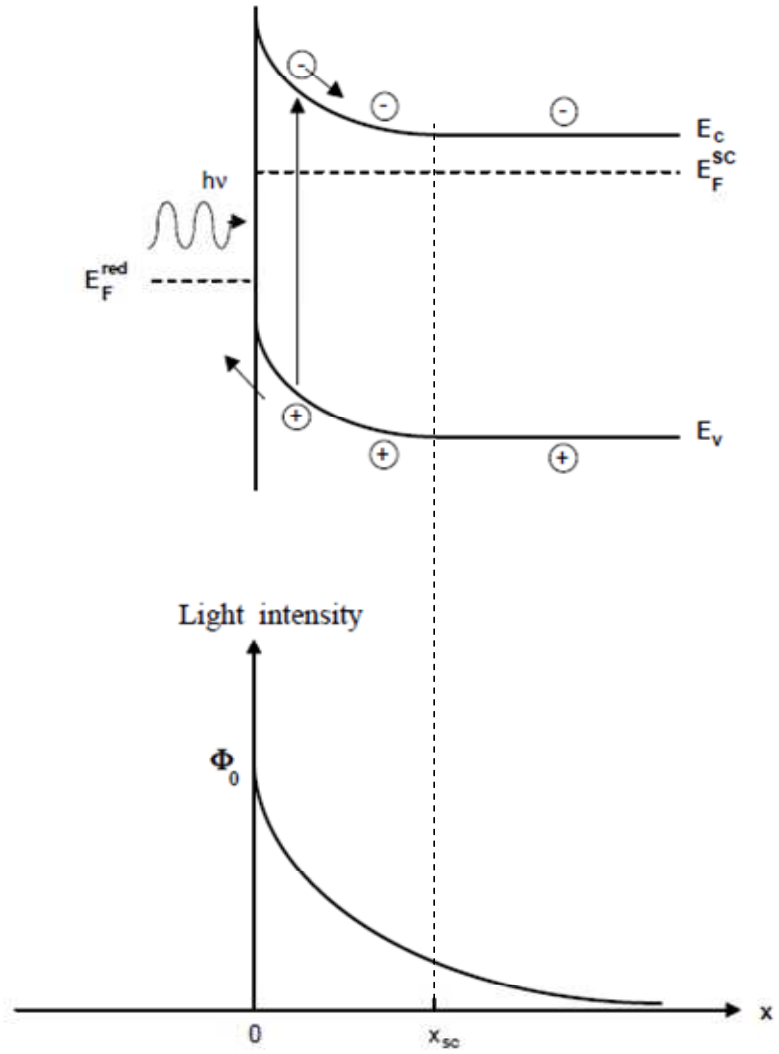

Fig. 2.6 Schematic representation of a crystalline n-type SC/El interface under Illumination.

In Fig. 2.6 we report a schematic picture for a crystalline n-type SC/El interface under illumination. In the figure, Φ_0 (in cm^{-2} sec^{-1}), is the photon flux entering the

semiconductor (corrected for the reflections losses at the SC/El interface) which is absorbed following the Lambert-Beer law. According to this, the number of electron-hole pairs generated per second and unit volume at any distance from the SC surface, g(x), is given by :

$$g(x) = \Phi_0 \, \alpha \, e^{-\alpha x} \qquad 2.21$$

where α, the light absorption coefficient of the semiconductor, is a function of the irradiating wavelength. It is assumed that each absorbed photon (having energy, $h\nu$, higher than the optical band gap of the semiconductor photoelectrode, E_g) originates a free electron-hole couple.

In the Gärtner model the total photocurrent collected in the external circuit is calculated as the sum of two terms: a migration term, I_{drift}, which takes into account the contribution of the minority carriers generated into the space-charge region, and a diffusion term, I_{diff}, arising from the minority carriers entering the edge of the space- charge region from the field free region ($x > x_{SC}$). No reflections of light at the rear interface is assumed, so that all the entering light is absorbed within the SC.

Moreover, in the model it is assumed that minority carriers generated in the space-charge region of the SC do not recombine at all, owing to the presence of an electric field which separates efficiently the photogenerated carriers. The same assumption is made for the minority carriers arriving at the depletion edge from the bulk region of the SC. In order to calculate I_{diff}, Gärtner solved the transport equation, which for a n-type SC is :

$$\frac{dp(x)}{dt} = D_p \frac{d^2p(x)}{dx^2} - \frac{p - p_0}{t} + g(x) \qquad 2.22$$

with the boundary conditions: p = p0 for $x \rightarrow \infty$ and p = 0 for $x = x_{SC}$. In eq. 2.22, p is the hole concentration under illumination, p_0 the equilibrium concentration of hole in the bulk of the (not illuminated) SC and Dp the diffusion coefficient of the

holes. The zero value for p at the boundary of the depletion region comes out from the previous assumption that all the holes generated into the space-charge region are swept away without recombining. According to Gärtner, for the total photocurrent we can write :

$$I_{ph} = I_{drift} + I_{diff} = e\int_0^{x_{SC}} g(x)dx + eD_p\left[\frac{dp(x)}{dx}\right]_{x=x_{SC}} \qquad 2.23$$

where e is the absolute value of the electronic charge. By solving eq. 2.22 in the steady-state approximation for getting out the distribution of holes in the field free region, and by substituting eq. 2.21 for g(x) in the integral of the drift term, we get finally the Gärtner equation for a n-type semiconductor [2.35] :

$$I_{ph} = e\Phi_0\left[\frac{1-\exp(-\alpha x_{SC})}{1+\alpha L_p}\right] + ep_0\frac{D_p}{L_P} \qquad 2.24$$

where L_p is the hole diffusion length. The same equation holds for p-type SCs, with D_n and L_n (electron diffusion coefficient and diffusion length, respectively) instead of D_p and L_p, and n_0 (electrons equilibrium concentration) instead of p_0.

Eq. 2.24 was further simplified by Butler for the case of wide band gap SCs (e.g., n-type WO_3), where the concentration of minority carriers into the bulk, p_0, is very small. In this case, by using also eq. 2.8 for x_{SC}, he derived the Gärtner-Butler equation for the photocharacteristics of a crystalline SC/El junction [2.34] :

$$I_{ph} = e\Phi_0\left[1-\frac{\exp\left(-\alpha x_{SC}^{\,0}\sqrt{\Delta\Phi_{SC}-\frac{k_bT}{e}}\right)}{1+\alpha L_p}\right] \qquad 2.25$$

In this equation, x_{SC}^{0} represents the space-charge width into the SC electrode at 1 V of band bending, and $\Delta\Phi_{sc} = (U_E - U_{FB})$. It is easy to show [2.34] that if $\alpha x_{sc} << 1$ and $\alpha L_p << 1$, the photocurrent crossing the n-type SC/El interface can be written as :

$$I_{ph} = e\Phi_0 \alpha x_{SC}^0 \left(U_E - U_{FB} - \frac{k_b T}{e} \right)^{1/2} \qquad 2.26$$

Eq. 2.26 foresees a quadratic dependence of the photocurrent on the electrode potential, which can be used for getting the flat band potential. In fact, neglecting the thermal voltage, a plot of $(I_{ph})^2$ *vs* U_E will be a straight-line which intercepts the voltage axis at the flat band potential, U_{FB}.

By considering also the relationship between the absorption coefficient and band gap of material, E_g, valid in the vicinity of the optical absorption threshold [2.19] :

$$\alpha = A \frac{\left(h\nu - E_g \right)^{n/2}}{h\nu} \qquad 2.27$$

with n depending on the kind of the optical transition between occupied electronic states and vacant states of the semiconductor, from Butler eq. 2.26 it is possible to derive the following expression for the quantum yield :

$$\frac{I_{ph}}{e\Phi_0} = \eta h\nu = A\left(h\nu - E_g \right)^{n/2} \left(L_i + x_{SC}^0 \sqrt{\left(\left| U_E - U_{FB} \right| \right)} \right) \qquad 2.28$$

In the previous equation η represents the collection efficiency, E_g the optical threshold for the onset of photocurrent of the electrode and $L_i = L_p$ or L_n for n-type or p-type SC, respectively. From eq. 2.28 it is possible to get the optical band gap of the material from the photocurrent dependence on the wavelength (usually referred

as the photocurrent spectrum of the junction in the photoelectrochemical literature), by plotting $(\eta h\nu)^{2/n}$ *vs* $h\nu$ at constant electrode potential (U_E-U_{FB} = const).

2.6 Photocurrent vs. potential curves for amorphous anodic film/electrolyte junctions

Like for the electronic properties, the amorphous nature affects considerably also the optical properties of materials. The main differences in the photocurrent response of disordered thin anodic films with respect to the case of bulk crystalline semiconductors arise from the following facts.

a) The optical band gap of an amorphous material may coincide or not with that of the crystalline counterpart, depending on the presence of different types of defects which can modify the DOS distribution (see fig. 2.3).

b) At variance with crystalline materials, the generation process of free carriers by the absorption of photons having energy equal or higher than the optical band gap of the film may depend on the electric field, owing to the presence of an initial (geminate) recombination.

c) The presence of reflecting metal/film and film/electrolyte interfaces makes it possible the onset of multiple reflections, even for photons having energy higher than the optical absorption threshold; this fact originates interference effects in the photocurrent *vs* film thickness curves.

d) The small thickness of the film does make possible the optical excitation at the inner metal/film interface, which can inject photocarriers from the underlying metal into the VB or CB of the anodic film (internal photoemission), or directly into the electrolyte (external photoemission) in the case of very thin films (1-2 nm thick).

2.6.1 Optical gap in amorphous SCs

As for the first point, we recall the relationship between light absorption coefficient and optical band gap of material, E_g, valid near the optical absorption threshold [2.19, 2.36]:

$$\alpha h\nu = A\left(h\nu - E_g\right)^{n/2} \qquad 2.29$$

where, for crystalline materials, n can assume different values depending on the nature of the optical transitions between occupied electronic states of the VB (Valance Band) and vacant states of the CB (Conduction Band). The optical transitions at energies near the band gap of a crystalline material may be direct or indirect: in the first case no intervention of other particles are required, apart the incident photon and the electron of the VB; in the second case the optical transition is assisted by the intervention of lattice vibrations.

By assuming a parabolic DOS distribution ($N(E) \propto E^{1/2}$) near the band edges, in the case of direct transitions n assumes values equal to 1 or 3, depending on whether the optical transitions are allowed or forbidden in the quantum mechanical sense [2.19]. In the case of indirect optical transitions the value of n in eq. 2.29 is equal to 4 [2.19].

In the case of amorphous materials, owing to the relaxation of the k-conservation selection rule, "no intervention of phonons is invoked to conserve momentum and all energy required is provided by the incident photons" [2.36]. By assuming again a parabolic DOS distribution in the vicinity of the mobility edges of both the conduction and valence band (above E_c and below E_v, with reference to Fig. 2.3) it has been shown [2.37] that the following relationship holds :

$$\alpha h\nu = \text{const}\left(h\nu - E_g^m\right)^2 \qquad 2.30$$

where E_g^m = E_c - E_v is the mobility gap of the a-SC. The exponent 2 is reminiscent of the indirect optical transitions in crystalline material but now photons interact with the solid as a whole: this type of transition in amorphous materials is termed non-direct.

Because some tailing of states is theoretically foreseen for a-SC by every proposed model of DOS, E_g^m represents an extrapolated rather then a real zero in the density of states.

In the presence of a DOS distribution varying linearly with energy in the ranges E_C-E_A and E_B-E_V of Fig. 2.3c, it is still possible to get a similar expression of the absorption coefficient [2.36] :

$$\alpha h\nu = \text{const}\left(h\nu - E_g^{opt}\right)^2 \qquad 2.31$$

where E_g^{opt} now represents the difference of energy (E_A-E_v) or (E_c-E_B) in Fig. 2.3c, whichever is the smaller, and the constant assumes values close to 10^5 eV^{-1} cm^{-1}. The range of energy in which eq. 2.31 should be valid is in the order of 0.3 eV or less [2.36].

In order to distinguish between these two different models of optical transitions, giving both the same dependence of the absorption coefficient on the photon energy, we will refer to the first one as the Tauc approximation for the calculation of the SC mobility gap and to the second one as the Mott-Davis approximation for the SC optical gap. When the $(\alpha h\nu)^{0.5}$ *vs* $h\nu$ plots display a linear region larger than 0.3 eV it seems more correct to interpret the data on the basis of the Tauc model of optical transitions.

In the case of anodic films on valve-metals, the so-called Urbach tail for the absorption coefficient is frequently observed for photon energies lower than the mobility gap, which follows the law :

$$\alpha = \alpha_0 \exp\left(- \gamma \frac{E_0 - h\nu}{k T} \right) \qquad 2.32$$

with γ and α0 constant. Such a relationship, which has been found to hold for crystalline materials too, has been rationalized in the case of amorphous SCs by assuming an exponential distribution of localized states in the band edge tails [2.38].

In interpreting the information provided by the optical gap values, it is important to recall the statement reported in Mott-Davis book [2.36]: "A general rule appears to be that, if the local atomic order is not appreciably altered in the amorphous phase, the gaps in the two states (amorphous and crystalline) are not appreciably different". This rule works better for materials whose band structure is mainly determined by the nearest-neighbour overlap integral (tight-binding materials). The difference E_g^{am} - E_g^{cryst} is in the range of 0.1 - 0.35 eV, in agreement with the extension of the localized states regions near the band edges due to the lattice disorder. Moreover, by taking into account that a value of E_0 nearly coincident with the mobility gap has been frequently derived from the Urbach plot, it seems quite reasonable to suggest for such a class of amorphous materials a band model similar to that shown in Fig. 2.3b, with an exponentially decreasing DOS in the mobility gap of the films at energies lying below E_c and above E_v.

A mobility gap of the amorphous anodic film lower than the band gap of the crystalline counterpart must be interpreted as an indication that differences are present between the short-range order of the two phases. A different short-range order can imply the formation of a defective structure, with a high density of localized states within the mobility gap as well as changes in the density of the anodic film, which is known to affect also the value of the optical gap in amorphous materials [2.36, 2.37, 2.39, 2.40].

2.6.2 Photoemission phenomena at the metal/anodic film interface

In this section we discuss the role of the inner metal/film interface in the generation processes under illumination for thin anodic films. In this case, regardless of the wavelength of the incident light, a large fraction of photons impinging the oxide/solution interface arrive at the metal/film interface, where the electrons in the metal surface can be excited to higher energy levels leaving vacant states below the Fermi level of the metal. The fate of the excited states into the metal depends on the occurrence of different physical deactivation processes at this interface. Apart the thermal deactivation by scattering of excited electrons with the lattice vibrations, photoemission phenomena of the excited photocarriers of the metal can be observed.

In the case of very thin anodic films ($d_{ox} \leq 2$ nm) external photoemission processes become possible, by tunnelling of the electrons or holes excited at the metal surface throughout the film. Although a hole photoemission process has been suggested years ago in the case of a gold electrode covered with a very thin oxide [2.41], the photoemission of electrons directly from the metal to the ground state of liquid water has been observed more frequently through very thin oxide films covering metals [2.42-2.44]. When such an external photoemission process occurs in absence of diffuse double layer effects or adsorbed large molecules, it has been shown that the emission photocurrent from the metal to the acceptor species in solution depends on both the photon energy and the electrode potential according to the so-called "5/2 power law" [2.45] :

$$I_{ph} \propto \left(h\nu - h\nu_0 - eU_e\right)^{5/2} \qquad 2.33$$

where U_e is the electrode potential measured with respect to a reference electrode and $h\nu_0$ is the photoelectric threshold at $U_e = 0$. From eq. 2.33 it comes out that the photoelectric threshold changes with the reference electrode. By extrapolating to $I_{ph} = 0$ the plot of $(I_{ph})^{0.4}$ as a function of the electrode potential, under irradiation with light at a fixed wavelength, we can derive the photoelectric

threshold $h\nu_0 = h\nu - eU^*(ref)$, where U*(ref) is the intercept potential measured with respect to the reference electrode employed.

In the case of thicker films ($d_{ox} \geq 5$ nm), where the external photoemission processes are forbidden owing to a very low probability of tunnelling through the film, the possibility of an internal photoemission due to the injection of photoexcited electrons (or holes) from the metal into the CB (or VB) of the anodic film must be considered. In such evenience the internal photocurrent emission varies with the photon energy according to the so-called Fowler law [2.45, 2.46] :

$$I_{ph} = \text{const} \left(h\nu - E_{th}\right)^2 \qquad 2.34$$

where E_{th} is the internal photoemission threshold energy, which can be obtained from a plot of $(I_{ph})^{0.5}$ *vs* the photon energy. This threshold is a measure of the distance in energy between the Fermi level of the metal and the edge of the film CB (electron photoemission) or VB (hole photoemission). The occurrence of electron or hole internal photoemission in the case of insulating films is established by the direction of the electric field, and in turn by the electrode potential value with respect to the inversion photocurrent potential. In absence of trapping effects, the inversion photocurrent potential can be used to determine the flat band potential of insulating anodic films.

Obviously, eqs. 2.33 and 2.34 can be referred also to the photoemission yield $(I_{ph}/e\Phi_0)$.

In the case of insulating anodic films on valve-metals internal electron photoemission processes are usually observed under cathodic polarization and under illumination with photons having energy lower than the optical band gap of the film [2.42,2.44].

2.6.3 A photocurrent expression for the a-SC/El junction

Due to the low mobility of carriers in amorphous materials it is reasonable to assume that a negligible contribution to the measured photocurrent arises from the field- free region of the semiconductor. In this case it is quite easy to derive an expression for the migration term in the space-charge region of the a-SC, in a quite similar way to that followed by Gärtner.

Like in the Butler model, we will assume the absence of kinetic control in the solution and a negligible recombination rate at surface of the semiconductor. The limits of validity of such assumption have been discussed in the literature for the case of crystalline SC/El junctions [2.47] and they will not be repeated here. Initially we will assume also an unitary efficiency of free carriers generation ($\eta_g = 1$) under illumination with light having energy higher than the SC mobility gap; then we will relax such an assumption in discussing the behaviour of particular systems.

In steady-state conditions the recombination of photogenerated carriers in the space-charge region can be taken into account by assuming that the probability of any carrier photogenerated at a position x to leave the space-charge region is given by [2.48] :

$$P(x,\overline{E}) = \exp\left(-\frac{x}{L_d}\right) \qquad 2.35$$

where $\overline{E}$ is the mean electric field in the space-charge region of the a-SC and L_d is the drift length of the photocarriers ensemble in the average field approximation, given by :

$$L_d = \mu\tau\overline{E} \qquad 2.36$$

μ and τ being the drift mobility and the lifetime of the photocarriers, respectively. According to these equations and to the assumptions made, we can write :

$$I_{ph} \equiv I_{drift} = e\Phi_0 \int_0^{x_{SC}} \alpha \exp(-\alpha x) P(x, \overline{E}) dx \qquad 2.37$$

where Φ_0 is the photon flux corrected for the reflection at the electrolyte/film interface, having assumed negligible reflections at the film/metal interface. By integration of eq. 2.37 we get [2.48] :

$$I_{ph} = e\Phi_0 \frac{\alpha L_d}{1+\alpha L_d}\left[1 - \exp\left(-x_{SC}\frac{1+\alpha L_d}{L_d}\right)\right] \qquad 2.38$$

From eq. 2.38 it follows a direct proportionality between the photocurrent and the absorption light coefficient for $\alpha L_d >> 1$ and $\alpha x_{SC} << 1$, as previously derived for crystalline materials (see eq. 2.26). On the other hand for $\alpha L_d << 1$ still a direct proportionality between I_{ph} and α is assured by the fractional term $\alpha L_d/(1+\alpha L_d)$. According to these considerations, we can still assume as valid for amorphous SCs a direct proportionality between the photocurrent yield, $I_{ph}/e\Phi_0$, and the light absorption coefficient, α, in the vicinity of the absorption edge. Like for crystalline materials, this allows to replace α with the photocurrent yield in eqs. 2.30 to 2.32, relating the absorption coefficient to the optical band gap, and to derive the optical band gap of amorphous semiconducting films from the photocurrent spectra.

A major aspect to take into account in the formulation of the transport equations of the photocarriers is related to the possible presence of geminate recombination effects in the generation of mobile photocarriers. This phenomenon occurrs generally in any material where the photogenerated carriers display very low mobility. In the case of amorphous materials, localized states are present below the CB and above the VB mobility edges as a consequence of lattice disorder. The mobility of carriers in these states is much lower than that in the extended states, so that the existence of initial recombination effects in amorphous materials is quite probable. In fact, during the thermalization time the electron–hole pairs do not cover a distance long enough to prevent recombination due to their mutual coulombic

attraction. Owing to this insufficient separation, a certain fraction of the photogenerated carriers recombine before the transport process can separate them permanently. As a consequence, the efficiency of free photocarrier generation must be taken into account when dealing with amorphous materials, and it acts to lower the quantum yield in comparison with crystalline materials. In order to account for the geminate recombination, a generation efficiency, η_g, is introduced in eq. 2.39:

$$I_{ph} = e\Phi_0\eta_g \frac{\alpha L_d}{1+\alpha L_d}\left[1-\exp\left(-x_{SC}\frac{1+\alpha L_d}{L_d}\right)\right] \qquad 2.39$$

η_g is expected to increase by increasing the electric field across the oxide as well as by increasing photon energy [2.1-2.3].

2.7 - Quantitative use of PCS for the characterization of anodic films on metals and alloys

In previous work [1.5], a correlation between the optical band gap values of crystalline oxides, M_xO_y, and the square of the electronegativity difference of their constituents was proposed. Such a correlation was derived by assuming a direct relation between the optical band gap and the single M-O bond energy, using the Pauling equation for the single bond energy. More specifically, E_g^{opt} was found to depend linearly on the square of the difference of electronegativity (Pauling's scale) between oxygen (χ_O) and metal (χ_M), according to the following equation:

$$E_g^{opt} = A\,(\chi_O - \chi_M)^2 + B \qquad 2.40$$

where A and B are determined by best-fitting of the experimental E_g vs $(\chi_O - \chi_M)^2$ data. With the exception of Ni, which followed the sp correlation, the following two equations were found for sp metal and d metal oxides respectively:

sp-metal) $E_g - \Delta E_{am}$ (eV) = 2.17 $(\chi_M - \chi_O)^2$ – 2.71 2.41

d-metal) $E_g - \Delta E_{am}$ (eV) = 1.35 $(\chi_M - \chi_O)^2$ – 1.49 2.42

where $\Delta E_{am} = 0$ for crystalline oxides, whilst increasing ΔE_{am} values have been suggested as the degree of crystallinity decreases. In the case of mixed oxides, the average single bond energy is estimated by taking into account the contributions of both cations involved in formation of the network. Thus, the same correlations were extended to the case of mixed amorphous oxides, considering an average cationic electronegativity, defined as follows:

$$\chi_{M,av} = x_i\chi_i + x_j\chi_j \qquad 2.43$$

where i and j refer to the two metals in the "mixed" oxide, and x_i and x_j represents their cationic fractions. Hence, a quadratic dependence of E_g on the oxide composition is predicted. The extension of eq. 2.40 to sp-d mixed oxides poses the problem of which best-fitting line should be used. The study of the photoelectrochemical behaviour of a large number of mixed oxides [2.49-2.52] allowed the validity of eq. 2.40 to be tested, leading to the conclusion that the d metal oxide correlation could hold for sp-d metal oxides, provided that the percentage of d-metal in the film is sufficiently high: a threshold of about 21at.% W was found for Al-W mixed oxides [2.52].

REFERENCES

[2.1] F. Di Quarto , F. La Mantia, M. Santamaria, in: Su-Il Pyun, Jong-Won Lee (Eds.), Modern Aspects of Electrochemistry, Springer, Inc. New York, 2009, p. 231.

[2.2] F.Di Quarto, S.Piazza, M. Santamaria, C. Sunseri, in: H.S. Nalwa (Ed.), Handbook of Thin Film Materials, vol. 2, Academic Press, S. Diego, 2002, p.373.

[2.3] F.Di Quarto, M. Santamaria, C. Sunseri, Photoelectrochemical techniques in corrosion studies, in: P. Marcus, F. Mansfeld (Eds.), Analytical Methods in Corrosion Science and Technology, Taylor and Francis, Boca-Raton, 2006, p.697.

[2.4] a) F. Di Quarto, F. La Mantia, M. Santamaria, Electrochimica Acta, 50, (2005), 5090; (b) La Mantia, F.; Habazaki, H.; Santamaria, M.; Di Quarto, F. Russian Journal of Electrochemistry, 46, (2010), 1306; c) F. La Mantia, J. Stojadinovich,; M. Santamaria, F. Di Quarto, ChemPhysChem, 13, (2012), 2910.

[2.5] H. L. F. von Helmholtz, Ann. Phys. Chem. 7, (1879), 337.

[2.6] G. Gouy, Ann. Chim. Phys. 29, (1903), 145.

[2.7] O. Stern, Z. Elektrochem. 30, (1924), 508.

[2.8] D. C. Grahame, Chem. Rev. 47, (1947), 441.

[2.9] M. Green, in “Modern Aspects of Electrochemistry” (B. E. Conway and J. O’M. Bockris, Eds.), Vol. 2, p. 343. Butterworths, London, 1959.

[2.10] R. Parsons, in “Advances in Electrochemistry and Electrochemical Engineering”(P. Delahay, Ed.), Vol. 1, p. 1. Interscience, New York, 1961.

[2.11] P. Delahay, “Double Layer and Electrode Kinetics.” Interscience, NewYork, 1966.

[2.12] R. Parsons, Chem. Rev. 90, (1990), 813, and references therein.

[2.13] A.Wieckowski, Ed., “Interfacial Electrochemistry.” Marcel Dekker, New York, 1999.

[2.14] H. Gerischer, in “Advances in Electrochemistry and Electrochemical Engineering” (P. Delahay, Ed), Vol. 1, p. 139. Interscience Publishers, New York, 1961.

[2.15] V. A. Myamlin and Yu. V. Pleskov, “Electrochemistry of Semiconductors.” Plenum Press, New York, 1967.

[2.16] H. Gerischer, in “Physical Chemistry. An Advanced Treatise” (H. Eyring, D. Henderson, andW. Jost, Eds.), Vol. IXA, p. 463. Academic Press, New York, 1970.

[2.17] A. J. Nozik, “Faraday Discussion No.70,” The Royal Society of Chemistry, London, 1980.

[2.18] S. R. Morrison, “Electrochemistry at Semiconductor and Oxidized Metal Electrodes.” Plenum Press, New York, 1980.

[2.19] Yu. V. Pleskov and Yu. Ya. Gurevich, “Semiconductor Photoelectrochemistry.” Consultants Bureau, New York, 1986.

[2.20] A. Hamnett, in “Comprehensive Chemical Kinetics” (R. G. Compton, Ed.), Vol. 27, p. 61. Elsevier Science, Oxford, 1987.

[2.21] J. O’M. Bockris and S. U. M. Khan, “Surface Electrochemistry.” Plenum Press, New York, 1993.

[2.22] S. Trasatti, in “Comprehensive Treatise of Electrochemistry”(J. O’M. Bockris, B. E. Conway, and E. Yeager, Eds.), Vol. 1, p. 45. Plenum Press, New York, 1980.

[2.23] E. H. Rodherick, “Metal–Semiconductor Contacts.” Clarendon, Oxford, 1980.

[2.24] W.E. Spear, S.H. Baker, Electrochim. Acta, 34, (1989), 1691.

[2.25] F. Di Quarto, M. Santamaria, Corros. Eng. Sci. Technol., 39, (2004), 71.

[2.26] F. Di Quarto, C. Sunseri, S. Piazza, Ber. Bunsenges. Phys. Chem., 90, (1986), 549.

[2.27] F. Di Quarto, S. Piazza, C. Sunseri, Electrochim. Acta, 35, (1990), 97.

[2.28] F. Di Quarto, V.O. Aimiuwu, S. Piazza, C. Sunseri, Electrochim. Acta, 36, (1991), 1817.

[2.29] S. Piazza, C. Sunseri, F. Di Quarto, AIChE J., 38, (1992), 219.

[2.30] J.D. Cohen, D.V. Lang, Phys. Rev. B, 25, (1982), 5321.

[2.31] W. Archibald, R.A. Abram, Phil. Mag. B, 48, (1983), 111.

[2.32] a) W. Archibald, R.A. Abram, Phil. Mag. B, 54, (1986), 421;

b) W. Archibald, R.A. Abram, Phil. Mag. B, 56, (1987), 429.

[2.33] C. Da Fonseca, M. Guerreiro Ferreira, M. Da Cunha Belo, Electrochim. Acta, 39, (1994), 2197.

[2.34] M. A. Butler, J. Appl. Phys. 48, (1977), 1914.

[2.35] W. W. Gärtner, Phys. Rev. 116, (1959), 84.

[2.36] N. F. Mott and E. A. Davis, "Electronic Processes in Non-crystalline Materials," 2nd ed., Clarendon, Oxford, 1979.

[2.37] J. Tauc, "Amorphous and Liquid Semiconductors." Plenum Press, London, 1974.

[2.38] G. D. Cody, in "Semiconductors and Semimetals" (J. I. Pankove, Ed.), Vol. 21, Part B, p. 11. Academic Press, London, 1984.

[2.39] A. F. Joffe and A. R. Regel, Prog. Semicond. 4, (1960), 237.

[2.40] N. F. Mott, Contemp. Phys. 10, (1969), 125.

[2.41] T. Watanabe and H. Gerischer, J. Electroanal. Chem. 122, (1981), 73.

[2.42] S. Piazza, A. Splendore, A. Di Paola, C. Sunseri, and F. Di Quarto, J. Electrochem. Soc. 140, (1993), 3146.

[2.43] C. Sunseri, S. Piazza, and F. Di Quarto, Mater. Sci. Forum 185–188, (1995), 435.

[2.44] F. Di Quarto, S. Piazza, C. Sunseri, M. Yang, and S.-M. Cai, Electrochim. Acta, 41, (1996), 2511.

[2.45] Yu. Ya. Gurevich, Yu. V. Pleskov, and Z. A. Rotenberg, "Photoelectrochemistry." Consultants Bureau, New York, 1980.

[2.46] R. H. Fowler, Phys. Rev. 38, (1931), 45.

[2.47] H. Reiss, J. Electrochem. Soc. 125, (1978), 937.

[2.48] S. U. Khan and J. O'M. Bockris, J. Appl. Phys. 52, (1981), 7270.

[2.49] Santamaria, M.; Di Quarto, F.; Habazaki, H. Corrosion Science 50, (2008), 2012.

[2.50] Santamaria, M.; Huerta, D.; Piazza, S.; Sunseri, C.; Di Quarto, F. J. Electrochem. Soc., 147, (2000), 1366.

[2.51] Di Quarto, F.; Santamaria, M.; Skeldon, P.; Thompson, G. E. Electrochim. Acta, 48, (2003), 1143.

[2.52] Santamaria, M.; Di Quarto, F.; Skeldon, P.; Thompson, G. E. J. Electrochem. Soc., 153, (2006), B518.

3 Growth and Characterization of anodic films on magnetron sputtered Nb-Ta Alloys.

3.1 Introduction

Microelectronics is very important for almost all kinds of technology evolutions of the past four decades. In this area, the dielectrics science occupies a prominent place in providing the dominant technology in integrated capacitors or gate insulators. In the last years the main challenge has been to scale down the insulating oxide thickness keeping low values of the leakage current. This task has been partially achieved for metal-oxide-semiconductor field effect transistor thanks to the use of hafnium based dielectrics, while less has been done for dynamic random access memory and metal-insulator-metal capacitors (DRAM MIMCAP). To the last generation DRAM, very low (from 0.5 to 0.35 nm) equivalent thickness is required with the constraint to maintain a very low leakage current. This implies the use of material having high dielectric constant (~ 50) and high band gap (> 4 eV), which can be obtained by post formation thermal treatment and tuning of the oxide composition. Owing to their high value of dielectric constant, Ta_2O_5 and Nb_2O_5 are quite attractive oxides for the development of the next generation of DRAM. Tantalum oxide is a wide band gap (~ 4 eV) material with a high dielectric constant (ε = 27 – 30) if properly crystallized (T > 750°C). Niobium oxide has a higher dielectric constant (ε = 53) with respect to Ta_2O_5 but a lower band gap (~ 3.3 eV). In recent papers [3.1-3.3], it has been shown that the addition of small amount of Nb in tantalum based oxide decreases the crystallization temperature with small effect on the band gap value of the material. Thus, $(Nb_{(1-x)}Ta_x)_2O_5$ have been introduced in the International Technology Roadmap for Semiconductors (ITRS).

Tantalum–niobium mixed oxides for microelectronic components are usually prepared by high vacuum techniques (physical and chemical vapour depositions, atomic layer deposition) [3.4-3.7]. In the first part of this chapter we propose to prepare these oxides by anodizing in suitable solutions sputter-deposited Nb-Ta alloys. This electrochemical room temperature process allows to grow oxides of controlled thickness and composition, even if a detailed investigation on the

dielectric properties of these anodic films is necessary before considering their effective use in microelectronics. Once grown, the oxides were characterized by Photocurrent Spectroscopy (PCS) in order to study their solid state properties (band gap, E_g, flat band potential, U_{FB}) a function of their composition. Impedance measurements were performed to get information of their electronic properties and dielectric constant.

In a recent paper [3.8], it has been reported that by anodizing Nb in ammonium hydroxide containing electrolytes, it is possible to incorporate nitrogen into the anodic film with a marked change in the dielectric properties of the oxide. Starting from these experimental findings in the second part of this chapter, the influence of anodizing parameters (bath composition, pH and final formation voltage) on the photoelectrochemical behaviour of anodic oxide films on Ta alloys is discussed. The results are interpreted by taking into account the occurrence of N incorporation into the anodic layers.

Part of this work was realized in collaboration with research group of Prof. H. Habazaki (Hokkaido University, Japan).

The results of this chapter are reported in refs. [3.9, 3.10].

3.2 Experimental

Ta, Nb and Ta–Nb alloy films were prepared by dc magnetron sputtering. Targets consisted of a 99.9% niobium disk, of 100 mm diameter, with an appropriate number of 99.9% tantalum disks, of 20 mm diameter, located symmetrically on the erosion region for preparation of the alloys. Substrates were glass plates. Thickness of metallic layer was 300 nm. In order to obtain alloy films of uniform thickness and composition, the substrate holders were rotated around the central axis of the chamber, as well as about their own axes, during sputter deposition. As reported in ref. [3.11], tantalum and Ta-Nb alloys containing up to 22 at.% niobium comprised the β-Ta phase, with a tetragonal structure. Further increase in the niobium content resulted in the formation of a body centered cubic phase. All the alloys appear to be mainly single-phase solid solutions, whose compositions were determined by Rutherford backscattering spectroscopy [3.11].

The anodizing was undertaken in 0.1 M NaOH, in 0.1 M ammonium biborate (ABE) (pH 9) and in 0.1 M $(NH_4)_2SO_4/H_2SO_4$ (AMS, pH 0.3).at 298 K potentiodynamically at 10 mV s^{-1}.

A saturated silver/silver chloride electrode (0 V vs Ag/AgCl = 0.197 V vs SHE) was employed as reference electrode for all the electrochemical and photoelectrochemical experiments.

The experimental set-up employed for the photoelectrochemical investigations is described elsewhere [2.1-2.3]: it consists of a 450W UV–VIS xenon lamp coupled with a monochromator (Kratos), which allows monochromatic irradiation of the specimen surface through the electrochemical cell quartz windows. A two-phase lock-in amplifier (EG&G) was used in connection with a mechanical chopper (frequency: 13 Hz) in order to separate the photocurrent from the total current circulating in the cell due to the potentiostatic control. Photocurrent spectra reported below are corrected for the relative photon flux of the light source at each wavelength, so that the photocurrent yield in arbitrary current units is represented in the Y axis. All the experiments were performed in air at room temperature.

Differential capacitance curves were recorded in 0.5 M H_2SO_4 solution by using a Parstat 2263 (PAR), connected to a computer for the data acquisition. For all the experiments, a Pt net having a very high surface area was used as counter electrode and a silver/silver chloride electrode was employed as reference electrode.

Elemental depth profile analysis was conducted by glow discharge optical emission spectroscopy (GDOES) using a Jobin-Ybon 5000 instrument in an argon atmosphere of 600 Pa by applying RF of 13.56MHz and power of 35W with a pulse mode of 100Hz and a duty cycle of 0.1. The wavelengths of the spectral lines used were 302.017, 149.262, 249.678 and 130.217 nm for tantalum, nitrogen, boron and oxygen respectively.

X-ray photoelectron spectroscopy (XPS) measurements were carried out with a JEOL JPS-9200 spectrometer with a hemispherical energy analyser and Mg Kα excitation (1253.6eV). The pressure in the analysis chamber during the XPS measurements was 1.0×10^{-7}Pa. The spectra were recorded at a 90º take-off angle

with 0.1eV step and 10eV pass energy. The binding energy was calibrated by using the C1*s* peak at 285.0eV as the reference.

3.3 Anodic Film Growth

Anodic films were grown to 5 V at 10 mV s^{-1} on all investigated materials. In Fig. 3.1 we report the growth curves relating to the anodizing of Ta, Nb and Ta-66at.%Nb.

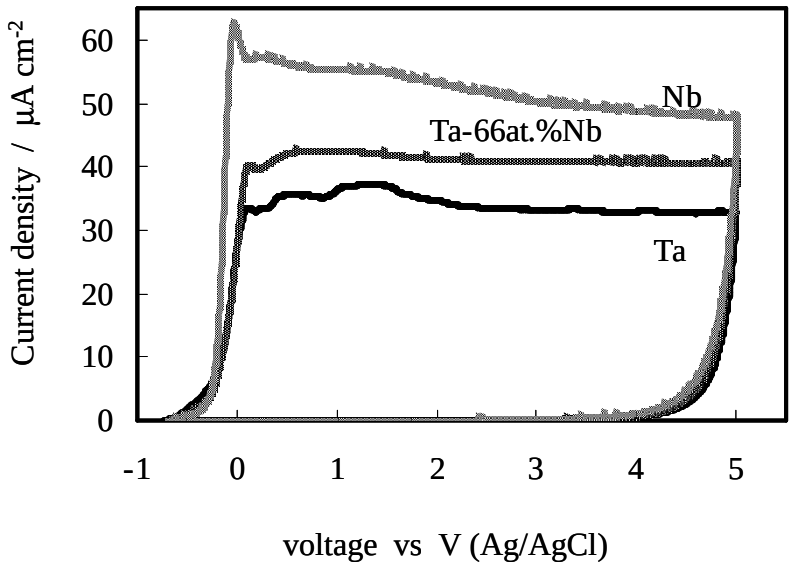

Fig. 3.1 Current density vs potential curves recorded during the potentiodynamic anodizing of Ta, Nb and Ta-66at.%Nb at 10 mV s^{-1} in 0.1 M NaOH.

As typical of valve metals, after an abrupt increase, the current density reaches an almost constant value, which is a function of the metallic substrate composition. The current density is sustained by the oxidation of metals, according to the following half cell reaction:

$$2\ Me + 5\ H_2O \rightarrow Me_2O_5 + 10\ H^+ + 10e^-$$

where Me is Ta or Nb or one of the investigated alloys. According to Faraday's law in the case of high field growth of anodic films, it is possible to relate the electric field strength, E_d, to the growth rate, dV/dt, according to eq.:

$$\frac{dV}{dt} = \eta \frac{iE_d M}{zF\rho} \qquad 3.1$$

in which i is the measured current density, M is the molecular weight of the growing oxide, z the number of electrons circulating per mole of formed oxide (i.e. 10), F the Faraday constant, ρ the film density and η the growth efficiency. η is defined as:

$$\eta = \frac{i_{form}}{i_{tot}} = \frac{i_{form}}{i_{form} + i_{diss} + i_{el}} \qquad 3.2$$

where i_{form} is the current density effectively employed for the film formation, i_{diss} is the current density fraction due to dissolution phenomena, expected to be negligible for all the investigated samples according to the Pourbaix diagrams relating to Ta and Nb [3.12], and i_{el} is the electronic current which is negligible due the blocking character of the oxides, as confirmed by the very low current circulating during the reverse scan.

In table 3.1 we report the electric field strengths and the anodizing ratios, Ã, (i.e. the reciprocal of E_d) calculated by eq. 3.1 from the current density measured during the forward scan. We have assumed for the mixed oxides a density and a molecular weight obtained by averaging according to the alloy composition the corresponding data pertaining to pure Nb_2O_5 and Ta_2O_5.

Alloy	E_d / MV cm^{-1}	Ã / Å	Oxide thickness / Å
Ta	4.8	21	114
Ta-10at.%Nb	4.30	23	121
Ta-19at.%Nb	4.2	24	130
Ta-39at.%Nb	4.0	25	134
Ta-66at.%Nb	3.8	26	140
Ta-85at.%Nb	3.4	29.	163
Nb	3.2	31	185

Table 3.1. Kinetic parameters estimated for the anodizing of Ta, Nb and Ta-Nb alloys.

Rutherford back scattering analysis revealed that the oxide composition is almost coincident with the base alloy composition [3.11] due to comparable migration rate of Nb^{5+} and Ta^{5+} during the anodizing process [3.11]. It is interesting to mention that the E_d (and thus Ã) values estimated for mixed oxides changes monotonically as a function of the base alloy composition. In table 3.1 we also report the oxides' thickness for all the investigated anodized alloys, estimated from the measured total circulated charge during the anodizing process, according to the integrated version of eq. 3.1. The films become thicker with increasing the Nb content and their value compares well with those reported in ref. [3.11], estimated for thicker anodic films by the direct observation of the transmission electron micrographs of their ultramicrotomed cross section, taking into account the different formation voltage and the higher formation rate [3.11].

3.4 Photoelectrochemical Study

In Fig. 3.2 we report the photocurrent spectra (photocurrent vs irradiating wavelength curves at constant potential) recorded by polarizing the anodic films grown on all the investigated alloys at 2 V in 0.5 M H_2SO_4.

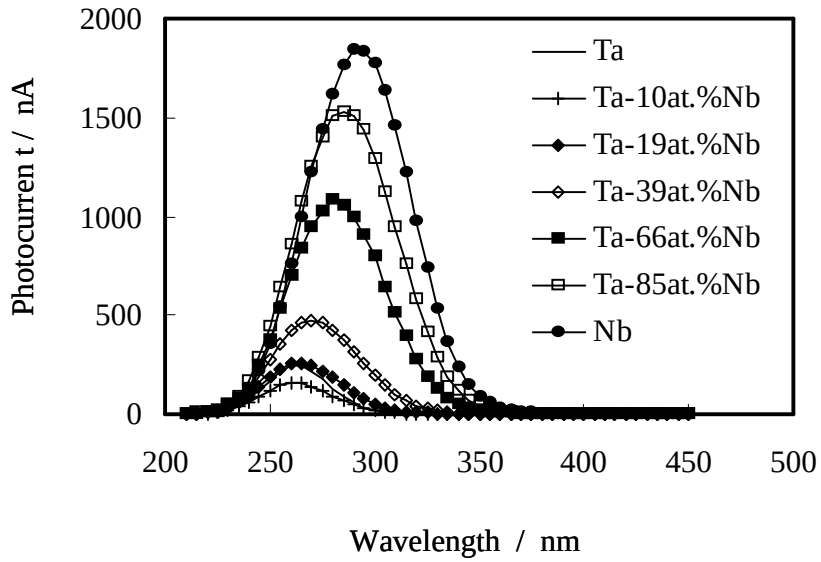

Fig. 3.2 Raw photocurrent spectra relating to anodic films grown on all investigated alloys to 5 V, recorded by polarizing the electrodes at 2 V in 0.5 M H_2SO_4.

By recording the total current circulating in the dark and under irradiation, we verified that the photocurrent was anodic at all the investigated wavelengths, as shown in Fig. 3.3 for anodic films grown on Ta-66at.%Nb alloys.

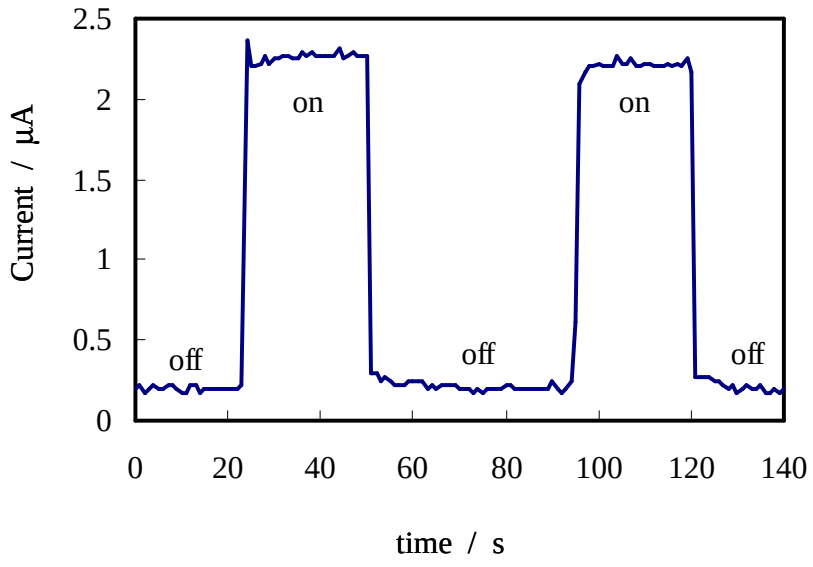

Fig. 3.3 Total current circulating in the dark (off) and under irradiation (on) for anodic films grown on Ta-66at.%Nb, recorded by polarizing the electrode at U_E = 2 V and λ = 270 nm in 0.5 M H_2SO_4.

For photon energy in the vicinity of the band gap, according to eqs. 2.31 and 2.38, the following equation holds:

$$(I_{ph}h\nu)^n \propto (h\nu - E_g^{opt}) \qquad 3.3$$

where I_{ph} is the photocurrent yield, assumed proportional to the light absorption coefficient, hν is the photon energy, E_g^{opt}, the optical band gap and the exponent n is 0.5 for indirect (non direct for amorphous materials) optical transitions [2.36]. As shown in Fig. 3.4 for the anodic film grown on Ta-66at.%Nb, from the photocurrent spectra corrected for the efficiency of the lamp–monochromator system [2.1-2.3], according to eq. 3.3 we can estimate the optical band gap of the investigated oxides by extrapolating to zero the $(I_{ph}h\nu)^{0.5}$ vs hν plot.

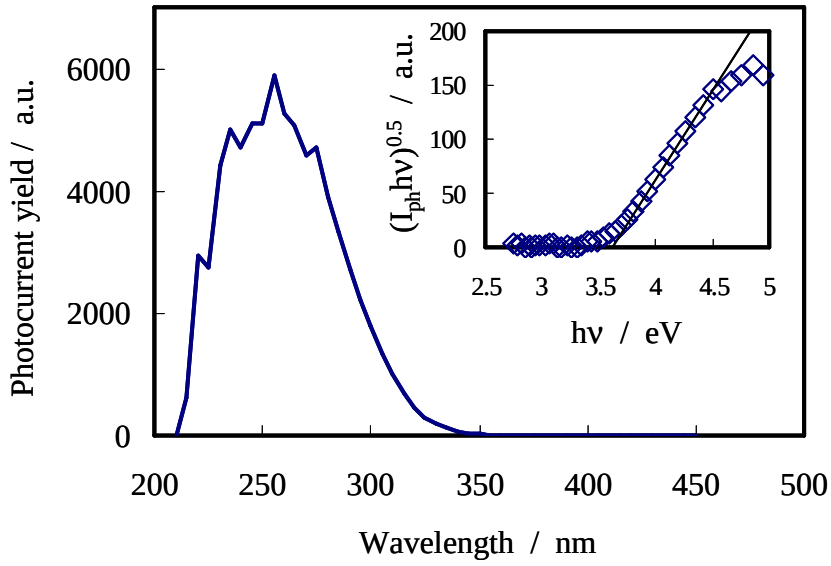

Fig. 3.4. Photocurrent spectrum relating to anodic film grown on Ta 66at.%Nb to 5 V, recorded by polarizing the electrode at 2 V in 0.5M H_2SO_4. Inset: band gap estimate by assuming non direct optical transitions.

In Fig. 3.5 we report the E_g^{opt} values estimated with the same procedure for all the investigated oxides. These data clearly show that the band gap value monotonically changes between those estimated for the corresponding pure oxides. This finding suggests that it is possible to tailor the band gap of an oxide by properly selecting the composition of the base alloy to be anodized.

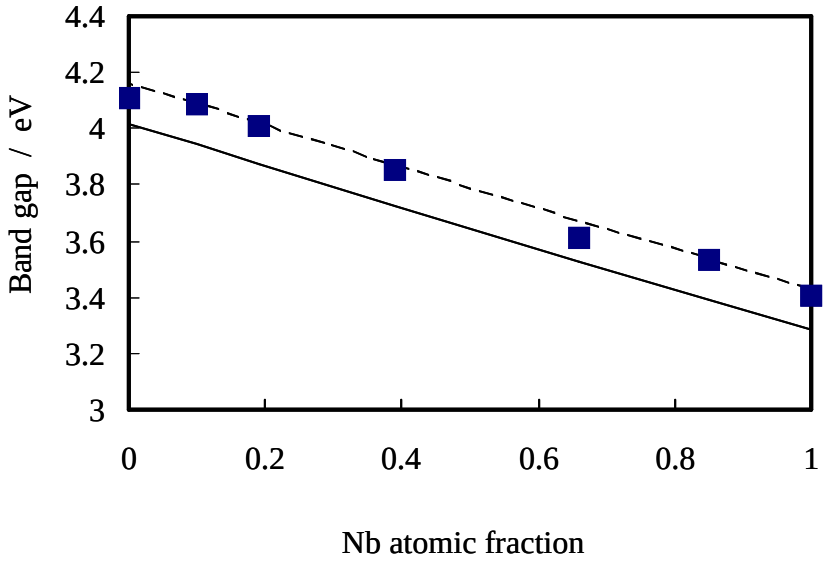

Fig. 3.5 . Experimental band gap values for Ta and Nb containing mixed oxides as a function of the Nb atomic fraction, x_{Nb}. Continuous line represents the theoretical prediction for crystalline oxides according to eqs (2.42) and (2.43). Dotted line represents the theoretical prediction for amorphous oxides according to eqs (2.42) and (2.43) with $\Delta E_{am} = 0.15$ eV.

In order to use eqs. 2.42 and 2.43 to fit the experimental band gap values of the investigated Ta-Nb mixed oxides, we assume $\chi_{Ta} = 1.50 \pm 0.05$ and $\chi_{Nb} = 1.60 \pm 0.05$, which are in the range of uncertainty accepted by Pauling [3.13]. As Fig. 3.5 shows E_g^{opt}, differs from the values calculated by means of eqs. 2.42 and 2.43, of a quantity which is less than 0.15 eV and in the range foreseen by the taking into account the amorphous nature of the investigated layers.

The good agreement between the experimental E_g values of Ta-Nb mixed oxides and those predicted by eq. 2.42 is a further evidence of the validity of the correlation between the electronegativity of the oxides' constituents and their band gap. This correlation is a powerful tool for the prediction of the band gap of a

material starting from the knowledge of its composition. This statement becomes more convincing if we consider the large approximation provided by Density Functional Theory based methods for E_g estimation. This is the case of the band gap value calculated in ref. [3.14] in the Low Density Approximation for $TaNbO_5$ (E_g = 1.82 eV), that the authors report to be underestimated and that appears really far from the expected value according to the experimental results of Fig. 3.5.

For a possible technological application, it is very important that the band gap of the mixed oxides are between those calculated for Ta_2O_5 and Nb_2O_5, if we consider that oxides with the band gaps over 3 - 4 eV meet the specifications defined by ITRS. However, the band offset with the metal electrode is also a critical factor that may define the leakage current. Therefore, the knowledge of the energetics of the metal/oxide interface is crucial.

Photocurrent vs electrode potential curves under constant irradiating wavelength (photocharacteristics) were recorded for all the investigated oxides, by scanning the polarizing voltage toward the cathodic direction at 10 mV s^{-1}. As typical of n-type semiconducting materials, the photocurrent decreases by decreasing the polarizing voltage, i.e. the electric field strength across the film. Due the very low thickness of the investigated films, the contribution to the measured photocurrent coming from the field free region is negligible. The zero photocurrent potential, V_{on}, which can be assumed as a rough estimate of the flat band potential, changes sensitively on going from Nb_2O_5 (V_{on} = - 0.25 V vs. Ag/AgCl) to Ta_2O_5 (V_{on} = - 1.0 V vs. Ag/AgCl).

In Fig. 3.6 we report the I_{ph} vs polarizing voltage curves relating to 5 V anodic films grown on Ta, Ta-10at.%Nb and Ta-19at.%Nb.

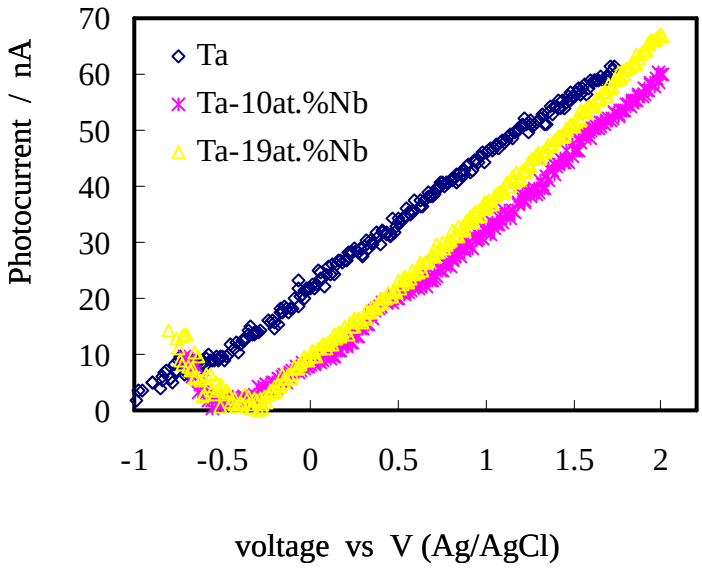

Fig. 3.6. Photocurrent vs potential curves relating to 5 V anodic films grown on Ta, Ta-10at.%Nb and Ta-19at.%Nb. Irradiating wavelength 240 nm, solution: 0.5 M H_2SO_4 and potential scan rate 10 mV s^{-1}.

It is interesting to stress that the addition of a small amount of Nb shifts sensitively the zero photocurrent potential toward more anodic values with respect to Ta_2O_5. Owing to the amorphous nature of all the investigated anodic films, we expect an influence of the irradiating photon energy as well as of the electric field strength on the photocurrent. The lack of the long range order for the amorphous oxides is responsible of a reduced mobility of the generated photocarriers, which do not cover during their thermalization time a distance long enough to prevent their recombination. Thus, for amorphous oxides it is not possible to assume as unit the efficiency of free carriers generation even for photon energies higher than the band gap of the material (geminate recombination). In order to get information on the mobility of the photocarriers we have fitted the I_{ph} vs potential, U_E, curves were fitted according to power law

$$\left(I_{ph}\right)^n \propto \left(U_E - V^*\right) \qquad 3.4$$

The best fitting exponent, n, and the extrapolated zero photocurrent potential, V*, are reported in table 3.2.

Metallic substrate	Wavelength / nm	n	V* (V)
Ta	240	0.975	- 1.00
	270	0.975	- 1.02
	300	0.975	- 0.97
Ta-10at%Nb	240	0.80	- 0.52
	270	0.65	- 0.45
Ta-19at%Nb	240	0.90	- 0.39
	270	0.65	- 0.43
Ta-39at%Nb	240	1.25	- 0.30
	270	0.78	- 0.34
	300	0.73	- 0.32
Ta-66at%Nb	240	1.15	- 0.26
	270	1.03	- 0.24
	300	0.85	- 0.29

Table 3.2. Parameters obtained by fitting according to power law, $(I_{ph})^n \propto (U_E - V^*)$ (see eq. 3.4) the experimental photocharacteristics recorded for anodic films grown to 5 V at 10 mV s^{-1} on Ta and Ta-Nb alloys in 0.5 M H_2SO_4.

A supralinear (n < 1) behaviour was evidenced for the oxides grown on Ta rich alloys and, in spite of the narrow energy range we were able to exploit due to the wide band gap of these oxides, it was possible to evidence that n decreases with increasing the irradiating wavelength, as expected for amorphous films. The estimated V* confirmed the shift toward anodic potential of the U_{FB} for Nb containing mixed oxides with respect to pure Ta_2O_5. The more anodic U_{FB} of $(Ta_{0.9}Nb_{0.1})_2O_5$ with respect to pure Ta_2O_5 can account for the dependence of photocurrent on oxide composition. A careful inspection of Fig. 3.2 shows that the

measured photocurrent increases with increasing Nb content with the exception of the anodic film on Ta-10at.%Nb, for which the I_{ph} vs wavelength curve is slightly lower that the corresponding curve for Ta_2O_5 in spite of the very close band gap value. We believe that such a finding can be related to the electric field strength across the mixed oxide which is expected to be lower owing to its more anodic flat band potential.

For higher Nb content (see Fig. 3.7), by increasing the irradiating wavelength the dependence of I_{ph} on U_E changes from sublinear to supralinear (see table 3.4). Such a dependence has been detailed discussed for pure a-Nb_2O_5 anodic films and is related to the strong dependence on the electric field of the geminate recombination efficiency [3.15].

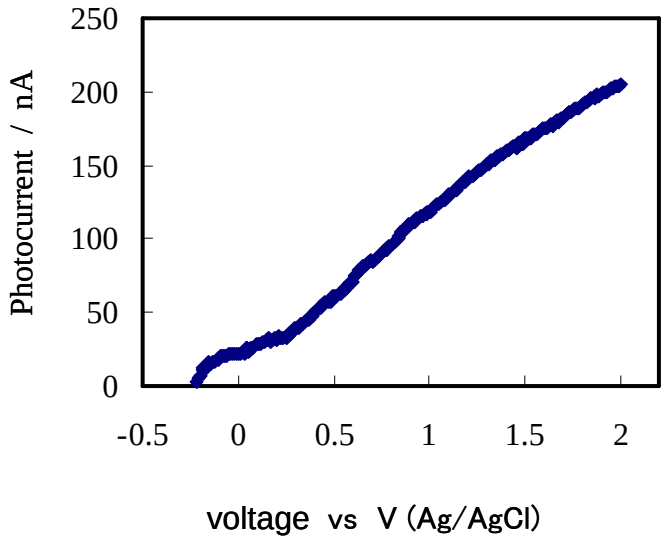

Fig. 3.7. Photocurrent vs potential curve relating to 5 V anodic films grown on Nb. Irradiating wavelength 340 nm, solution: 0.5 M H_2SO_4 and potential scan rate 10 mV s^{-1}.

3.5 Differential Capacitance Study

In order to get information on the dielectric properties of the investigated oxides, we recorded differential capacitance curves as a function of the a.c. signal frequency as well as of the oxide composition in a wide electrode potential range (from 3 V to the flat band potential). In Fig. 3.8 we report the measured series capacitance, C_M, of the Ta/Ta_2O_5/electrolyte interface recorded in 0.5 M H_2SO_4 at three different frequencies. C_M depends on both the polarizing potential and a.c. frequency, as typical of amorphous semiconductors. However, the measured capacitance becomes almost independent on U_E when $f_{a.c.}$ = 5 kHz.

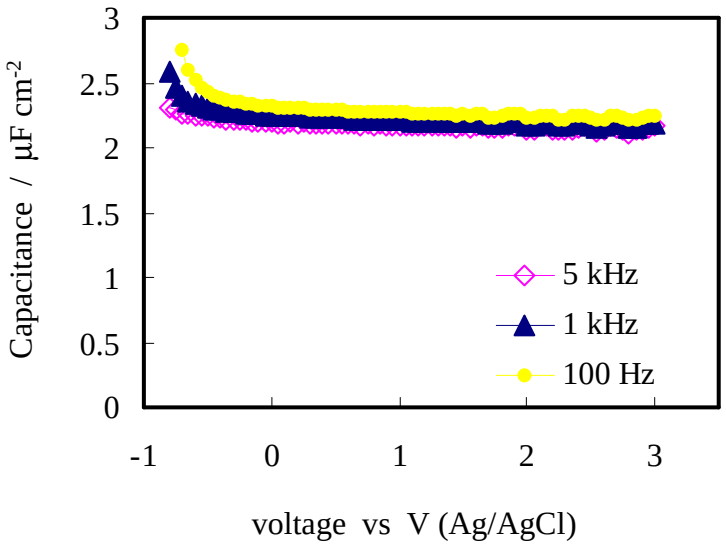

Fig. 3.8. Measured series capacitance of the Ta/Ta_2O_5/electrolyte interface recorded in 0.5 M H_2SO_4 at three different frequencies.

It is evident that even the anodic film grown on Ta-10at.%Nb shows a behaviour different from that shown by Ta_2O_5. In spite of the very close band gap value, the anodic film with the lowest Nb content shows a flat band potential more

anodic than that of tantalum oxide, in agreement with the photoelectrochemical results. The shift toward the anodic direction of the flat band potential of all the mixed oxide with increasing Nb content, suggested by the photoelectrochemical results, is confirmed by the differential capacitance curves of Fig. 3.9.

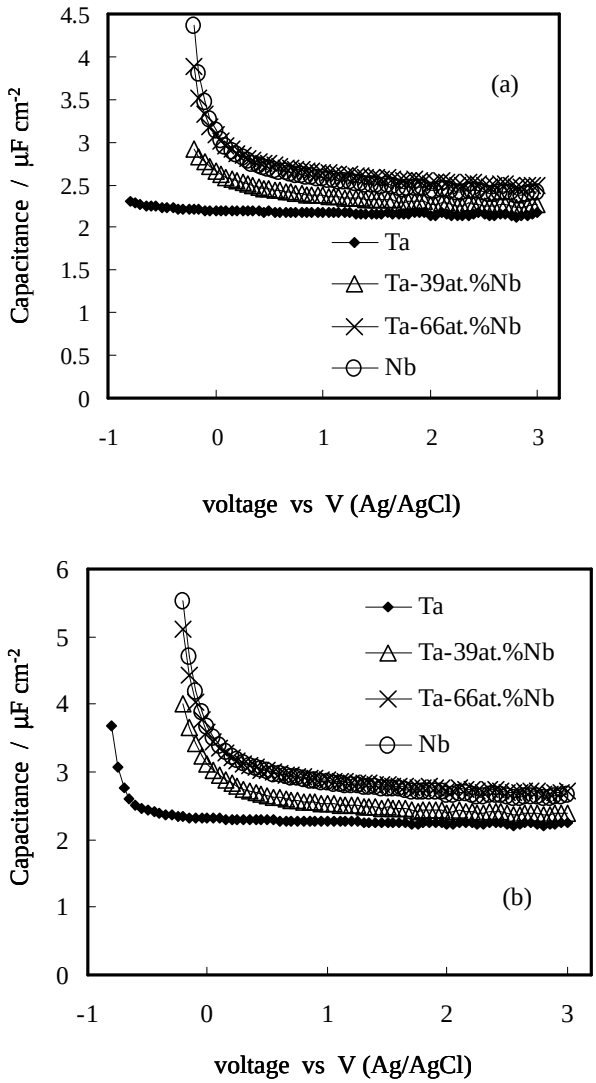

Fig. 3.9 Measured series capacitance, C_M, for all the investigated films recorded in 0.5 M H_2SO_4. Frequency of the a.c. signal: a) 5 kHz and b) 100 Hz.

According to Amorphous Semiconductor Schottky Barrier Theory (see section 2.4), in the high band bending region, i. e. for $e\psi_S > (E_g/2 - \Delta E_F)$, when a deep depletion region at the surface of a-SC/El junctions appears [2.4] the total capacitance of barrier can be modelled as a two series capacitance according to equation 2.18.

Under high band bending ($e\psi_S > E_g/2 - \Delta E_F$) and high frequency ($\psi_C \rightarrow 0$), $C(\psi_S, \omega) \cong C(\psi_C, 0)$ and, thus, we can assume that the space charge region width coincides with the whole oxide thickness. This allows to estimate the oxides' dielectric constant according to the following eq.:

$$C = \frac{\varepsilon\varepsilon_0}{d} \qquad 3.5$$

By subtracting to the measured capacitance the Helmholtz double layer contribution, assumed ~ 20 μF cm^{-2} in concentrated aqueous solution (as 0.5 M H_2SO_4 is) [3.16] we can have the idea on how the $\frac{\varepsilon}{d}$ ratio changes by changing the oxide composition. We know from the anodizing curves (see previous sections) as well as from the transmission microscopy images of ultramicrotomed sections [3.11] that the film thickness increases with increasing Nb content into the mixed oxide. The knowledge of d allows to estimate the oxide dielectric constant from the capacitance values measured at 5 kHz at the highest band bending (U_E = 3V), reported in Fig. 10 as a function of the film composition. ε monotonically increases with increasing Nb content, as found for thicker films grown on the same investigated alloys [3.11]. Such dependence also agrees with the dielectric constant calculated by computation method for $NbTaO_5$, reported in ref. [3.14].

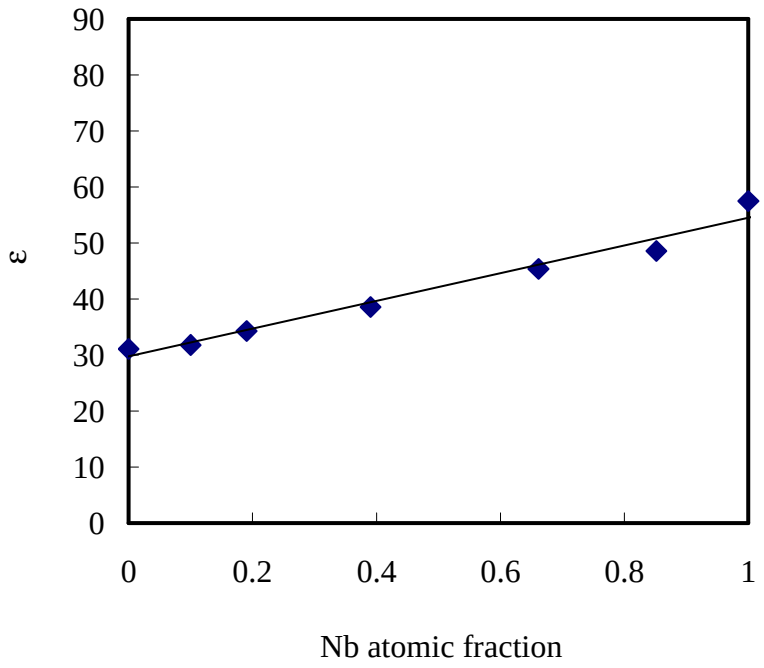

Fig. 3.10 Dielectric constant ε as a function of the Nb content into the oxide.

Finally, we want to stress that eq. 2.14 allows to estimate ΔE_F, provided that it is possible to estimate a frequency of the a.c. signal high enough to make the capacitance almost independent on the applied potential. The simultaneous knowledge of this energy distance and of the band gap value of the oxide allows to get the energetics of the metal/oxide/electrolyte interface, as reported in Fig. 3.11 for anodic films grown on Ta, Ta-10at.%Nb and Ta-19at.%Nb. A work function of 4.25 eV has been assumed for tantalum and for the alloys [3.17], due to their low Nb content and by taking into account that a very close work function is reported for Nb (4.30 eV according to ref. 3.17). These sketches provide an idea of the band offset for the investigated metal/oxide systems. With a Nb content of 19%, we get a mixed oxide with a dielectric constant 10% higher than that of Ta_2O_5 with a reduction of less than 3% of the band gap. However, to have a complete set of information it is very important to have a look to the energetics of the metal/oxide interface, that shows a reduction of the band offset (see Fig. 3.11). If we consider that the metal or

alloys to be anodized can be easily sputtered on a metal with a properly selected work function, we can hypothesize to control the band offset by properly selecting the materials involved in the fabrication of the metal/oxide interface.

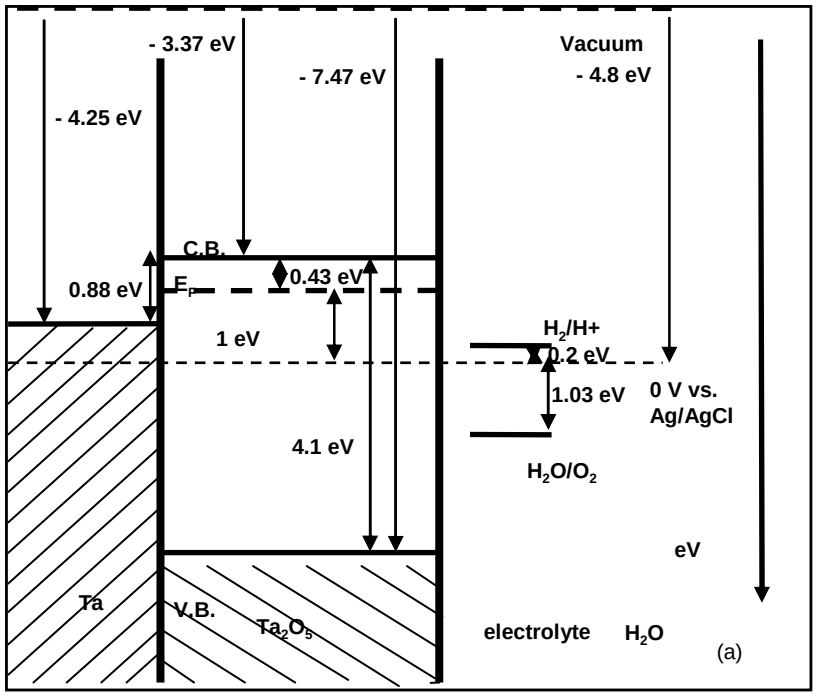

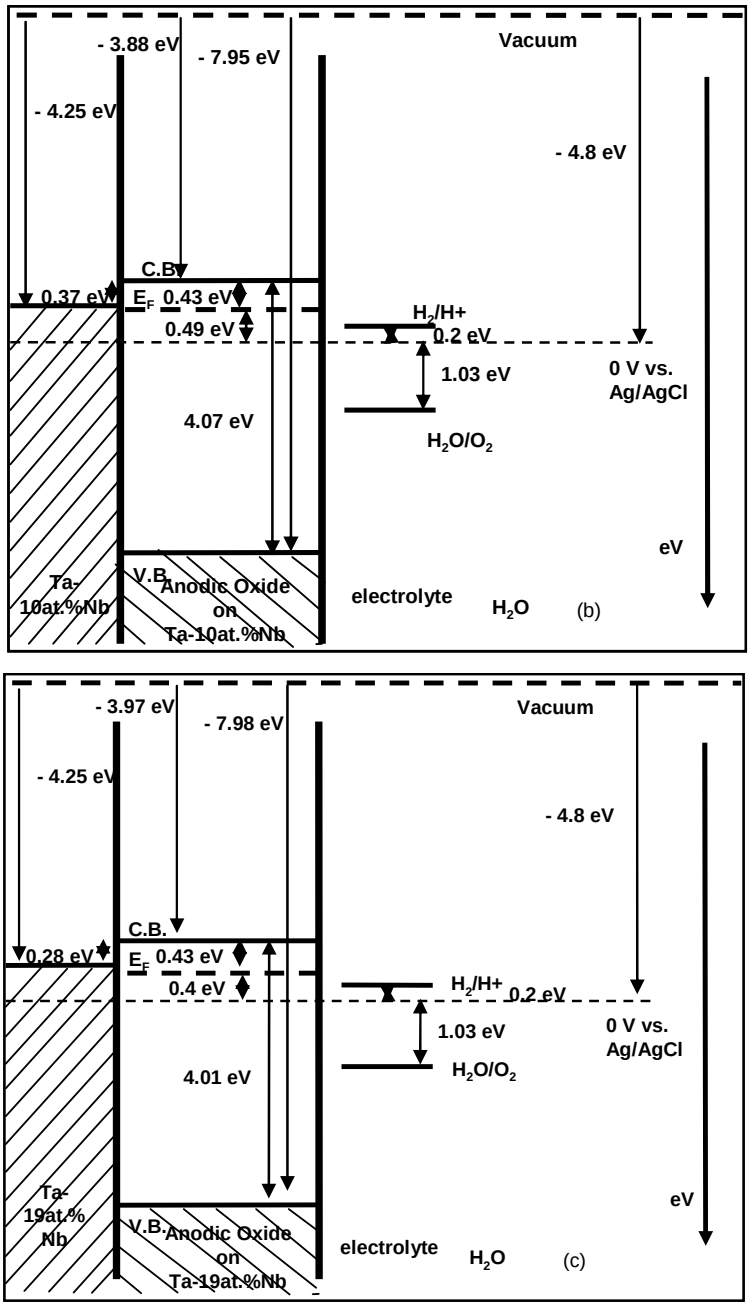

Fig. 3.11 Sketch of the energetic levels of metal/oxide/electrolyte interface for anodic films grown on a) Ta, b) Ta-10at.%Nb, c) Ta-19at.%Nb.

3.6 Nitrogen incorporation on anodic Ta_2O_5.

In Fig. 3.12a we report the raw photocurrent spectrum relating to the anodic layer grown to 5 V(Ag/AgCl) (~ 11 nm thick) in 0.1 M NaOH, recorded by polarizing the electrodes at 2 V(Ag/AgCl) in 0.5 M H_2SO_4.

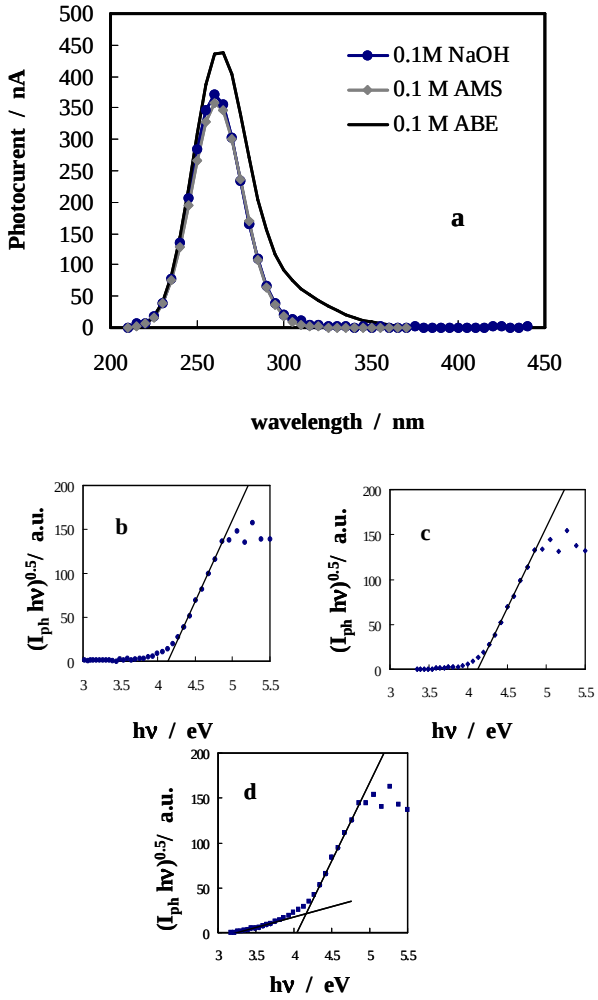

Fig. 3.12 a) Raw photocurrent spectra relating to anodic films grown on Ta to 5V(Ag/AgCl), recorded at 2V(Ag/AgCl) in 0.5 M H_2SO_4. $(I_{ph}h\nu)^{0.5}$ vs hν plots relating to the oxides grown in b) 0.1 M NaOH and c) 0.1 M AMS and d) 0.1 M ABE.

By extrapolating to zero the $(I_{ph}h\nu)^{0.5}$ vs hν plot a mobility gap of 4.13 eV has been estimated for the film formed in NaOH solution (see Fig. 3.12b), and in good in agreement with the band gap values reported in the literature for anodic oxide on Ta metal [3.18] and quite close to the value of crystalline Ta_2O_5 oxide (~ 3.9 eV). As previously suggested (see Chapter 2) the difference (~ 0.2 eV) in the optical band gap value of amorphous and crystalline tantalum oxide can be attributed to the effect of lattice disorder in amorphous oxide which affect both the DOS distribution in the vicinity of band edges and the intensity of optical transition between localized states The small tailing at lower energy observed in Fig. 3.12b agrees with the model of DOS suggested in Chapter 2.

Photocurrent spectra (see Fig. 3.12a) very similar to those relating to films grown in NaOH solution were recorded for anodic films similarly grown in 0.1 M $(NH_4)_2SO_4$ (pH corrected to 0.3 by the addition of H_2SO_4), for which a band gap value of 4.1 eV was estimated according to eq. 3.3 (Fig. 3.12c)

A different photoelectrochemical behaviour was displayed by the anodic layer grown in 0.1 M ABE (see Fig. 3.12), due to the presence of a consistent red-shift in the optical absorption extending well below the band gap of Ta_2O_5 reported above. In this last case, apart from the band gap value (4.04 eV) very close to that estimated for anodic films grown in the other investigated electrolytes (see Fig. 3.12d), it was possible to derive from the longer wavelength region of photocurrent tail a second lower threshold at around 3.25 eV.

The presence of sub-band gap photocurrent is more evident for thicker films formed in 0.1 M ABE. In Fig. 3.13a we compare the photocurrent spectra relating to anodic films grown on tantalum to 50 V in AMS, NaOH and ABE solutions. By assuming non direct optical transitions, according to eq. 3.3 two linear regions are present in the $(I_{ph}h\nu)^{0.5}$ vs hν plots for the anodic film grown in ABE, corresponding to optical transitions at 3.25 and 4.05 eV (see Fig. 3.13b), in agreement with the behaviour of thinner films. For both 50 V anodic films grown on Ta in 0.1 M NaOH and AMS there is no evidence of the optical transitions at lower energy (see Fig. 3.13c and 3.13d).

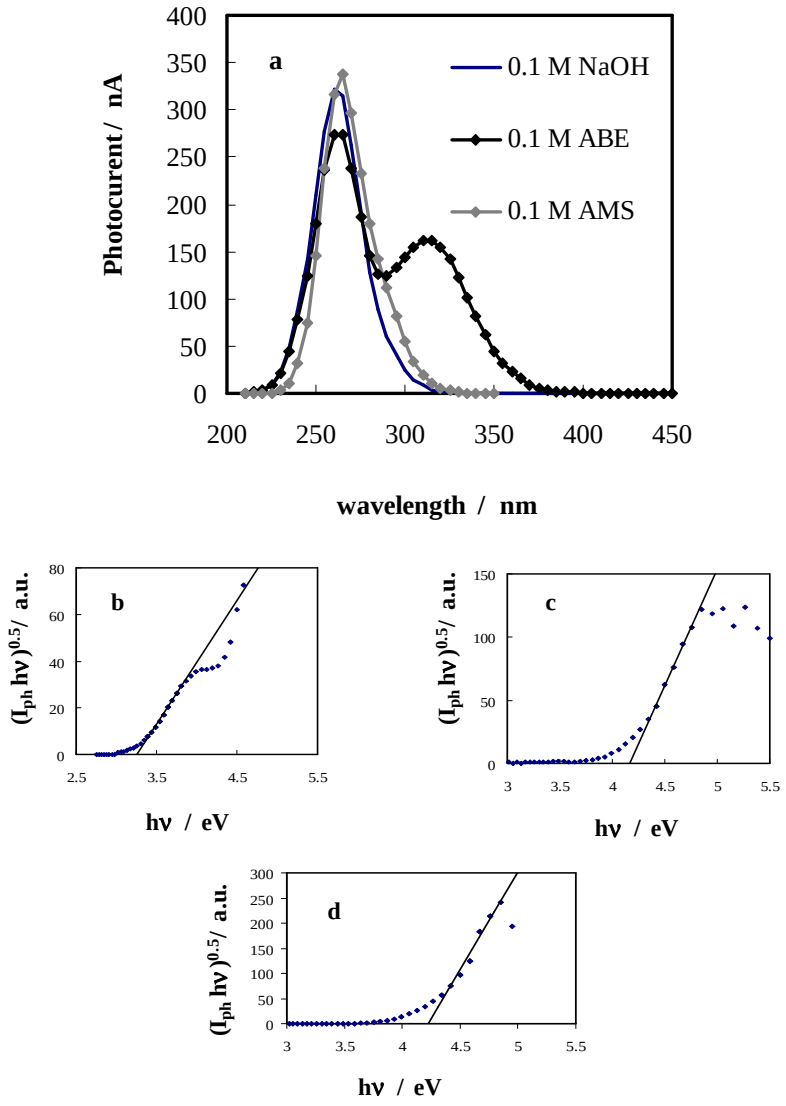

Fig. 3.13 a) Raw photocurrent spectra relating to anodic films grown on Ta in 0.1 M NaOH, 0.1 M ABE and 0.1 M AMS to 50V, recorded at 3 V(Ag/AgCl) in 0.5 M H_2SO_4. $(I_{ph}h\nu)^{0.5}$ vs hν plots relating to the oxide grown in b) 0.1 M ABE and c) 0.1 M NaOH and d) 0.1 M AMS.

In order to get further information on the nature of this sub-band gap optical transitions photocurrent vs potential curves (photocharacteristics) under constant irradiating wavelength were recorded. In Fig. 3.14 we report the photocharacteristics (normalized for the maximum value of I_{ph}) obtained under illumination with photons having supra-band gap energy (λ = 270 nm, i.e. $h\nu$ = 4.6 eV) for the anodic films of Fig. 3.13.

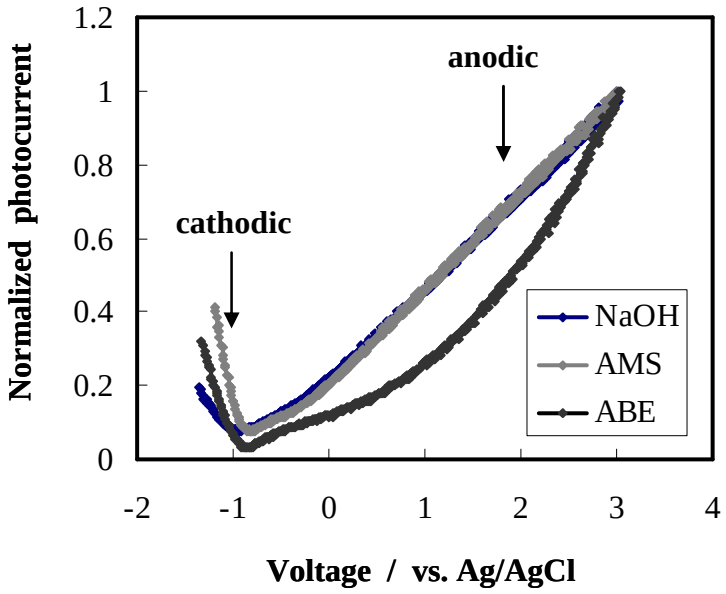

Fig. 3.14 Normalized Photocurrent vs. U_E curve relating to anodic films grown on Ta in 0.1 M NaOH, 0.1 M ABE and 0.1 M AMS to 50V, by scanning the electrode potential at 10 mV s^{-1} under monochromatic irradiation (270 nm) in 0.5 M H_2SO_4

By scanning the electrode potential toward the cathodic direction (v_{scan} = 10 mV s^{-1}), an inversion of the photocurrent sign occurs, as typical of insulating material [2.2] independently on the anodizing electrolyte. The electrode potential corresponding to the inversion of photocurrent sign can be roughly assumed as a proxy value of flat band potential, U_{FB}. However, if we compare the

photocharacteristic relating to the film grown in ammonium biborate with those relating to the anodic films grown in NaOH and AMS, it is evident that the dependence of the measured photocurrent on the applied potential is very different. Quasi-linear photo-characteristics were recorded for the films grown in NaOH and AMS solutions with an inversion photocurrent potential around - 1 V vs (Ag/AgCl). For the film grown in ABE, the photocurrent changes linearly in a narrow potential range between V_{inv} and - 0.5 V(Ag/AgCl) (omhic region). At higher band bending, ($U_E - U_{FB}$), I_{ph} shows an exponential-like dependence on electrode potential, i.e. electric field strength across the oxide at constant thickness by taking into account the insulating nature of the investigated oxide [2.2]. This finding suggests a Poole-Frenkel mechanism of transport of photocarriers dominated by a trap limited mobility [2.36] in a band of localized states generated by the incorporated species.

3.6.1 Discussion

The anodizing of valve metals has been extensively studied in the last decades and there is currently a general agreement on the mechanism of growth of the oxides, which is sustained by a field assisted hopping of mobile ions, i. e. outward migrating metal cations and inward migrating oxygen anions. At 100% current efficiency of film growth (as expected for Ta in all the investigated solutions according to the Pourbaix diagram for Ta, ref. 3.12), 25% of film thickness of tantalum oxide forms at the oxide/electrolyte interface, while the remaining 75% forms at the metal/oxide interface, according to the transport numbers of Ta^{5+} and O^{2-} [3.19]. As widely discussed in previous papers [3.19-3.20], low concentrations of species derived from the anions of the anodizing electrolyte are normally incorporated into the growing oxide, such as phosphate, sulphate, or molybdate, Recent results reported in the literature [3.8] demonstrated that it is possible to incorporate also nitrogen inside anodic films on Nb with the surprising finding that the source of N is a cation, i.e. ammonium.

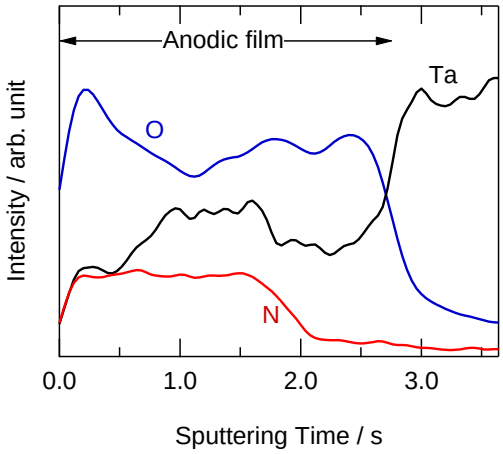

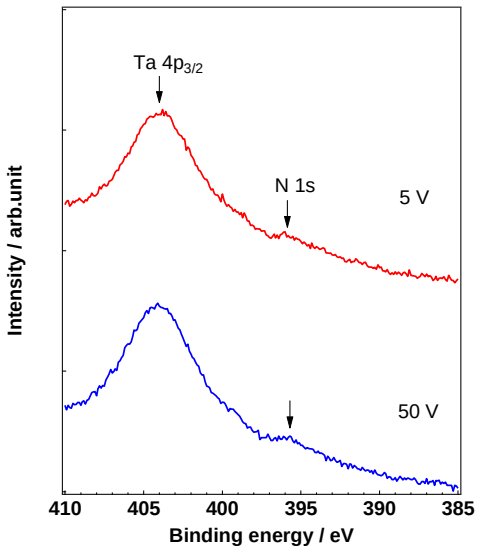

Fig. 3.15 a) GDOES depth profiles of the anodic film formed to 50V on Ta in 0.1M ABE at 293 K. b) N 1s XPS spectra of the anodic films on Ta grown to different formation voltages in 0.1M ABE.

In Fig. 3.15 we report the GDOES elemental depth profile of the 50 V anodic film grown on Ta in 0.1 M ABE. Together with the expected signals coming from tantalum and oxygen, the presence of nitrogen has been revealed. If we consider that the abrupt decrease of O signal marks the oxide/metal interface, we can postulate that the anodic film has a bilayer structure with a N containing outer part (roughly 70% of the whole thickness) and an inner practically nitrogen free part. Assuming the transport number of 0.25 for cations as mentioned above, it can be said that the nitrogen species migrates inwards and their migration rate is approximately 0.65 that of O^{2-} ions.

The photoelectrochemical results reported in this paper show a marked change in the optical properties of anodic films on Ta only when they are anodized in an electrochemical bath containing NH_4^+ at pH 9. If we match this experimental evidence with the results reported in Fig. 3.15a, we can conclude that during anodic oxidation, the interfacial processes at the oxide/electrolyte interface that are responsible of water molecules dissociation under high electric field to give O^{2-}, can also deprotonate ammonium ions generating NH_{3-x}^{x-} moieties than can migrate inward and can be bonded to Ta^{5+} together with O^{2-} with the consequent formation of an oxy-nitride. A fundamental role is played by the electrolyte pH which determines the sign of the charge on an oxide's surface. Due to the acid/base equilibria at the oxide/electrolyte interface, the surface of Ta_2O_5 is expected to be positively or negatively charged, when the solution pH is lower or higher than the isoelectric point (pH_{pzc} 2.9, ref. [3.21]), respectively. Thus, the possibility of NH_4^+ ions to get close to the oxide surface is influenced by the electrolyte pH, hindering N incorporation in strongly acidic ammonium ions containing solution. This suggestion is in agreement with the behaviour reported by Ono et al. in ref. [3.8], where N incorporation is reported to occur in H_3PO_4/NH_3 solution only when the electrolyte pH is higher that 8.

XPS was used to examine the surface composition of Ta after anodizing in 0.1 M ABE. Fig. 3.15b shows the electron binding energy of Ta $4p_{3/2}$ and N 1*s* characterized by XPS. The N 1s region shows a peak at ~ 396 eV (missing for the

anodic films grown in 0.1 M NaOH), that can be assigned to N in TaO_xN_y [3.22]. The broad Ta $4p_{3/2}$ signal at higher binding energy (~ 404 eV) is assigned to Ta in the same oxynitride [3.22]. A further support to this identification comes from ref. [3.23,3.24], where the XPS spectra relating to N-doped tantalum pure and mixed oxides in the same binding energy region are reported.

As suggested by the photoelectrochemical results, the incorporation of N species causes the formation of electronic states inside the mobility gap of Ta_2O_5 generating the evidenced sub band gap photocurrent. We reasonably hypothesize that such states are due to the p orbitals of nitrogen and, thus, are located above the valence band edge of Ta_2O_5 in agreement with the band structures suggested for tantalum oxy-nitride [3.25]. However, the dependence of I_{ph} on U_E for anodic films grown in ABE (see Fig. 3.14) suggests that N incorporation creates not extended states in the mobility gap of the film. These localized states work as traps for the photogenerated holes, and justify the suggested Pool-Frenkel transport mechanism of charge carriers.

This result is very important if we consider that the presence of a high concentration of localized states inside the mobility gap of Ta_2O_5, usually employed as dielectric in electrolytic capacitor industry, affects both the optical and electronic properties of the films with consequent increase of the electronic leakage current responsible for electrical instability of tantalum capacitors.

3.7 Conclusions

Ta_2O_5, Nb_2O_5 and Ta-Nb containing oxides grown by anodizing sputter-deposited Ta, Nb and Ta-Nb alloys of different composition were characterized by Photocurrent Spectroscopy and by impedance measurements.

Band gap values of 4.1 eV and 3.4 eV were estimated for anodic Ta_2O_5 and Nb_2O_5, respectively, while intermediate values were estimated for mixed oxides monotonically increasing by increasing the Ta content.

The estimated band gap values are in agreement with the proposed linear dependence of E_g on the squared difference of electronegativity of the oxide

constituents. This finding shows the potential of this correlation to predict the band gap value of an oxide knowing its composition.

Differential capacitance curves, recorded for all the investigated oxides in a wide range of electrode potential and for several frequencies of the alternative signal, were interpreted on the basis of amorphous semiconductor Schottky barrier, and allowed to determine the dielectric constant of the investigated oxides. According to the estimated values, ε depends almost linearly on the atomic fraction of one of the partner cations into the mixed oxide.

The experimental results reported in this chapter suggest that by properly selecting the alloy composition it is possible tailoring both the oxides band gap and dielectric constant, which are key parameters in determining the performance of high-k materials.

The effect of the anodizing bath composition and pH on the photoelectrochemical behaviour of anodic films grown on tantalum to different formation voltages (i.e. thickness) was studied. A band gap value of ~ 4.1 eV was estimated for 5 V and 50 V anodic films grown in NaOH and AMS solutions. For films formed in a bath containing ammonium ions at pH 9, i. e. ABE, the presence of sub-band gap photocurrent was evidenced.

GDOES compositional depth profiles revealed the presence of N in the outer two third of anodic films grown in ammonium biborate, while XPS analysis suggests the formation of a tantalum oxynitride.

A mechanism is proposed in order to investigate the role of the anodizing bath pH in determining the occurrence of nitrogen incorporation. The experimental results suggest that it is crucial the possibility of ammonium cations to reach the oxide surface, whose charge density depends on the acid-base equilibria at the interface, mainly conditioned by the difference between the bath pH and zero charge pH.

REFERENCES

[3.1] K. Kukli, M. Ritala, M. Leskela, J. Appl. Phys., 86, (1999), 5656.

[3.2] Y. Matsui, M. Hiratani, I. Asano, S. Kimura, IEEE Trans. Electron Devices, 225, (2002).

[3.3] Y. Matsui, M. Hiratani, S. Kimura, and I. Asano, J. Electrochem Soc., 152, (2005), F54.

[3.4] K. Kishiro, N. Innoue, S.J. Chen, and M. Ypshimaru, J. Appl. Phys., 37, (1998), 1336.

[3.5] J.C.Yu, B.C. Lai, J.Y.M. Lee, IEET Trans. Electron Devices, 21, (2000), 537.

[3.6] B.C.M. Lai, N.H. Kung, Y.M. Lee, J. Appl. Phys., 87, (1999), 4087.

[3.7] M. Stromme, G.A. Niklasson, M.Ritala, M. Leskela, and K. Kukli, J. Appl. Phys., 90, (2001), 4532.

[3.8] S. Ono, K. Kuramochi and H. Asoh, Corrosion Science, 51 (7), (2009), 1513.

[3.9] F. Di Franco, G. Zampardi, M. Santamaria, F. Di Quarto, H. Habazaki Journal of The Electrochemical Society, 159, (2012), C33.

[3.10] F. Di Franco, M. Santamaria, F. Di Quarto, E. Tsuji, H. Habazaki, Electrochimica Acta, 59, (2012), 382.

[3.11] S. Komiyama, E. Tsuji, Y. Aoki, H. Habazaki, M. Santamaria, F. Di Quarto, P. Skeldon, G.E. Thompson, J. Soil. State Electrochemistry,16, (2012), 1595.
.
[3.12] M. Pourbaix, Atlas of Electrochemical Equilibria in Aqueous Solutions, Pergamon Press, Oxford, 1966.

[3.13] L. Pauling, “The Nature of Chemical Bond”, Chapter 3, Cornell University Press, Ithaca. NY, 1960

[3.14] S. Clima, G. Pourtois, A. Hardy, S. Van Elshocht, M.K. Van Bael, S. De Gendt, D. J. Wouters, M. Heyns, J. A. Kitt, J. Electrochem. Soc., 157**,** (2010), G20.

[3.15] F. Di Quarto, S. Piazza, R. D’Agostino, C. Sunseri, J. Electroanal. Chem., 228, (1987), 119.

[3.16] H. Gerischer, Electrochim. Acta, 34, (1989), 1005.

[3.17] Handbook of Chemistry and Physics, David R Lide Editor in Chief, 76th Ed., 1995

[3.18] Di Quarto, F., Gentile, C., Piazza, S., Sunseri C., Corrosion Science, 35, (1993), 801.

[3.19] Shimizu K., Kobayashi K., Philosophical Magazine B, 73, (1996), 461.

[3.20] Zhou F., LeClere D.J., Garcia-Vergara S.J., Hashimoto T., Molchan I.S., Habazaki H., Skeldon P., Thompson G.E., Journal Of The Electrochemical Society, 157, (2010), C437.

[3.21] McCafferty E., J. Electrochem. Soc., 146, (1999), 2863.

[3.22] P. Lamour, P. Fioux, A. Ponche, M. Nardin, M.F. Vallat, P. Dugay, J.P. Brun, N. Moreaud, J.M. Pinvidic, Surf. Interface Anal. 40, (2008), 1430.

[3.23] H. Shin, S.Y. Park, S. Bae, S. Lee, K.S. Hong, H.S. Jung, J. Appl. Phys. 104, (2008), 116108.

[3.24] A. Mukherji, R. Marschall, A. Tanksale, C. Sun, S.C. Smith, G.Q. Lu, L. Wang, Adv. Funct. Mater. ,21, (2011), 126.

[3.25] W. Chun, A. Ishikawa, H. Fujisawa, T. Takata, J.N. Kondo, M. Hara, M. Kawai, Y. Matsumoto, K. Domen, J. Phys. Chem. B, 107, (2003), 1798.

4 Growth and Characterization of anodic films on magnetron sputtered Nb-Al Alloys.

4.1 Introduction

In order to satisfy the requirement of miniaturization in modern linear integrated circuits, electronic components are developing toward smaller volume. For electrolytic capacitors this issue can be achieved by increasing the specific capacitance, i. e. by increasing the dielectric constant and the roughness factor. Al_2O_3 is a wide band gap, E_g, insulator [4.1] with an amphoteric character, widely employed as dielectric in electrolytic capacitors ($\varepsilon \sim 9$). It can be directly grown on Al metal by anodizing, and an easy electrochemical etching process allows to increase the specific surface of this metal.

As shown in chapter 3, Nb_2O_5 is a n-type semiconductor with relatively lower band gap ($E_g \sim 3.30 \pm 0.1$ eV) [3.9, 4.2, 4.3] and chemically stable in a wide range of pH. A very high, field dependent, dielectric constant ($\varepsilon \sim 53$) (3.9, 4.2, 4.3) is reported for anodic niobia, which makes this oxide a very appealing high k material, even if the possibility to use Nb_2O_5 as dielectric is limited by its poor blocking character.

Starting from these considerations, Al-Nb mixed oxides are anticipated to have properties that lie between those of pure Al_2O_3 and Nb_2O_5, which suggest that an improvement on the low ε value of Al_2O_3 and a lowering of the high leakage current of Nb_2O_5 could be achieved. In refs. [4.4 - 4.6] the use of chemically prepared Al_2O_3-Nb_2O_5 composite oxides is suggested as a viable route to increase the dielectric constant with respect to that of pure alumina. This effect is also observed for Al-Nb mixed oxides grown by anodizing sputter deposited Al-Nb alloys [4.7]. An increase in the dielectric constant up to ~ 22 is reported for anodic films grown on Al-44at.%Nb, which was the Nb richest investigated alloy.

In this chapter photoelectrochemical measurements were carried out on anodized samples in order to obtain information on the solid state properties (band gap, flat band potential, conductivity type) of the oxides as a function of their

compositions. The compositional dependence of E_g is discussed in order to highlight the chemical approach to tailoring of E_g for oxides on alloys that was previously suggested for pure sp-metal or d-metal oxides (see section 2.7 and ref. [1.5]). The effect of Al/Nb ratio in determining their dielectric and electronic properties was studied by means of both electrochemical impedance spectroscopy (EIS) and differential admittance (DA) measurements. The dependence of admittance components for the Nb richest investigated alloy will be discussed quantitatively on the basis of the amorphous Schottky barrier theory (see section 2.4).

Part of this work was realized in collaboration with research groups of Prof. G.E Thompson (University of Manchester, UK), Dr. Fabio La Mantia (Ruhr University, Bochum, Germany), Dr. C. Rangel (LNEG, Lisboa, Portugal).

The results of this chapter are reported in refs. [4.8 and. 4.9]

4.2 Experimental

Aluminium, niobium and Al-Nb alloys were deposited by magnetron sputtering using an Atom Tech Ltd system, with targets of aluminium (99.999%) and niobium (99.9%). Sputtering was performed in 0.5 Pa argon after previous evacuation to 5 x 10^{-5} Pa. The substrates consisted of high purity aluminium sheet that had been electropolished at 20 V in a solution of ethanol and perchloric acid (4:1 by vol.) for 180 s at 283 K. Al-Nb alloys, containing 9, 11, 21, 40, 55, 66, 81, 85 and 92 at.% niobium, were prepared. The composition of the alloys was determined by Rutherford backscattering spectroscopy (RBS), performed using 2.0 MeV He^+ ions supplied by the Van de Graaff accelerator of the University of Paris. The scattered ions were detected at 165° to the direction of the incident beam. Data were interpreted by the RUMP program. The deposited layers were anodized to 9 V (SCE) at 100 mV s^{-1} in 0.1 mol dm^{-3} ammonium pentaborate electrolyte (ABE, pH ~ 8.5) at room temperature. At this pH and temperature, both Al_2O_3 and Nb_2O_5 are reported to be thermodynamically stable according to the Pourbaix diagrams for the Al-H_2O and Nb-H_2O systems [3.12]. According to transmission electron micrographs of ultramicrotomed sections [4.7], the films are amorphous. The experimental set-up for the photoelectrochemical measurements has been described

elsewhere [2.1]. A 450 W UV-vis xenon lamp, coupled with a monochromator, allows irradiation of the specimen through a quartz window. A two-phase, lock-in amplifier, with a mechanical chopper, enables separation of the photocurrent from the total current in the cell. The photocurrent spectra are corrected for the relative photon efficiency of the light source at each wavelength, so that the photocurrent yield in arbitrary current units is represented on the y-axis. A saturated calomel electrode (0 V vs SCE = 0.24 V vs SHE) was employed as a reference electrode for all photoelectrochemical experiments.

Electrochemical impedance spectroscopy (EIS) data for anodized alloys were obtained using a Parstat 2263 (PAR), controlled by a computer via Electrochemistry PowerSuite software. A three-electrode arrangement was used, consisting of the anodized specimen, a reference electrode (silver/silver chloride) and a Pt net having a very high specific area, immersed in 0.2 M Na_2HPO_4. The impedance spectra were generated by applying a sinusoidal signal of amplitude 10 mV over the frequency range 0.1 Hz – 100 kHz. The resultant spectra were analysed with Zview software.

4.3 Anodic Film Growth

In Fig. 4.1 we report the anodizing curve relating to Al-66at.%Nb.

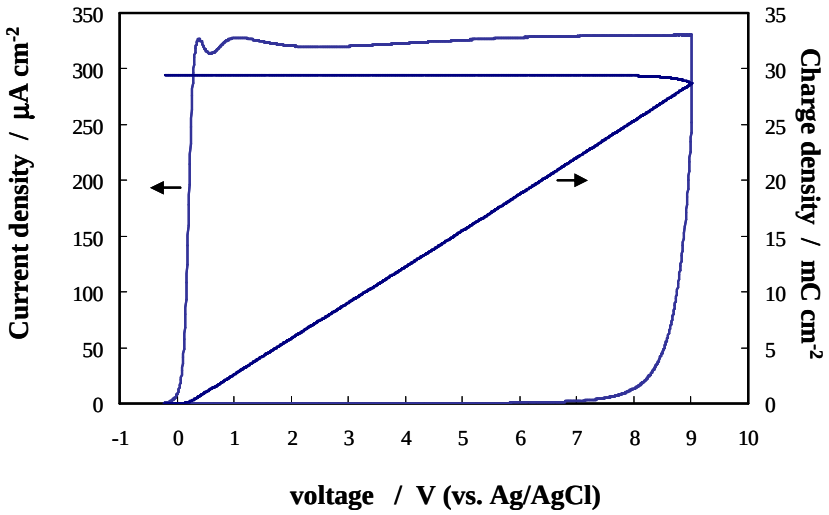

Fig. 4.1 Current density and charge density vs potential curves recorded during the potentiodynamic anodizing of Al-66at.%Nb at 100 mV s^{-1} in 0.1 M ABE.

As typical of valve metals, after an initial increase the current density reaches an almost constant value which remains unchanged up to the selected final formation voltage; it is important to stress that the charge density increases linearly with the potential during the anodizing, while it remains constant during the reverse scan, according to the theory of high field growth mechanism for valve metals. As expected for anodic barrier oxides a very low current density is measured in the reverse scan, due the formation of a blocking film. From the overall charge circulating during the anodizing, and by assuming for the oxide density and molecular weight the values obtained by averaging the density, ρ, and molecular weight, MW, of the pure oxides, it was possible to roughly estimate the film thickness, as shown in table 4.1. An Al/Nb ratio into the oxide coincident with that of the base alloy was assumed in agreement with previous results reported in the literature, based on Rutherford Back Scattering analysis of the anodic film composition [4.7,4.8]. The estimated values compare well with those estimated from

the anodizing ratio reported in refs. [4.8] for Al-Nb alloys with a Nb content ≤ 44at.%.

at.%Nb	0	9	40	55	66	81	92	100
d_{ox} (Å)	120	130	180	190	200	230	280	310

Table 4.1 Anodic film thickness estimated from circulating charge during anodizing (see text).

4.4 Photoelectrochemical Characterization

With the exception of the anodic films on the Al-9at.%Nb and Al-11at.% Nb alloys, all other investigated oxides proved to be photoactive.

As shown in Fig. 4.2 for the anodic film grown on Al-21at.%Nb, the optical band gap of the investigated oxides can be estimated by extrapolating to zero the $(I_{ph}h\nu)^{0.5}$ vs hν plot (E_g= 4.11 eV) (according to eqs. 2.31, 2.38).

For the oxide on this alloy, as well as for those grown on alloys with Nb contents ≤ 55at.%, an exponential decrease in the photocurrent yield (Urbach tail) as a function of photon energy is observed at photon energies lower than the mobility gap (Fig. 4.2c). As already found for several anodic films on valve metals and valve metal alloys [2.49], a possible origin of the trend is the variation of the light absorption coefficient according to eq. 2.32.

An E_0 value slightly higher (~ 4.22 eV) than the mobility gap (4.11 eV) was estimated.

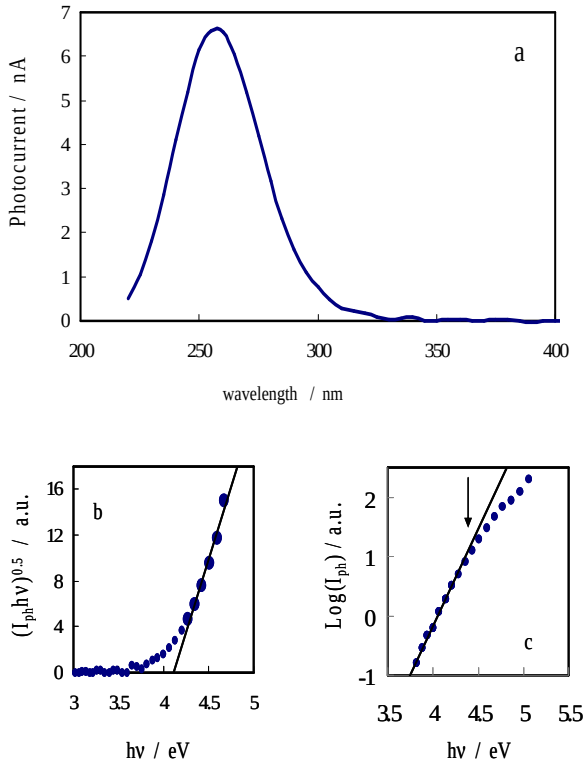

Fig. 4.2 a) Raw photocurrent spectrum relating to anodic film grown to 9V/SCE on Al-21at.%Nb alloy, recorded by polarizing the electrodes at 5 V/SCE in 0.1 M ABE.
b) Band gap estimate by assuming non direct optical transitions and c) Urbach plot.

Figure 4.3 displays the $(I_{ph}h\nu)^{0.5}$ vs hν plots relating to anodic films with different Nb contents. The estimated E_g values show that the optical band gap monotonically changes between the values estimated for the pure oxides (see Table 4.2). This finding suggests that it is possible to tailor the band gap of an anodic oxide by properly selecting the composition of the base alloy.

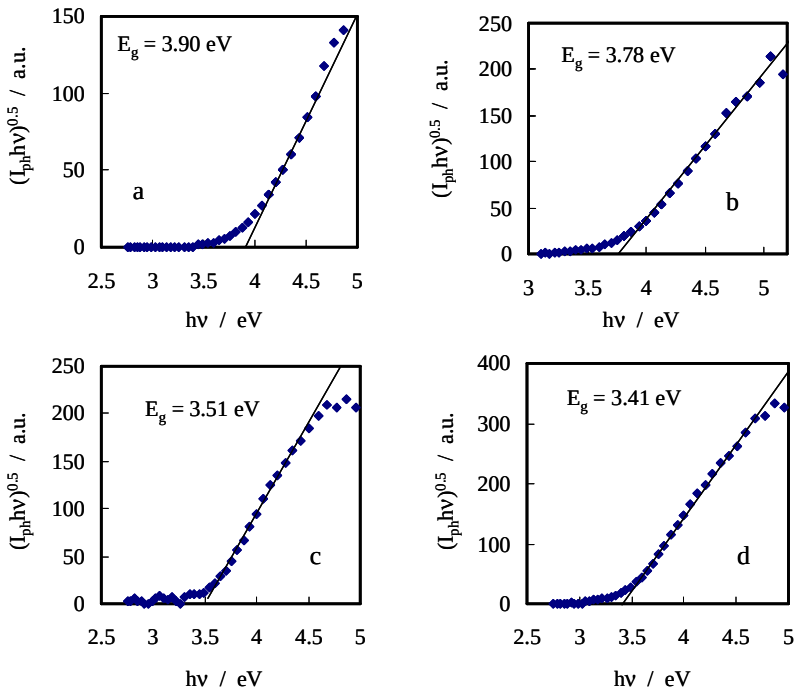

Fig. 4.3 Band gap estimate by assuming non-direct optical transitions relating to anodic films grown to 9 V/SCE on a) Al-40at%Nb, b) Al-55at.%Nb, c) Al-85at%Nb and d) Al-92at.%Nb alloys, recorded by polarizing the electrodes at 5 V/SCE in 0.1 M ABE.

Al-Nb Alloy	21at.%Nb	40at.%Nb	55at.%Nb	66at.%Nb	81at.%Nb	85at.%Nb	92at.%Nb
E_g / eV	4.11	3.90	3.78	3.64	3.52	3.51	3.41

Table 4.2 Optical Band gap values estimated by assuming non-direct optical transitions relating to anodic films grown to 9 V/SCE on Al-Nb alloys.

The photocurrent vs potential curves (photocharacteristics) were recorded by scanning the electrode potential at 10 mV s^{-1} in 0.1 M ABE and by irradiating the mixed oxides at several constant wavelengths. By moving the polarizing voltage

(U_E) toward the cathodic direction, an inversion of the photocurrent sign was revealed in the case of oxides grown on the investigated alloys with a niobium content ≤ 55at.% (see Figs. 4.4 and 4.5), as the sharp change in the phase angle suggests. This behaviour is typical of insulating materials [2.49, 4.10] for which both anodic and cathodic photocurrents can be detected depending on the direction of the imposed electric field, i.e. on the polarizing voltage with respect to the flat band potential, U_{FB}. Thus, the inversion potential V_{inv} can be assumed to be a proxy of the flat band potential. It is important to stress that for films grown on Al-21at.%Nb (see fig. 4.5), the inversion photocurrent potential of the photocharacteristics is more anodic than that estimated from the steady state photocurrent values, owing to the presence of cathodic photocurrent spikes in the low band bending region, i.e. close to the flat band potential.

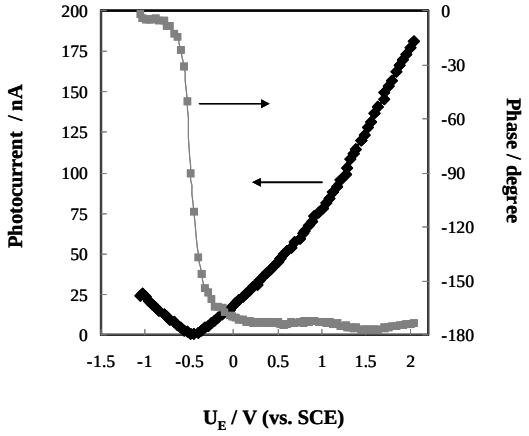

Fig. 4.4 Photocurrent and phase vs potential curves relating to 9V/SCE anodic films grown on Al-55at.%Nb alloy. Irradiating wavelength 270 nm, solution: 0.1 M ABE and potential scan rate 10 mV s^{-1}.

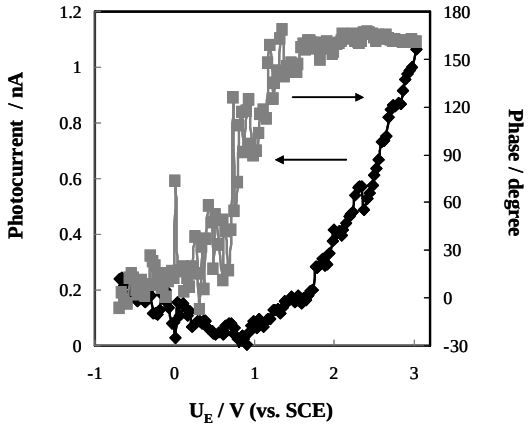

Fig. 4.5 Photocurrent and phase vs potential curves relating to 9V/SCE anodic films grown on Al-21at.%Nb alloy. Irradiating wavelength 270 nm, solution: 0.1 M ABE and potential scan rate 10 mV s^{-1}.

The steady state anodic photocurrent inversion potential for this sample can be located between – 0.6 V (SCE) and -0.8 V (SCE). The discrepancy between the inversion potential values estimated under chopped light (13 Hz) and under steady illumination can be explained by the presence of localized states inside the mobility gap of the oxide, which can behave as traps for the injected photocarriers locally modifying the electric field distribution and the potential drop at oxide/electrolyte interface [4.11].

The presence of cathodic photocurrents allowed the recording of photocurrent spectra at potentials more cathodic than the inversion potential. For anodic films grown on Al-55at.%Nb and on Al-40at.%Nb, the shapes of the cathodic spectra were generally similar to the corresponding anodic ones, revealing estimated band gap values similar to those obtained from the anodic spectra (see Fig. 4.6).

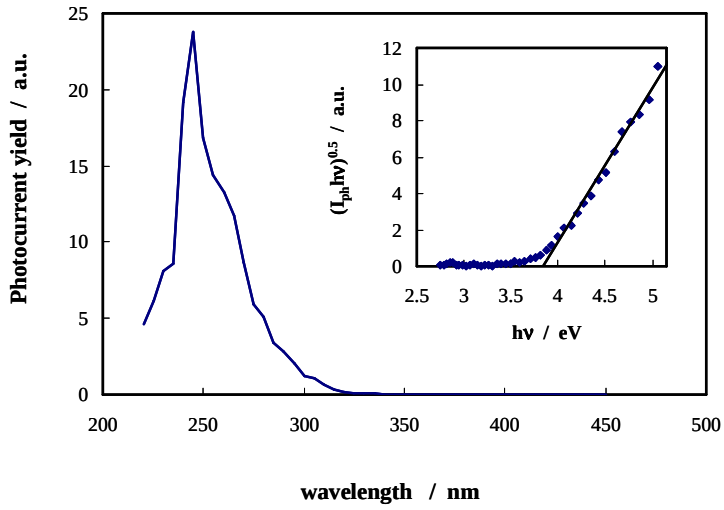

Fig. 4.6 Photocurrent spectrum relating to anodic film grown on Al-55at.%Nb alloy to 9V/SCE, recorded by polarizing the electrodes at -1 V/SCE in 0.1 M ABE. Inset: band gap estimate by assuming non direct optical transitions.

In the case of Al-21at.%Nb, a photocurrent tail appeared at energies lower than the band gap of the corresponding oxide. Cathodic photocurrents at energies below E_g are attributed to photoemission of electrons from the Fermi level of the alloy to the oxide conduction band, with an internal photoemission threshold energy E_{th} = 2.25 ± 0.05 eV (Fig. 4.7) estimated according to Fowler's law (eq. 2.34)

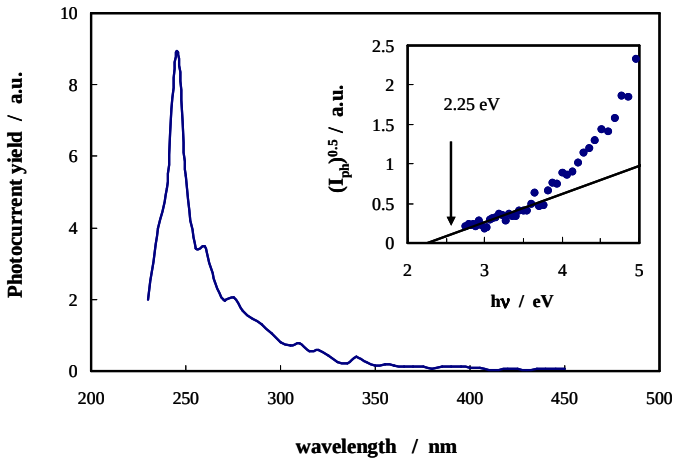

Fig. 4.7 Photocurrent spectrum relating to anodic film grown on Al-21at.%Nb alloy to 9V/SCE, recorded by polarizing the electrodes at -1 V/SCE in 0.1 M ABE. Inset: Fowler plot.

For anodized alloys with Nb contents ≥ 66at.%, only anodic photocurrents were observed, as typical of n-type semiconducting materials and reminiscent of the behaviour of Nb_2O_5 (see Fig. 4.8). In order to estimate the flat band potential of these oxides, the photocharacteristics were fitted according to a power law, $(I_{ph})^n \propto U_E$, and a U_{FB} coincident with the extrapolated potential of zero photocurrent, V*, was assumed [2.1]. The values of n and V* obtained at each wavelength are reported in Table 4.3. According to the data the V* values are not strongly dependent on the oxide composition. The zero photocurrent potentials, estimated for all the investigated alloys, displayed at constant wavelength (λ = 320 nm), a V* value slightly decreasing with decreasing Nb content, reaching a value of - 0.87 V (SCE) for the anodic films grown on alloys with Nb content equal to 66at.%.

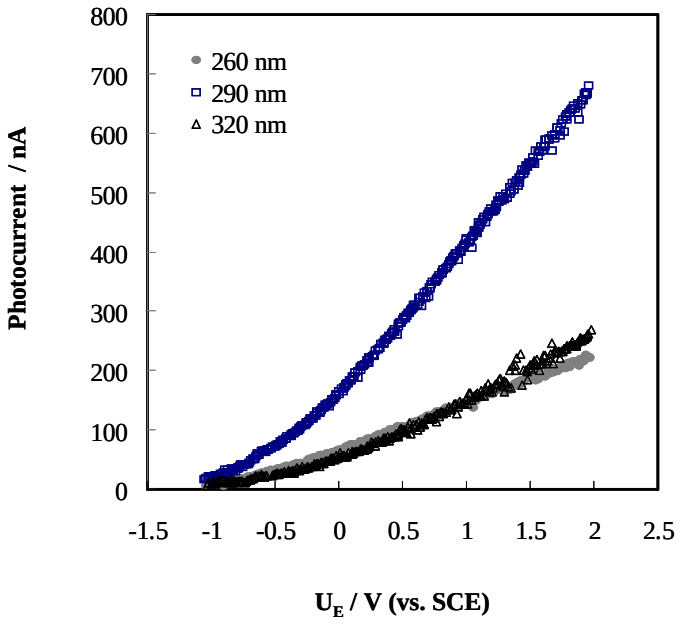

Fig.4.8 Photocurrent vs potential curves relating to 9V/SCE anodic films grown on Al-66at.%Nb alloy.

The disclosed linear or supralinear behaviour (n < 1) over a large potential range, as well as the dependence of n on the wavelength, has been attributed to the presence of initial (geminate) recombination effects of injected photocarriers. Geminate recombination can occur if the thermalization length of the photogenerated electron - hole pairs is too short to prevent recombination of photocarriers during the thermalization process of injected photocarriers. It is typical of optical transitions involving not extended energy levels, owing to a lower mobility of electron carriers in localized states (see Chapter 2 and ref. [2.1]).

Alloy	wavelength / nm	n	V* / V(SCE)
Al-66at%Nb	260	0.975	- 0.88
	290	0.85	- 0.88
	320	0.775	- 0.87
Al-85at%Nb	260	0.95	- 0.81
	290	0.825	- 0.81
	320	0.80	- 0.81
Al-92at%Nb	260	1.25	- 0.77
	290	0.875	- 0.78
	320	0.75	- 0.79

Table 4.3 Parameters obtained by fitting according to power law, $(I_{ph})^n \propto U_E$ the experimental photocharacteristics recorded for anodic films grown to 9 V/SCE on Al-Nb Alloys, at 10 mV s^{-1} in 0.1 M ABE.

4.4.1 Discussion

Al_2O_3 and Nb_2O_5 mixed oxides represent a very intriguing system owing to the distinctly different solid state properties of the component oxides. Al_2O_3 is a wide band gap insulator with a valence band constituted by the occupied O 2p orbitals and a conduction band constituted by the Al 3s - 3p empty orbitals, separated by a high energy gap at least ≥ 6.2 eV [4.1, 4.12], while Nb_2O_5 is an n-type semiconductor with a valence band generated by the (occupied) O 2p orbitals, but with a conduction band comprising mainly the d orbitals of Nb. A band gap of 3.35 ± 0.05 eV is usually reported for anodic Nb_2O_5 [3.9, 4.2]. The study of the photoelectrochemical behaviour of anodic films on sputtering-deposited Al-Nb alloys of different compositions provided evidence that by increasing the Al content in the base alloy the optical band gap monotonically increases. Furthermore, a change from n-type semiconducting to insulating oxide behaviour occurs, at a constant final formation voltage, when the Al content reaches values of ~ 55at%.

The mixed oxide composition is directly related to the base alloy composition and to the migration rates of the metal ions. Al^{3+} and Nb^{5+} have transport numbers t > 0 in Al_2O_3 and Nb_2O_5 respectively (t_{Al3+} = 0.4 and t_{Nb5+} = 0.23) [4.13]. During anodizing of Al-Nb alloys, Al^{3+} and Nb^{5+} ions migrate toward the oxide/electrolyte interface at similar rates [4.7], with simultaneous migration of O^{2-} toward the metal/oxide interface. Fig. 4.9 shows the RBS spectra relating to oxides grown to 150 V in 0.1 mol dm^{-3} ABE on Al-Nb alloys with Nb contents ≥ 66at.%. The niobium contents of the oxides (considering cations only) are close to the contents in the alloys to an accuracy of ~ 1 at.%. Furthermore, a close similarity between the compositions of the anodic film and the alloy has also been shown for Al-Nb alloys of lower Nb contents [4.7].

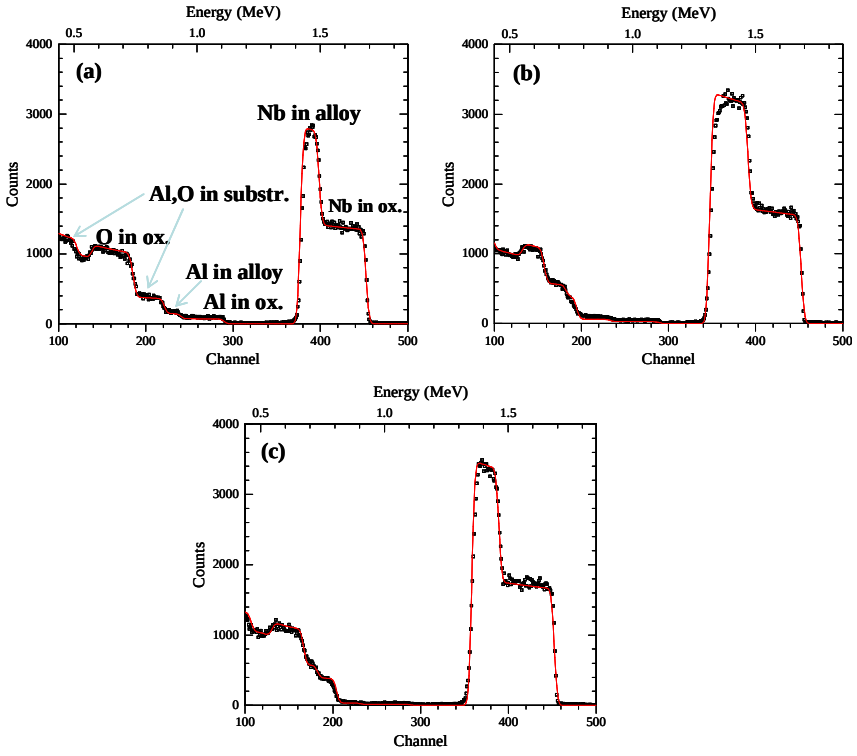

Fig. 4.9 RBS spectra relating to anodic films grown to 150 V on a) Al-66at.%Nb b) Al-85at.%Nb c) Al-92at.%Nb .

The experimental E_g values are displayed in Fig. 4.10 as a function of $(\chi_M - \chi_O)^2$, assuming $\chi_O = 3.5$, $\chi_{Al} = 1.50$ and $\chi_{Nb} = 1.615$ (value recent used for Nb in Nb-Ta mixed oxides, ref. 4.14) in agreement with the values reported in the Pauling scale [3.13]. In the same Figure, the dashed lines corresponding to eq. 2.41 and 2.42 are shown. Comparison between the experimental E_g values and those expected on the basis of the correlations shows that values are far from those predicted by eq. 2.41. In contrast, the experimental E_g differs from the values expected according to eq. 2.42 by an amount which is in a range of ΔE_{am} compatible with theoretical expectations [2.36]. This finding suggests that the d-d metals correlation could hold also for Al-Nb mixed oxides, provided that the percentage of d-metal in the film is higher than, or equal to 21at.%, which is very close to the value found for photoactive Al-W mixed oxides [2.52].

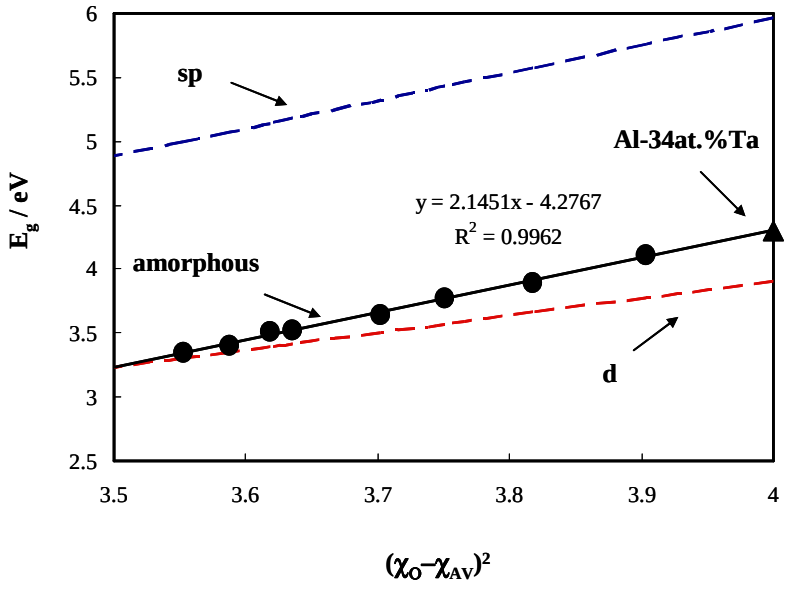

Fig. 4.10 Optical band gap vs $(\chi_O - \chi_{Av})^2$. ●: experimental values ─: quadratic best fitting curves ---: theoretical prediction for sp and d metal oxides, according to eq. 2.40.

On the other hand, a careful inspection of Fig. 4.10 reveals that the experimental points can be fitted satisfactorily by a straight line of slope (2.1451 eV) that is close to that of eq. 2.41, while the coefficient B (4.2767) is almost equal to the sum of the two corresponding terms in eqs. 2.41 and 2.42. Moreover, by extrapolating to $(\chi_O - \chi_{Al})^2 = 4$ (i.e. $x_{Al} = 1$), an optical band gap value of 4.3 eV can be estimated. This value departs significantly from the E_g^{opt} values reported for both amorphous [4.15] and crystalline Al_2O_3, [4.1, 4.12], but is almost coincident with the band gap estimated for the anodic oxide on Al-34at.%Ta alloy [2.52]. This last E_g^{opt} value can be considered as the band gap of an amorphous oxide grown on a sp-d-metal alloy having the same electronegativity parameter as aluminium ($\chi = 1.5$).

In order to explain the compositional dependence of the optical band gap reported in Fig. 4.10, it is recalled that in the case of random semiconducting alloys E_g of mixed alloys are traditionally fitted, as a function of their composition, according to a bowing formula [4.16]:

$$E_g(x) = E_{gi}(1-x) + E_{gj}x - b\,x\,(1-x) \qquad 4.1a$$

where E_{gi} and E_{gj} represent the band gaps of pure compounds (at x = 0 and x = 1, respectively) and b is the bowing parameter, which can be derived once the experimental band gap value of the alloy at x = 0.5 is known. After trivial algebraic manipulation, eq. 4.1a can be rewritten as:

$$E_g(x) = E_{gi} + ax + b\,x^2 \qquad 4.1b$$

with $a = (E_{gj} - E_{gi} - b)$. In Fig. 4.11, the experimental band gap values of the investigated Al-Nb mixed oxides are compared with those estimated according to eq. 4.1a. A value for E_g of 3.35 eV was assumed for amorphous anodic niobia, according to the experimental values estimated in this work. A value for E_g of 6.4 eV was assumed for amorphous alumina in the hypothesis of non-direct optical transitions [4.15]. The employed bowing parameter (b = 4.3 eV) was calculated by using eq. (4.1b) with E_g = 3.80 eV for $x_{Nb} = 0.50$. This last value was estimated by

assuming a linear interpolation of E_g values between the two measured E_g at composition x = 0.4 (3.9 eV) and x = 0.55 (3.75 eV).

It is evident from the data in Fig. 4.11 that eqs. (4.1a,b) provide a very poor fitting of the experimental data for Nb contents ≤ 20 at.%, if we assume as the end point at x = 1 the band gap of 6.4 eV. The fitting is worse if larger E_g values are assumed for Al_2O_3, such as those reported for crystalline Al_2O_3 (7.2 – 8.8 eV) [4.1].

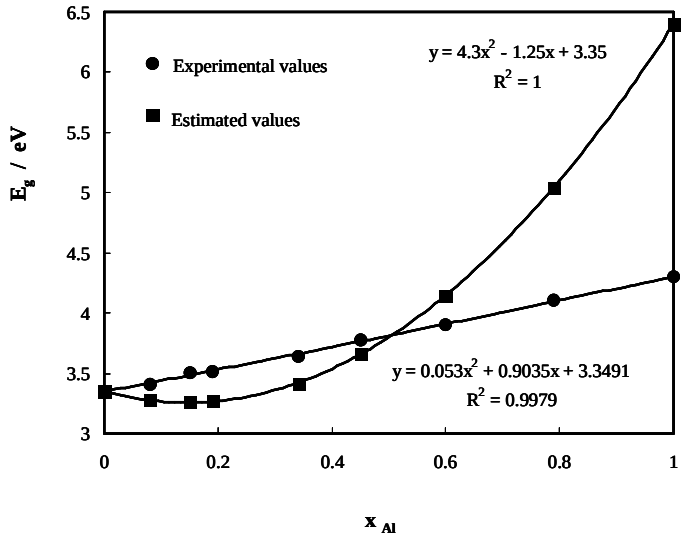

Fig. 4.11 Optical Band gap as a function of the Al cation fraction, x_{Al}. ●: experimental values and ■: estimated values, according to eq. 4.1a.

On the other hand, we have recently shown ref. [4.14] that eq. (4.1b) is able to account for the dependence of E_g on composition for Ti-Zr and Fe-Ti mixed oxides. In fact after substitution of eq. 2.43 in eq. 2.40 and simple algebraic manipulation, we can write for a mixed semiconducting oxide the following relation [4.14]:

$$E_g(x) = E_{g,i} + 2Ax_j\,(\chi_i - \chi_j)\,(\chi_{an} - \chi_i) + Ax_j^2(\chi_j - \chi_i)^2 \qquad 4.2a$$

which recalls the standard bowing equation above reported. A direct comparison of eqs. 4.1b and 4.2a yields the following expressions for the linear and quadratic coefficients:

$$b = A(\chi_i - \chi_j)^2 \qquad 4.2b$$

$$a = 2\,A(\chi_i - \chi_j)(\chi_O - \chi_i) \qquad 4.2c$$

In the cases of Ti-Zr and Fe-Ti alloys, the involved metals belong to the d block of the Periodic Table, unlike Al-Nb alloys, due to the sp character of aluminium. For Al-Nb alloys, by direct substitution of the respective $\chi_{i,j}$ and A values derived above, we obtain b = 0.0284 and a = 0.93. Both values compare quite well with the experimentally-derived ones equal to b_{exp} = 0.053 and a_{exp} = 0.904 respectively. A still better agreement with the experimental values is obtained by assuming for Al-34at.%Ta a band gap value of 4.29 which is within the experimental uncertainty (± 0.025 eV) embodied in the measured. E_g^{opt} Equation 4.2b shows that the bowing coefficient b is always positive, whilst the linear term can be positive or negative depending on the sign of the term $(\chi_i - \chi_j)$. The linear term will be positive (negative) if E_{gi} is the band gap of the oxide with higher (lower) χ parameter. According to our correlation, lower band gap materials have a higher Pauling electronegativity parameter and vice versa. For mixed oxides emerge that the value of bowing parameter is a function of the nature of the cations present in the semiconducting oxides and that an almost linear dependence of the band gap on the composition parameter is expected provided that the difference of the electronegativities ($\Delta\chi_{ij}$) of the cations present in the oxides is small ($b < 0.1$ for $\Delta\chi_{ij} \leq 0.2$).

Knowledge of the band gap and flat band potential enables consideration of the energetics of the alloy/oxide/electrolyte interfaces, which is of key importance for the possible practical application of these films in electrolytic capacitors or in solid state junctions (MIM capacitors and memristors).

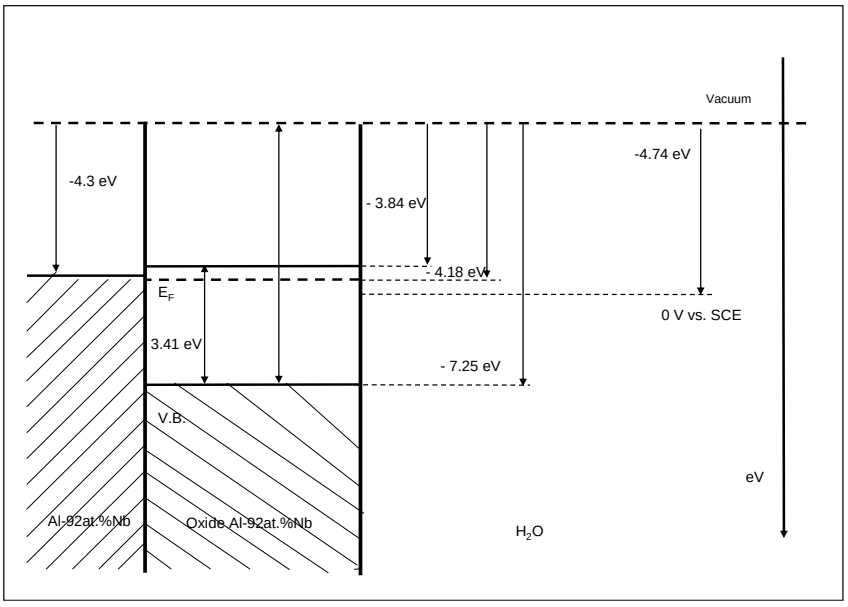

Fig. 4.12 Sketch of the energetic levels of metal/oxide/electrolyte interface for anodic films grown on Al-92at.%Nb at pH of zero charge.

Fig. 4.12 shows schematically the energetics of the anodic film on Al-92at.%Nb using for U_{FB} the proxy value given by the zeroing photocurrent potential V*. For this oxide a comparison of V* (V* = - 0.79V/SCE) with the flat band potential as derived from the fitting of differential admittance curves (see paragraph 4.6 and ref. [4.9]) showed a very good agreement, so that for all semiconducting films the V* value at longer wavelength was used for the location of Fermi level of the oxide in the vacuum scale, according to the relationship [2.1], $E_F = -|e|U_{fb}(rif, abs)$.

In Fig. 4.12 we have located the level of SCE reference electrode at – 4.74 eV vs vacuum, assuming for the normal hydrogen electrode a value of - 4.5 eV, as reported in the literature [4.17]. We have to mention that this value is also in between those reported in literature by Bockris (-4.6 eV in ref. [2.21]) and by Pleskov (- 4.4 eV in ref. [2.19]).

In order to have a complete image of the relative energy levels location for the investigated alloys, we need to estimate the band edges position as a function of the

Nb content. We can follow the procedure described for the anodic film on Al-92at.%Nb for all the semiconducting oxides. The first step is to estimate the E_F for the investigated oxides at the respective pH of zero charge, pH_{pzc}, in order to cancel the effect of a different charge density on the oxides' surface. At this aim we have used the following eq.

$$E_F(pH_{pzc}) = -4.74 - |e|U_{FB}(SCE) + 0.059(pH_{pzc} - 8.5) \qquad 4.3$$

The employment of eq. 4.3 requires the knowledge of pH_{pzc} as a function of the oxide composition, which was determined by averaging for the Al and Nb molar fraction the pH_{pzc} of pure oxides [3.21, 4.19]. Assuming $pH_{pzc} \sim 4.1$ and $pH_{pzc} \sim 9.5$ for niobia and for alumina respectively, for semiconducting films on Nb rich alloys U_{fb} at pH_{pzc} was found to change linearly as a function of pH_{pzc} with a slope of ~ 119 mV/decade, as expected according to ref. [3.21, 4.19] .

Once the Fermi level of each mixed oxide was estimated, we located the conduction band mobility edge using the relationship (according to eq. 2.14 and ref. [2.1, 2.4]):

$$\Delta E_F = -k_B T \ln(\omega_c \tau_0) \qquad 4.4$$

where $\Delta E_F = (E_c - E_F)_{bulk}$, τ_0 is the capture/emission time of electronic carriers (usually assumed 10^{-12} s) and $\omega_c = 2\pi f_c$ represents the cut-off frequency (in rad s^{-1}), i.e. the frequency where an almost complete flattening of the differential capacitance vs voltage curve is observed [2.4].

In the case of Al-92at%Nb a value of ΔE_F equal to 0.35 eV has been estimated by fitting the differential admittance curves in a large range of frequency ($10^2 \cdot Hz \leq f \leq 2 \cdot 10^4$ Hz) (see section 4.6 and ref. [4.9]). This ΔE_F value is almost coincident to that estimated for pure niobia anodic film (0.335 eV) in ref. [2.1, 2.4]. The corresponding estimated cut-off frequencies are respectively $3.35 \cdot 10^5$ Hz and $1.86 \cdot 10^5$ Hz for pure niobium oxide and Al-92at.%Nb mixed oxide respectively. As for the other semiconducting films we located, by analogous procedure, the flat band

potential at pH_{pzc} and from the capacitance vs potential curves at different frequencies we estimated the cut-off frequencies (f ~ 4 kHz and f ~ 2 kHz for anodic film on 85at.%Nb and 66at.%Nb respectively) from which the ΔE_F values have been derived according to eq. 4.4 (see section 4.6 and ref. [4.9]).

The results of such calculations are reported in tabs. 4.4 and 4.5 together with the estimated energy levels E_{CBM} for the conduction band mobility edge in the vacuum scale. By using the measured optical band gap we have been able to locate in the same scale the E_{VBM} levels of different semiconducting oxides. Since the reported Fermi levels, with respect to the vacuum, for pure Al and Nb are very close (see ref. [4.20]) a constant value (E_F = - 4.30 eV) was employed for all investigated Al-Nb alloys.

According to this an almost constant value of -7.28 ± 0.03eV is derived for the location of valence band mobility edge of all semiconducting oxides (see Table 4.5). Such a value is quite in agreement with the value reported in literature for the valence band edge of transition metal oxides essentially derived from 2p oxygen ions orbitals [2.49, 4.21, 4.22].

Alloy	U_{FB} at pH = 8.5 (V vs. SCE)	pH_{pzc}	U_{FB} at pH_{pzc} (V vs. SCE)	E_F eV vs vacuum	Cut off frequency (kHz)	E_C eV
Nb	- 0.76	4.1	- 0.50	- 4.24	334	0.335
Al-92at.%Nb	- 0.79	4.53	- 0.56	- 4.19	186	0.35
Al-85at.%Nb	- 0.81	4.91	- 0.60	- 4.14	4	0.448
Al-81at.%Nb	- 0.82	5.13	- 0.63	- 4.11	4	0.448
Al-66at.%Nb	- 0.87	5.94	- 0.72	- 4.02	2	0.466

Table 4.4 - Estimated parameters for semiconducting mixed oxides grown on Al-Nb alloys.

As for the anodic oxide formed on Al-Nb alloy with Nb content $\leq$ 55at%, owing to their insulating nature, the determination of cut-off frequency was not accessible in the exploited range of frequency (10 Hz – 20 kHz), so that it was impossible to get an estimate of the ΔE_F value for these oxides. However for these insulating oxides no large differences are expected in the energy levels of the O 2p orbitals as a function of Nb content into the mixed oxides in analogy with that suggested for other mixed oxides [4.20]. This suggestion is supported by the fact that in the case of Al-34at%Ta an internal photoemission threshold equal to 1.45 eV has been previously reported [2.52] which poses the E_{CBM} energy level of the mixed oxide grown on such an alloy at around -2.82 eV if a Fermi level of -4.27 eV is assumed for the alloy. According to this and taking into account the band gap value of 4.30 eV for the anodic film (see table 4.5) we can locate the E_{VBM} of the mixed oxide on Al-34at%Ta at -7.12 eV below the vacuum level not too far from the value of -7.27 eV estimated for the E_{VBM} of the mixed Al-Nb semiconducting oxides. By taking into account the experimental uncertainty embodied on the estimation of the physical quantities like: metal work function, oxide optical band gap, ΔE_F it seems reasonable to assume an almost constant E_{VBM} level (O 2p valence band of the anodic mixed oxides) equal to -7.27 ± 0.2eV in the vacuum scale also for insulating anodic films grown on Al-55at%Nb and Al-40at%Nb alloys. The values of E_{CBM} for these oxides reported in table 4.5 have been estimated according to this assumption and allowed to get the schematic representation of the band gap of fig. 4.13.

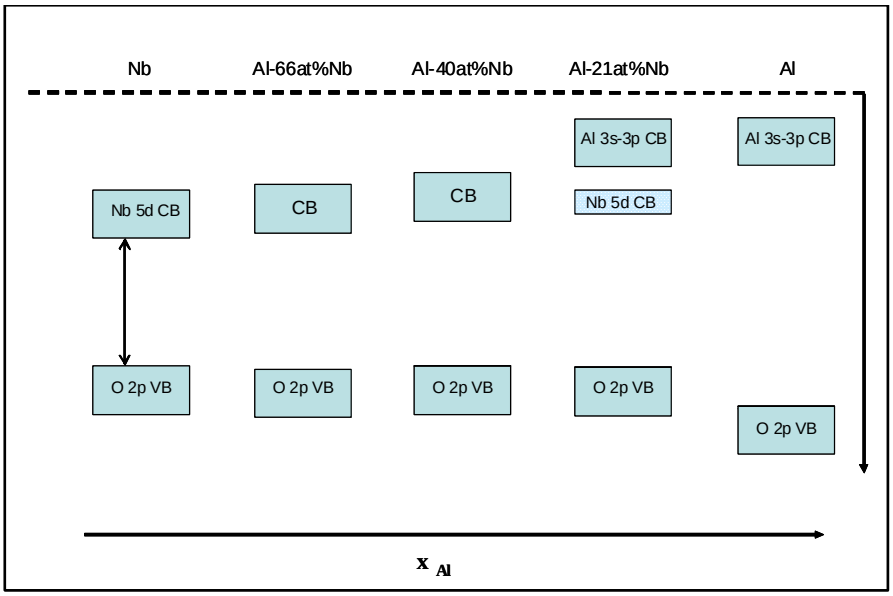

Fig. 4.13 Schematic representation of the band edges and Niobium alloying states in oxides grown on pure Nb, Al-Nb alloys and pure Al.

Alloy	E_{CBM} eV vs vacuum	E_{VBM} eV vs vacuum
Nb	- 3.89	- 7.24
Al-92at.%Nb	- 3.84	- 7.25
Al-85at.%Nb	- 3.79	- 7.30
Al-81at.%Nb	- 3.76	- 7.28
Al-66at.%Nb	- 3.67	- 7.31
Al-55at.%Nb	- 3.49	- 7.27
Al-40at.%Nb	- 3.37	- 7.27
Al-21at.%Nb	- 3.16	- 7.27
Al-34at.%Ta	- 2.82	- 7.12

Table 4.5 - E_{CBM} and E_{VBM} values (vs. vacuum) for mixed oxides grown on Al-Nb alloys.

On the other hand as for the anodic film on Al-21at.%Nb the conduction band edge, E_{CBM}, can be located at -2.05 eV by using the Fowler threshold for the internal electron photoemission process (E_{th} = 2.25 eV) reported in Fig. 4.7 and the value of E_F = - 4.3 eV assumed for the alloys.

However, location of the valence band edge 4.11 eV (i.e. E_g) below the CB band edge of the oxide film causes the energy level of the O 2p orbitals (with respect to vacuum) to be quite far (- 6.16 eV) from that estimated for oxide grown on Al-Nb alloys with Nb $\geq$ 40at% (-7.27 eV) or on Al-34at.%Ta (-7.12 eV) alloy. In order to overcome such a discrepancy and by recalling that internal photoemission threshold values near to the above reported one have been measured at the Al/Al_2O_3 interface for anodic or CVD alumina film [4.15a, 4.23] we suggest that the estimated Fowler threshold in Fig. 4.7 accounts for an internal photoelectron injection process into the conduction band levels of anodic alumina generated by Al 3s-3p empty orbitals. In this scheme, the indirect (non-direct) optical transitions of the anodic photocurrent spectra involve as final states the energy levels of a narrow d-band generated by Nb orbitals located 4.11 eV above the valence band i.e. at around -3.16 eV below vacuum. These results are in quite good agreement with theoretical studies reported in ref. [4.24] showing that the insertion of Nb impurities into Al_2O_3 matrix originates "a shallow impurity band approximately located 1eV below the bottom of conduction band of alumina". According to these results, it can be assumed that the band gap variations of Al-Nb mixed oxides, in the range of Al contents between 0 and 80at.%, is attributable to the variation of the conduction band mobility edge, E_{CBM}, of mixed Nb-Al oxide.

For Nb content in the sputtered alloy around 10at.% we have not been able to detect any anodic photocurrent by illuminating the anodic oxide with photons of energy higher than 5.3 eV (λ = 230 nm) so fixing the band gap of the formed mixed oxide above such a value. In this range of oxide composition the above proposed correlation fails to predict the correct band gap value of mixed oxide and probably the use of eq. 2.41 together with the average cationic electronegativity could provide a better estimate of band gap values for the aluminum rich mixed oxides.

Finally we like to stress that a value of 6.4 eV for the optical gap of amorphous ALD aluminum oxide is compatible with a value of electronegativity parameter for Al equal to 1.45 (a value still in agreement with that of the original Pauling's scale: $\chi_{Al} = 1.5 \pm 0.05$). The 6.4 eV value of the amorphous anodic film is not too far from the experimental value (7.2 eV, direct band gap) reported in ref. [4.1] for γ-Al_2O_3. We like to mention that a still lower optical band gap value could be experimentally extrapolated in ref. [4.1], in the hypothesis of indirect optical transitions, as suggested by the non-zero optical absorption values below 7.2 eV reported in French's work [4.1]. Lower optical band gap values for anodic alumina films could be traced, however, to different band structures of amorphous and crystalline alumina films as suggested for other oxides [2.1, 2.36, 4.25] .

In summary, the solid state properties of Al-Nb mixed oxides grown by anodizing Al-Nb magnetron-sputtering alloys were studied as a function of their composition. A detailed photoelectrochemical investigation allowed the band gap, flat band potential and conductivity type of these oxides to be determined. By increasing the Al content into the oxide, E_g increases monotonically and a transition from insulating (Nb content $\leq$ 55at.%) to n-type semiconducting material (Nb content $\geq$ 66at.%) was revealed for thin anodic films. The dependence of the band gap on the composition of mixed sp-d metal oxides has been rationalised by using a semi-empirical correlation between the difference of electronegativity and band gap of oxides proposed in the literature some years ago and recently tested for regular d-d metal mixed oxides. A chemical approach to the estimate of bowing coefficient has been suggested and its value seems to confirm a theoretical suggestion put forward several years ago by Wei and Zunger for explaining the optical band gap behaviour of semiconductor alloys as a function of the cation composition [4.26]. According to these authors a bowing coefficient "relatively small and constant" can be expected for semiconductor alloys in a composition range x where a bandlike region still exist, while "relatively larger and composition dependent" bowing coefficient can be expected in the impurity-like region. Our experimental results, including the region of lower ($\leq$ 21at%) Nb content where large variations in the optical band gap values can be predicted according to our experimental results, seem to confirm the

Wei-Zunger's suggestion also for mixed oxides belonging to different mains groups (s.p or d). Further investigations are now in progress aimed at testing the proposed correlations.

4.5 Dielectric properties

In Fig. 4.14 we report the measured capacitance as a function of the Nb content into the base alloy, recorded with a.c. frequency of 1 kHz in 0.2 M Na_2HPO_4 (pH ~ 8.5). A first qualitative information arising from Fig. 4.14 is that for the anodic oxides grown on Al-Nb alloys with a Nb content ≤ 55at.% the measured capacitance, C, is almost independent on the applied potential, as expected for insulating material. In contrast, for higher niobium content C sensitively increases by moving the polarizing voltage toward the cathodic direction, as typical of n-type semiconducting material. This behaviour compares well with the results reported in section 4.4 and in ref. [4.8] where the photoelectrochemical investigation evidenced a transition from insulating (Nb ≤ 55at.%) to n-type semiconducting material (Nb ≥ 66at.%).

For the anodic films with insulating behaviour, grown on alloys with a Nb content ≤ 55at.%, it is possible to use the following equation:

$$C = \frac{\varepsilon\varepsilon_0}{d} \qquad 4.5$$

where ε_r is the oxide dielectric constant, ε_0 is the vacuum permittivity and d_{ox} is the oxide thickness.

At higher Nb content a sensitive increase in the measured capacitance is observed with decreasing frequency at constant potential or by decreasing the electrode potential at constant frequency (see Fig. 4.14b). This behaviour becomes more evident with increasing Nb content into the film. In Fig. 4.15 we report the squared reciprocal of the measured series capacitance as a function of the potential

for 9 V anodic film grown on the richest Nb alloy, i.e. Al-92at.%Nb, recorded in 0.2 M Na_2HPO_4 (pH ~ 8.5) at different a.c. signal frequencies.

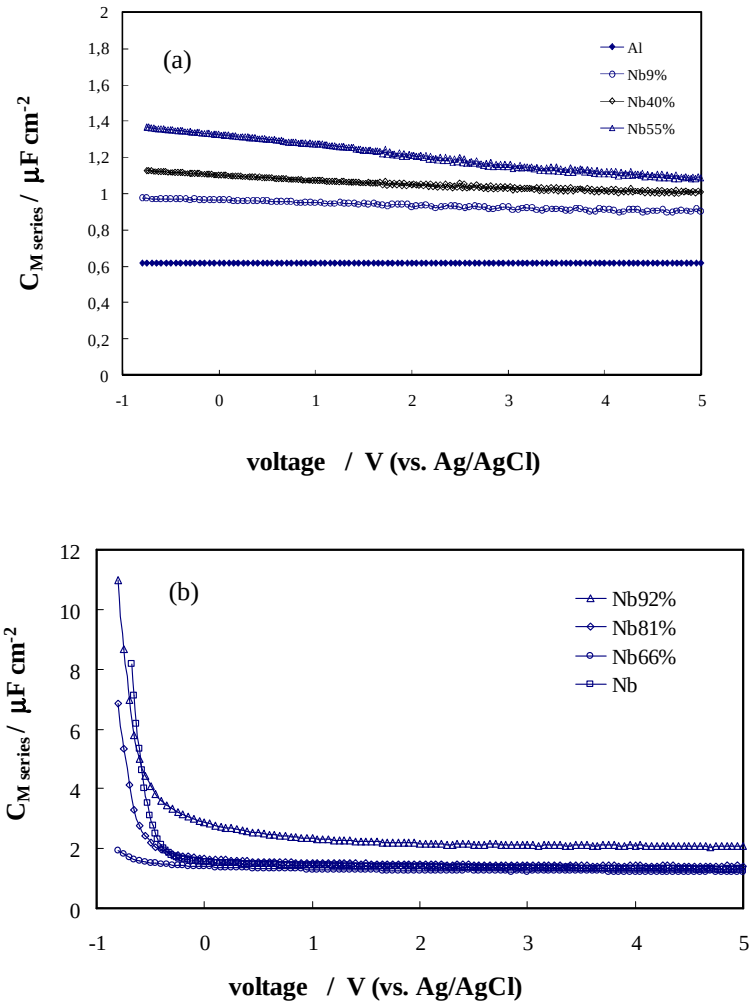

Fig. 4.14 Measured series capacitance vs potential curves for Al-Nb mixed oxides as a function of composition. $v_{a.c.}$ frequency = 1 kHz and solution: 0.2 M Na_2HPO_4 (pH ~ 8.5).

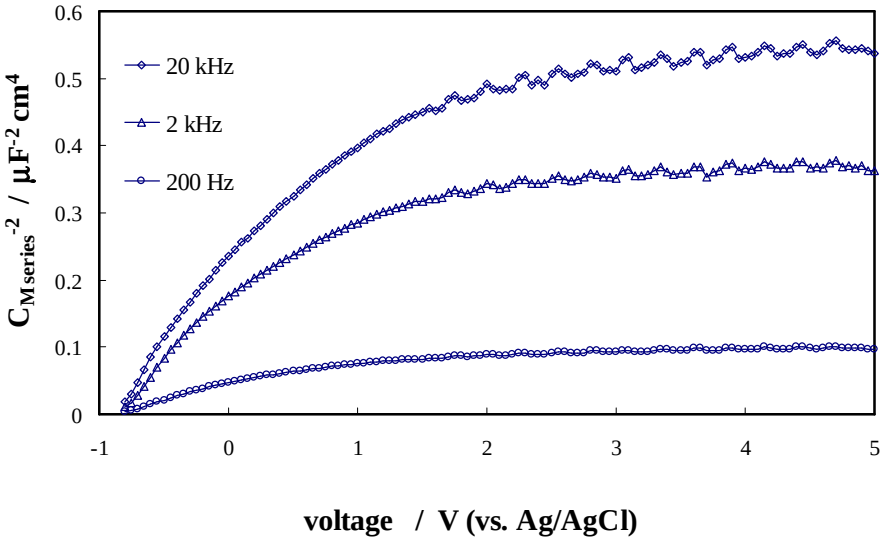

Fig. 4.15 Measured series differential capacitance relating to 9 V anodic film grown on Al-92at.%Nb alloy, recorded in 0.2 M Na_2HPO_4 (pH ~ 8.5) at different a.c. signal frequencies.

The comparison of the curves reported in Fig. 4.15 shows that the measured capacitance is also frequency dependent. Such a behaviour does not agree with the simple M-S theory.

In order to get reliable quantitative information on the dielectric constant, thickness and flat band potential of the investigated n-type SC oxides, the dependence of the admittance component on both the electrode potential and a.c. signal frequency was studied in the frame of the theory of amorphous semiconductor Schottky barrier (see Chapter 2 and ref. 2.1-2.4).

In order to fit C_{SC} and G_{SC} according to eq. 2.19 and 2.20b, we need to extract the differential impedance of the semiconducting oxide space charge region, Z_{SC}, from the overall measured impedance by fitting the EIS spectra recorded at several

electrode potentials. We modelled the metal/oxide/electrolyte interface according to an electrical equivalent circuit of Fig. 4.16a.

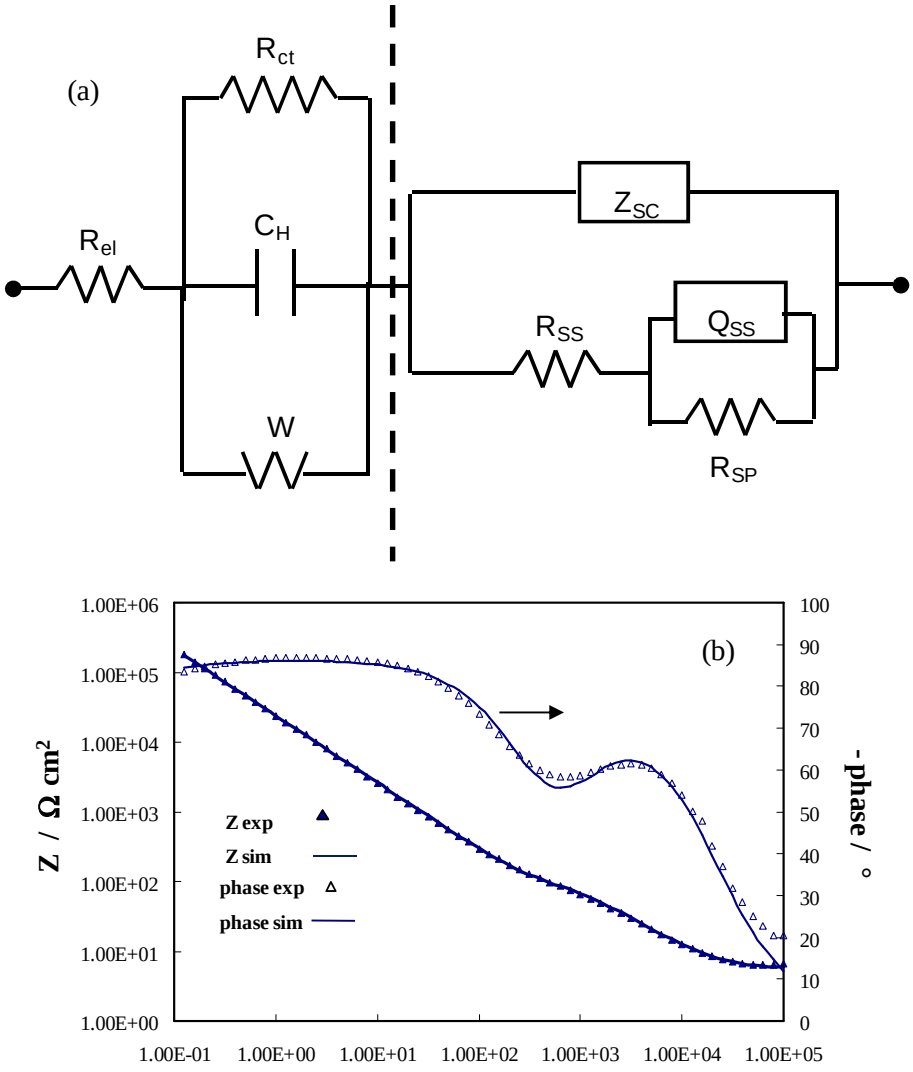

Fig. 4.16 (a) Electrical equivalent circuit employed to model metal/oxide/electrolyte interface (see text for the meaning of the symbols); (b) EIS spectrum in the Bode representation relating to anodic film grown to 9 V on Al-92at.%Nb, recorded by polarizing the film at 3V vs Ag/AgCl in 0.2 M Na_2HPO_4.

The latter consists of a first part (left side in Fig. 4.16a) accounting for the oxide/electrolyte interface, and a second part (right side in Fig. 4.16a) accounting for the a-SC space charge region. The oxide/electrolyte interface was modelled by a modified Randles circuit, where R_{el} is the electrolyte resistance, R_{ct} is the charge transfer resistance, which was kept constant during the best fitting procedure (1 $M\Omega\ cm^2$) in agreement with the blocking character of the oxide in the exploited potential range. C_H is the double layer capacitance, kept constant at 20 $\mu F\ cm^{-2}$.

With respect to the classical Randles circuit a Warburg element was inserted in parallel with both C_H and R_{ct} as suggested in by Abe and co-workers for TiO_2/electrolyte interface [4.27]. In refs. [4.28-4.29] the Warburg element is used in series with a capacitance, C_a, to account for the adsorption/desorption charge processes occurring at the oxide/electrolyte interface owing to the acid/base equilibrium reaction involving H^+/OH^- ions in solution. However, according to the results arising from the fitting procedure, the simplest Abe's circuit seems to better fit the experimental EIS spectra, and allows a good fitting of the differential admittance curves, as detailed described below. Moreover, even by inserting C_a (~ 90 $\mu F\ cm^{-2}$) in the equivalent circuit of Fig. 4.16a, not appreciable differences are found in the derived DOS distribution.

Concerning the right side part of the equivalent circuit, the impedance of the semiconductor, Z_{SC}, is in parallel with an arm introduced to account for the presence of surface states (see Fig. 4.16a). R_{SS} and R_{SP} account for the resistance to electronic transfer via surface states, while Q_{SS} accounts mainly for the surface states contribution to the measured capacitance. Actually, we believe that the use of constant phase elements instead of pure capacitors for Q_{SS} is a better and physically grounded choice if we consider that owing to the amorphous nature of the investigated oxide a mono-energetic surface state as well as a frequency independent space charge region should be a very poor approximation of the electronic properties of the amorphous semiconductor. According to this the equivalent circuit of the a-SC space-charge region is now analogous to that originally proposed by Oskam et al., for the single crystal p-GaAs/electrolyte interface [4.30], after substitution of the

pure capacitance (C_{SC} and C_{SS}) with the CPE element. The best-fitting values of R_{SP} elements decreased largely (~ one order of magnitude) with increasing electrode potential whilst the R_{SS} element remained almost constant . In absence of the arm ($R_{SS}(R_{SP}Q_{SS})$) it was impossible to get a good fitting of the impedance spectra.

A procedure analogous to that previously reported for thin films of amorphous anodic niobia was followed to take into account the influence of the arm ($R_{SS}(R_{SP}Q_{SS})$) on the impedance of the amorphous semiconductor [2.4a]. Both components of the Z_{SC} were obtained from the measured differential admittance (DA) data and according to the equivalent circuit of Fig. 4.16a, by subtracting to the measured impedance firstly the contribution of the oxide/electrolyte interface, and then the contribution of the parallel arm ($R_{SS}(R_{SP}Q_{SS})$) to the residual impedance.

In Fig. 4.16b we show the EIS spectrum in the Bode representation relating to the anodic film grown to 9 V on Al-92at.%Nb, recorded by polarizing the film at 3V vs SSC in 0.2 M Na_2HPO_4. The continuous lines overlapped to the experimental points show the simulated dependence of the impedance modulus, $|Z|$, and phase angle, ϕ, according to the equivalent circuit of Fig. 4.16a and the fitting parameters reported in table 4.6. The validity of the EIS data was verified by the application of the Kramers-Kronig transformations, as explained in ref. [4.31].

U_E / V vs. Ag/AgCl	R_{el} Ω cm^2	R_{ct} Ω cm^2	C_H F cm^{-2}	W S $s^{0.5}$ cm^{-2}	R_{SS} Ω cm^2	R_{SP} Ω cm^2	Q_{SS} S $s^{0.5}$ cm^{-2}	n
1	5.46	$1\cdot10^6$	$20\cdot10^{-6}$	0.0029	126	$6.7\cdot10^6$	$4.06\cdot10^{-6}$	0.975
3	5.46	$1\cdot10^6$	$20\cdot10^{-6}$	0.0029	132	$6.6\cdot10^5$	$3.32\cdot10^{-6}$	0.975

Table 4.6 Fitting parameters relating to EIS Spectra of anodic films grown on Al-92at.%Nb, using equivalent electric circuit of figure 4.16a.

The obtained C_{SC} and G_{SC} were then fitted according to eqs. 2.19 and 2.20, as shown in Fig. 4.17.

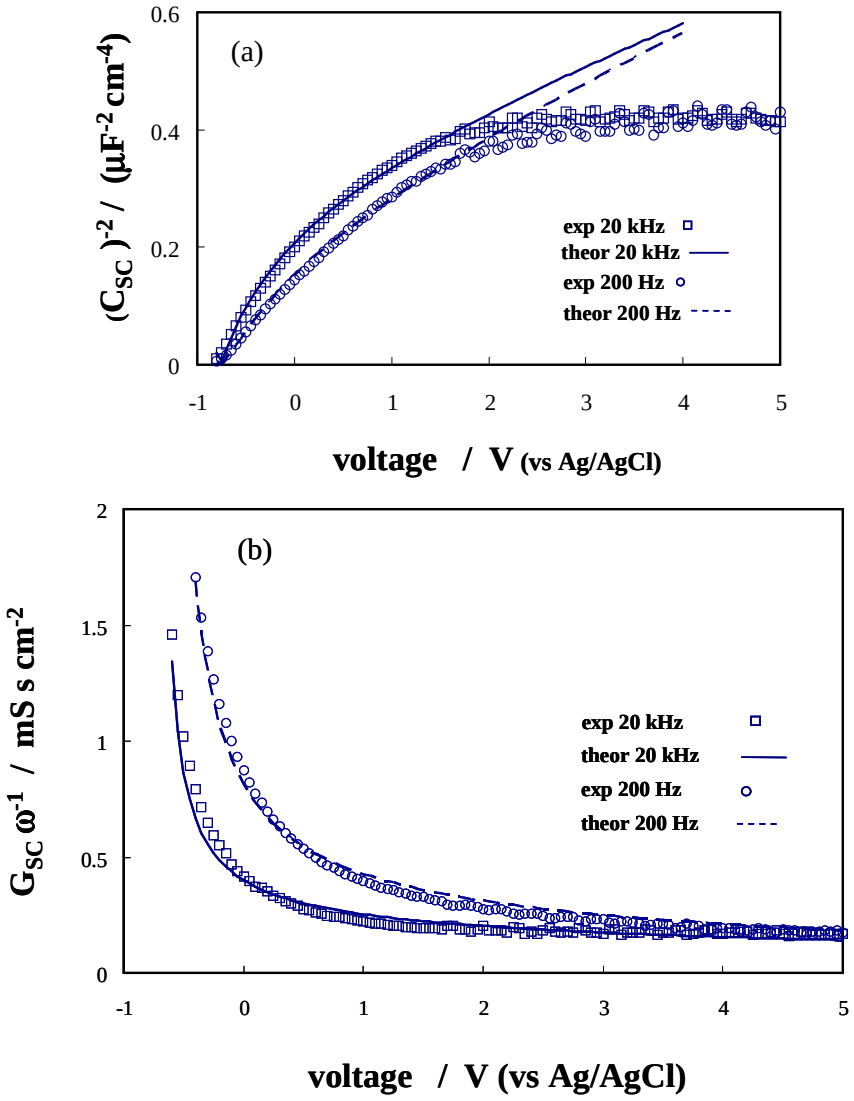

Fig. 4.17 Fitting of the experimental admittance curves relating to anodic film grown on Al-92at.%Nb (f = 20 kHz and 200 Hz, and sol: 0.2 M Na_2HPO_4) with U_{FB} = −0.80 ± 0.025 V vs Ag/AgCl, $e\psi_C$ (20 kHz) = 0.104 eV and $e\psi_C$ (200 Hz) = 0.224 eV, ε = 49. a) $(C_{SC})^{-2}$ vs. U_E and b) $G_{SC}\omega^{-1}$ vs. U_E.

It is interesting to stress that the value of static zero-field dielectric constant (ε (0) = 49) successfully used in the fitting procedure is close to that estimated by averaging according to the film composition the dielectric constant of anodic niobia (53 according to refs. [3.9, 4.2-4.3]) and that of alumina (ε = 9). We have also fitted the curves of Fig. 4.17 with a field dependent dielectric constant according to the following eq. 4.6:

$$\varepsilon\ (E_{av}) = \varepsilon\ (0)(1 - \gamma E_{av}) \qquad 4.6$$

where E_{av} is the average electric field during the differential admittance recording.

The average electric field was approximated according to the following expression:

$$E_{av} = \frac{U_E - U_{FB}}{d_{ox}} \qquad 4.7$$

where U_E is the applied potential, U_{FB} is the oxide flat band potential and d_{ox} its thickness.

This expression is similar to that employed previously for fitting the admittance curves of pure niobium oxide film [2.4b] but with $\gamma = 5.57 \cdot 10^{-8}$ cm V^{-1} and ε(0) = 49. A quadratic dependence of the dielectric constant on the electric field has been reported more recently [4.3] for anodic niobia film, but in the range of electric field employed in this study the linear dependence was an accurate approximation.

As reported in Fig. 4.17 both the components of the differential admittance were nicely fitted in the range of investigated electrode potential and by taking into account that at higher band bending when the space charge region reaches the oxide/metal interface a constant capacitance value is obtained in agreement with theoretical expectations [2.4c] and with the estimated oxide film thickness (280 Å).

We like to stress that strongly non linear M-S plots (C_{sc}^{-2} vs U_E plot) were obtained in a rather large range of frequencies (200 Hz-20 kHz), if we take into account that at the highest employed frequencies (f > 1 kHz) any residual contribution of the surface states capacitance (C_{SS}) to the measured space charge capacitance (C_{SC}) is surely negligible, we can assume that the reported behaviour is completely justified in the framework of the theory of amorphous semiconductor Schottky barrier.

From the fitting procedure a flat band potential U_{fb} = - 0.80 ± 0.025 V vs Ag/AgCl was estimated for the anodic film on Al-92at.%Nb, which is close to that previously estimated by photoelectrochemical measurements (see section 4.4 and ref. [4.8]) and slightly more cathodic than that estimated for anodic films grown to 9 V on pure Nb (see also below) [2.4a]. Also the oxides with Nb content ≥ 66at.% show the same behaviour with respect to anodic Nb_2O_5, according to previous photoelectrochemical findings on these films (see paragraph 4.4 and ref. [4.8]).

By looking to the electronic density of states distribution derived from the fitting of the admittance components for all investigated frequencies, it is possible to have a better insight on the electronic properties of the mixed oxide.

In Fig. 4.18a we report the average DOS vs distance from metal/oxide interface obtained according to the amorphous Schottky Barrier Theory (see chapter 2 and ref. 2.1, 2.4, 4.2) from the fitting of differential capacitance at 2 kHz, which resulted to be spatially constant (~ 5.0 ± 0.25·10^{19} eV^{-1} cm^{-3}). By looking to the different frequencies an average value of DOS equal to (5.3 ± 1)·10^{19} eV^{-1} cm^{-3} was derived at fixed distance from metal/oxide interface (see fig.4.19a). On the other hand, the DOS distribution along the film thickness can be also obtained by fitting the G_{SC} vs U_E curves. As shown in Fig. 4.18b, the DOS derived by fitting the dependence of G_{SC} on potential at 2 kHz as a function of the parameter x_c (in Chapter 2 defined) displays both a thickness dependence as well larger values with respect to its average value (see Fig. 4.18a) at any x_c. Analogous results were obtained for all the investigated frequencies.

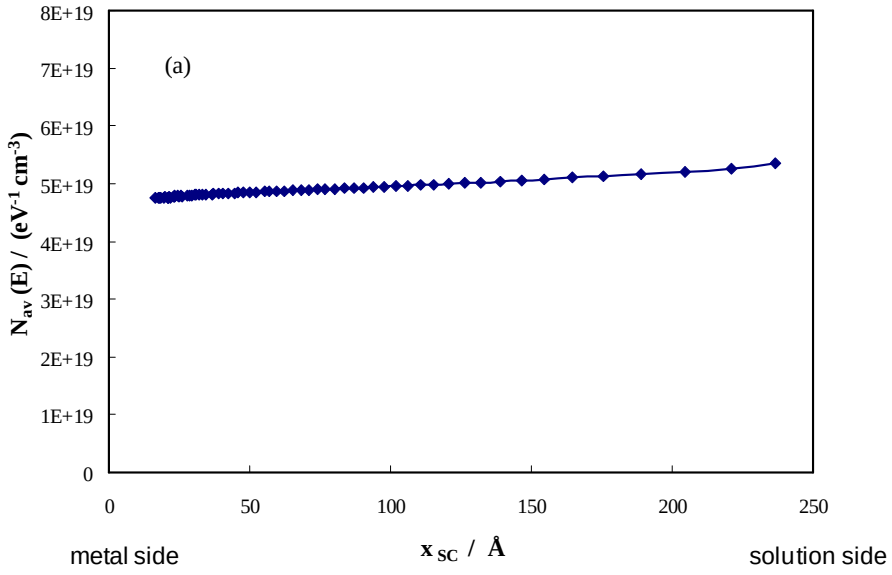

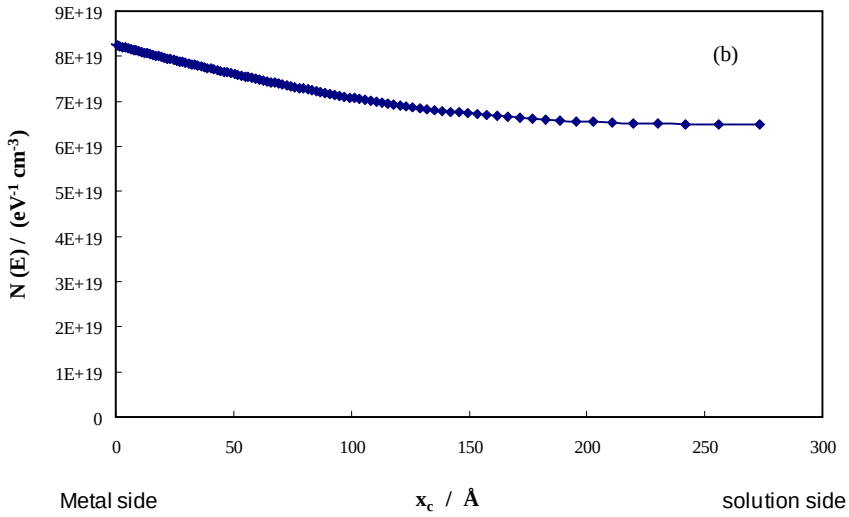

Fig. 4.18 Spatial dependence of DOS derived from the fitting of the differential admittance curves at 2 kHz from a) C_{SC} and b) G_{SC}.

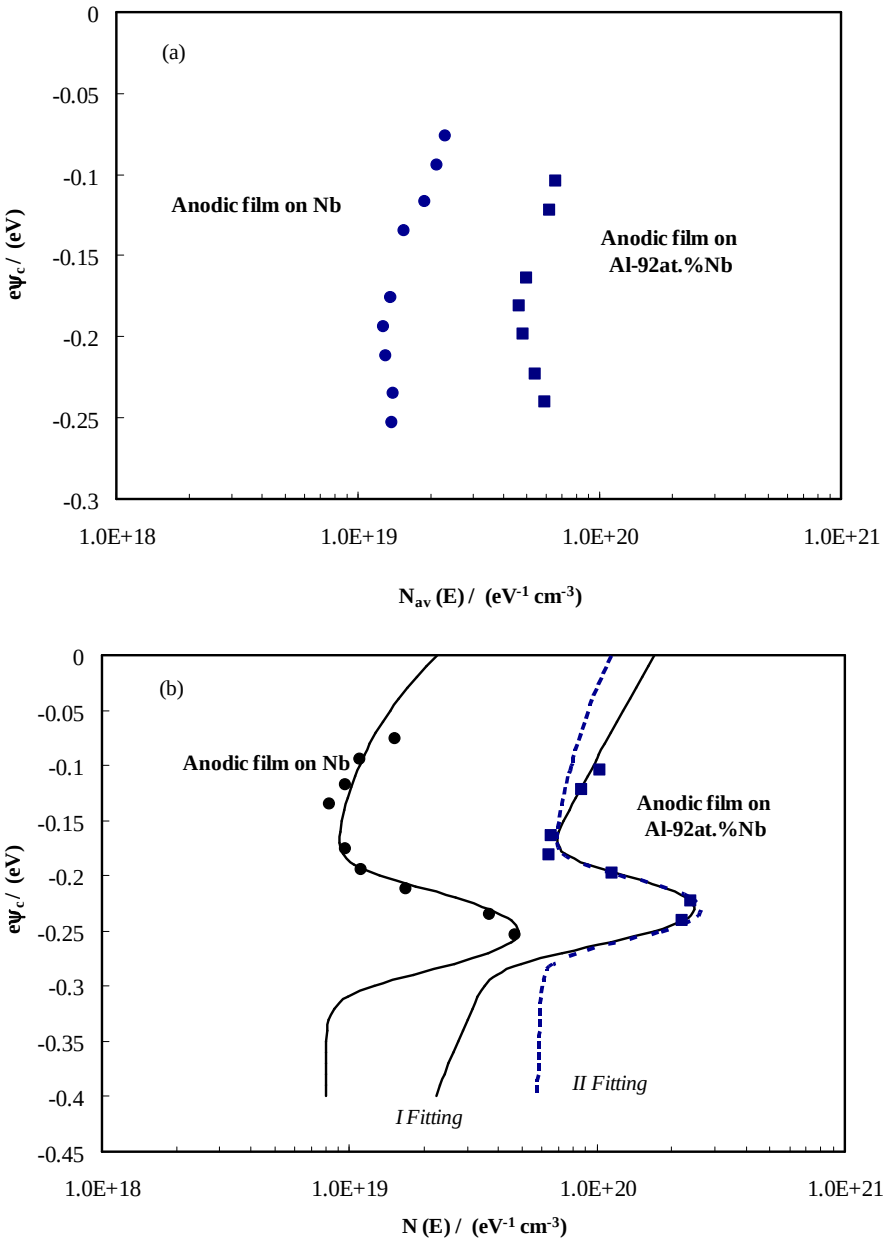

Fig.4.19 DOS distribution vs. distance in energy (or frequency) from E_F ($e\psi_c$ = 0 eV), obtained by fitting admittance curves of anodic film grown on Al-92at.%Nb and Nb. (a) DOS from C_{SC} and (b) DOS from $G_{SC.}$

We like to stress that owing to the finite thickness of the anodic film (i.e. 28 nm), under sufficiently high anodic polarization the space charge region reaches the metal/oxide interface, and a constant capacitance is measured at lower potential with increasing frequency (compare also the M-S plots above reported). The influence of a limited thickness on the experimentally derived DOS distribution along the distance from the metal/oxide interface will be discussed in a forthcoming paper (see also below).

In order to evaluate the dependence of DOS as a function of the energy distance [2.4a] in oxides grown on pure Nb (estimated by same procedure) and on Al-92at.%Nb alloy, in Fig. 4.19a we report the DOS vs $e\psi_c$ derived by fitting the differential capacitance curves, and estimated at a constant distance from the oxide/metal interface (i.e. x_{SC} = 15 nm), at several a.c. frequencies, whilst in Fig. 4.19b we report the analogous DOS derived by fitting the G_{SC} vs U_E curves at constant x_C value (i.e. 15 nm) at different frequencies. From the data of Fig. 4.19 it comes out that by alloying Nb with a small amount (8at.%) of Al metal we get a larger electronic DOS distribution.

The DOS distribution derived from G_{SC} fitting at different frequencies for both pure niobia and mixed oxide on Al-92at.%Nb can be described as sum of three contributions:

$$DOS(E) = \frac{N_T}{\sqrt{2\pi\sigma^2}} \exp\left(-\frac{(E-E_0)^2}{2\sigma^2}\right) + Ae^{\frac{E_C-E}{E_U}} + const. \qquad 4.8$$

The first term is a Gaussian-like function, where N_T is the total density of states in the Gaussian, E_0 is a characteristic energy of the Gaussian distribution and σ a parameter which accounts for the width of the Gaussian distribution; the second term is an exponential function accounting for the tailing of DOS derived from the conduction band electronic states, as previously reported for pure anodic niobia [2.4a].

A reasonable fitting (I Fitting) of total DOS was obtained according to the equations above reported, from which it is possible to extract some interesting information on the electronic properties of the anodic film on pure Nb and on Al-92at.%Nb (see fig. 4.19).

The characteristic parameters (E_0 and σ) of the Gaussian distribution for both films seem quite similar with $E_0 \sim 0.24 \pm 0.01$ eV from the Fermi level, defined trough the relationship: $E_F = -|e|U_{FB}$(ref.), where U_{FB}(ref.) is the flat band potential measured with respect to employed reference electrode (see Chapter 2 and ref. [2.1]) and $\sigma = 0.02 \pm 0.001$ eV for oxide film grown on Al-92at.% Nb alloy slightly smaller than the value of $\sigma = 0.024 \pm 0.001$ eV used for the oxide film grown on pure Nb. The value of $N_T = 1.05 \cdot 10^{19}$ cm^{-3} for mixed Al-Nb oxide film was appreciably larger (~ 4 times) than the value observed on anodic film grown on pure niobium metal (~ $2.4 \cdot 10^{18}$ cm^{-3}).

The exponential tailing of the DOS from the conduction band mobility edge, E_{CBM}, was described by a characteristic tailing parameter in the Urbach region, E_U, equal to 0.0625 eV for niobia and 0.165 eV for the mixed oxide film, its exact value depending on the value chosen for the DOS at the mobility edge E_C assumed in this case in the order of $1 \cdot 10^{21}$ $eV^{-1}cm^{-3}$ (in quite reasonable agreement with effective DOS values reported in literature for d-bands [4.32]).

A constant contribution of DOS (third contribution in eq. 4.8) of $8 \cdot 10^{18}$ $eV^{-1}cm^{-3}$ was added in order to have a reasonable fitting of the experimental points derived for pure niobia as well for mixed oxide.

We tried to change the fitting parameters (II Fitting) in order to push eq. 4.8 to predict a constant DOS at energy distance from the conduction band edge larger than 0.25 eV. In Fig. 4.19b we have overlapped to the experimentally estimated points, the DOS vs energy plot obtained for the film grown on Al-92at.%Nb with a constant DOS parameter of $5.6 \cdot 10^{19}$ cm^{-3} eV^{-1} and with $E_U = 0.105$ eV, whilst an almost unchanged N_T ($0.9 \cdot 10^{19}$ cm^{-3}) was used. It is evident that we succeed in predicting a constant DOS far from E_{CBM} but the quality of fitting in the energy region accessible with the employed a.c. frequencies (f > 2 kHz) is worse.

We like to mention that if the EIS data were fitted by introducing a value of C_a of 90 μF cm^{-2} in series with W element, a similar DOS distribution was derived from C_{SC} as well from G_{SC} vs ψ_c plots. No appreciable differences were evidenced in the fitting parameters used in eq. 4.8.

The results of DOS distribution, moreover, evidence that alloying of Nb with Al, at low concentration, affects the DOS distribution as well the doping level in such a way that the electronic properties of the mixed oxide still reflect the n-type semiconducting behaviour of pure niobium oxide. Thus, the semiconducting to insulator transition observed in anodic films at higher Al content (Al > 34at%) in the sputtered alloy seems to be related to the increase of energetic distance between the Fermi level and the conduction band edge of the oxides due to the monotonic increase of the band gap with increasing Al content (see section 4.4 and ref. [4.8]).

This last suggestion, based also on a detailed photoelectrochemical study of these mixed oxides (see section 4.4 and ref. [4.8]), is supported by the fact that a fixed valence band edge of the mixed oxides has been estimated in presence of a growing optical band gap sustained by the parallel shift of the conduction band edge in the range of Al content variable from 8at.% to 79at.%. The onset of the insulating behaviour in the mixed oxides occurs at 45at.%Al in the alloy when an optical band gap of 3.78 eV has been measured for the anodic film formed on such an alloy.

For semiconducting mixed oxides (i.e. Nb content ≥ 66at.%) a careful inspection of the differential admittance curves as a function of the polarizing voltage and a.c. frequency, allows to estimate a flattening frequency of 2 kHz and 4 kHz for anodic films on Al-66at.%Nb and Al-81at.%Nb, respectively. By imposing $\psi_C = 0$ at the flattening frequency in equation 2.14, it is possible to estimate for both the oxides the energy distance between the conduction band edge and the Fermi level; ΔE_F = 0.47 eV and 0.45 eV for Al-66at.%Nb and Al-81at.%Nb, respectively.

From the differential capacitance curves, we have finally estimated the dependence of the dielectric constant on the film composition (see Fig. 4.20) inserting in eq. 4.5 the oxides' thickness of table 4.1 and the capacitance values of Fig. 4.14 extrapolated to zero-electric field using equation 4.6 as reported in ref. [2.4c]. For semiconducting films (high Nb content) the capacitance values in HBB

regime were employed. We want to stress that the monotonic increase of ε(0) with Nb content in the mixed oxides is rather linear in the whole range of compositions. It has to be taken into consideration that eventually a frequency dispersion of the dielectric constant may exist, however its effect is smaller than the observed variations (see ref. [2.4c]).

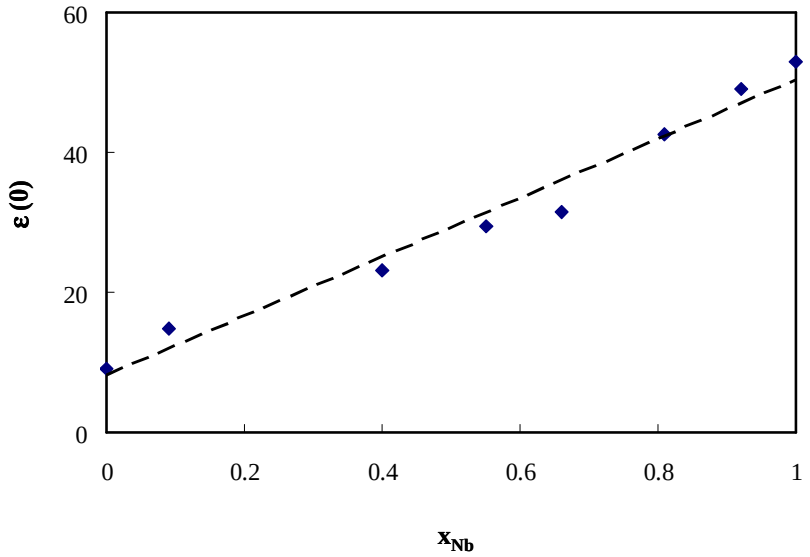

Fig. 4.20 Dielectric constant estimated at zero electric field as a function of the Nb content into the oxide.

In summary, the solid state properties of Al-Nb mixed oxides grown by anodizing on Al-Nb magnetron-sputtering alloys were studied as a function of their composition. The experimental findings arising from impedance measurements evidenced the transition of the oxide from n-semiconductor to insulator with decreasing the Nb content. Moreover, the analysis of the differential admittance curves in the frame of the amorphous semiconductor Schottky barrier allows to get a reliable estimate of the dielectric constant, flat band potential and density of states of the Nb richest investigated oxide.

A rationale for the semiconductor to insulator transition in amorphous mixed oxides has been suggested by taking into account the results of EIS and differential

admittance study as well as the results of a recent photoelectrochemical analysis of their solid state properties. The shift of the conduction band towards higher energy (increasing ΔE_F) potentials, with increase aluminium content, is the main cause of this transition. Concomitantly, the dependence of the dielectric constant on the composition seems to change rather linearly with the composition of the oxides.

This study has evidenced also that the use of simplified Mott-Schottky analysis for the characterisation of thin passive film on metallic alloys is rather misleading if used to derive information on the electronic structure of passive film in terms of donor/acceptor density at a single frequency as evidenced in our previous works (2.1, 2.4, 4.2). Further study is now in progress to extend the use of amorphous semiconductor Schottky barrier theory valid for very thick film to the case of relatively thin amorphous oxides. We like to stress that the results depicted above are encouraging with respect to the use of amorphous semiconductor Schottky barrier theory to extract information which is technologically important from the corrosion as well electronic application point of view.

REFERENCES

[4.1] (a) R. H. French, J. Am. Ceram. Soc., 73, (1990), 477. (b) R. H. French, D. J. Jones, S. Loughlin, J. Am. Ceram. Soc., 77, (1994), 412.

[4.2] F. La Mantia, M. Santamaria, H. Habazaki, F. Di Quarto, J. Electrochem. Soc., 157, (2010), C258.

[4.3] Q. Van Overmeere, F. Blaffart, F. La Mantia, F. Di Quarto, J. Proost, J. App. Phys, 111, (2012), 113529.

[4.4] Z-S. Feng, J-J. Chen, R. Zhang, N. Zhao, Ceramics International, 38, (2012), 3057.

[4.5] J-H. Jang, T-Y. Kim, N-J. Kim, C-H. Lee, E-M. Park, C. Park, S-J. Suh, Mat. Sci. Eng. B, 176, (2011), 1505.

[4.6] S-S. Park, B-T. Lee, J. Electroceramics, 13, (2004), 111.

[4.7] A.I. de Sa´, C.M. Rangel, Q. Lu, P. Skeldon, G.E. Thompson, Corr. Sci., 48, (2006), 2203.

[4.8] M. Santamaria, F. Di Franco, F. Di Quarto, P. Skeldon and G.E. Thompson, Journal of Physical Chemistry C, 117, (2013), 4201.

[4.9] F. Di Franco, M. Santamaria, F. Di Quarto, F. La Mantia, A. I. De Sà, C. M. Rangel, ECS Journal of Solid State Science and Technology, 2, (11), (2013), N205.

[4.10] Santamaria, M.; Di Quarto, F.; Habazaki, H. Electrochimica Acta, 53, (2008), 2272.

[4.11] Gerischer H. Corr. Sci., 31, (1990), 81.

[4.12](a) Xu, Y.-N.; Ching, W.Y. Phys. Rev. B, , 43, (1991), 4461. (b) Jiang, T.T.; Sun, Q.Q.; Li, Y.; Guo, J.J.; Zhou, P.; Ding, S.-J.; Zhang, D. W.; J. of Phys. D: Appl. Phys., , 44, (2011), 185402.

[4.13] Pringle, J.P.S. Electrochim. Acta, 25, (1980), 1423.

[4.14] Di Quarto, F.; Di Franco, F.; Santamaria, M. in Frontiers in Electronic Materials Heber J.; Schlom, D.; Tokura, Y.; Waser, R.; Wuttig M. (Eds). A collection of extended abstracts of the Nature Conference Frontiers in Electronic Materials, June 17th to 20th 2012, Aachen, Germany, 648-650, 2012.

[4.15] (a) Di Quarto, F.; Gentile, C.; Piazza, S.; Sunseri, C. J. Electrochem. Soc., 138, (1991), 1856. (b) Nguyen, N.V.; Kirillov, O.A.; Jiang, W.; Wang, W.; Suehle, J.S.; Ye, P.D.; Xuan, Y.; Goel, N.; Choi, K.-W.; Tsai, W.; Sayan, S. Appl. Phys. Letter, 93, (2008), 082105-1. (c) Afanas'ev, V.V.; Houssa, M.; Stesmans, A. J. Appl. Phys., , 91, (2002), 3079. (d) Yeo, Y.-C.; King, T.-J., Hu, C. J. Appl. Phys., 92, (2002), 7266.

[4.16] Bernard, J. E.; Zunger, A. Phys. Rev. B, , 36, (1987), 3199.

[4.17] Memming, R. Semiconductor Electrochemistry, J. Wiley-VCH, Weinheim FRG 2001.

[4.19] McCafferty E. Electrochimica Acta, , 55, (2010), 1630.

[4.20] Robertson, J. Rep. Prog. Phys., , 69, (2006), 327.

[4.21] Koffyberg, F. P.; Benko, F. A. J. Electrochem. Soc., , 128, (1981), 2476.

[4.22] Weinhardt, L.; Blum, M.; Bär, M.; Heske, C.; Cole, B.; Marsen, B.; Miller, E.L. J. Phys. Chem. C, , 112, (2008), 3078.

[4.23] Miyazaki, S. J. Vac. Sci. Technol. B, , 19, (2001), 2212.

[4.24] Dantas, J.M.; Lima, A.F.; Lalic, M.V. J. of Phys. Conference Series, , 249, (2010), 012036-1.

[4.25] Afanas'ev, V.V.; Stesmans, A. J. Appl. Phys., , 102, (2007), 081301-1.

[4.26] Wei, S.-H.; Zunger, A. Phys. Rev. Lett., , 76, (1996), 664.

[4.27] M. Abe, H. Morisaki, K. Yazawa, Jpn. J. Appl. Phys., 19, (1980), 1421.

[4.28] Comprehensive Chemical Kinetics, Edited by R.G. Compton Vol. 27 "Electrode kinetics: reactions". Elsevier Amsterdam (1988) Andrew Hamnett, Chapter 2 p. 117.

[4.29] L. Bousse, P. Bergveld, J: Electroanal. Chem., 152, (1983), 25.

[4.30] G. Oskam, D. Vanmaekelbergh, J.J. Kelly, El. Acta, 38, (1993), 301.

[4.31] F. La Mantia, J. Vetter, P. Novak, El. Acta, 53, (2008), 4109.

[4.32] R.H. Bube, Electrons in Solids, Academic Press, San Diego, 1988.

5 Growth and Characterization of anodic films on magnetron sputtered Ti-Si Alloys.

5.1 Introduction

The occurrence of crystallization phenomena during the anodizing of valve metals and/or when high electric fields are applied across already formed anodic films is an important issue for their use as dielectric in the electronic industry. A dense and flaw-free barrier oxide must be formed to work as a dielectric in capacitor or in memristor [5.1, 5.2].

Anodic titanium oxide has attracted much attention in micro- and nano-electronics due the high dielectric constant of TiO_2 (ranging between 24 and 53, ref. [5.3-5.6]). However, anodic TiO_2 films develop with a high population density of flaws on high purity titanium in aqueous electrolytes. Thus, anodic titanium oxide-based capacitors have not been realized practically despite the large permittivity of the oxide with respect to anodic aluminium oxide (ε_{ox} = 10) and tantalum oxide (ε_{ox} = 27), currently used in commercial electrolytic capacitors.

Previous works [5.7] have shown that the development of flaws in anodic TiO_2 is associated with crystallization of the film during anodizing. The crystalline regions are reported to enable oxygen evolution, due to their increased electronic conductivity with respect to the amorphous counterpart. The consequent increased pressure can bring to film breakdown, which is detrimental for capacitors.

Several strategies have been proposed in the literature to hinder or delay the onset of crystallization during anodizing of TiO_2. It is widely accepted that the onset of crystallization is delayed by the incorporation of foreign species inside the oxide [5.7-5.9]. These species can come from the electrolyte and, according to their relative migration rate compared to that of the ions involved in the oxide formation (i.e. Ti^{4+} and O^{2-}), they contribute to keep amorphous the outer part of the anodic film.

But foreign species can be incorporated into the anodic films by alloying to titanium small amount of another element, namely silicon. The occurrence of amorphous to crystalline transition during the anodizing of Ti and Ti-Si alloys has

been extensively studied in refs. [5.8, 5.9] by ex situ optical techniques, like Transmission Electron Microscopy of ultramicrotomed sections, which allowed to well characterize the structural features of the anodic films as a function of the anodizing conditions (alloy composition and ageing, anodizing electrolyte). Moreover, this transition has been related to the film composition by both ex situ Rutherford Back Scattering (RBS) and Glow Discharge Optical Emission Spectroscopy (GDOES), which allowed to evidence the presence of Si in the inner part of the anodic films corresponding to the 40% of the whole film thickness. These experimental findings unambiguously demonstrate that Si has an effective role in delaying the crystallization and breakdown of TiO_2. It remains to explain the effect of Si on the solid state properties of anodic films on Ti-Si alloys. Thus, this chapter is focused on the physico-chemical characterization of anodic films on sputtering-deposited Ti-6at.%Si alloys as a function of their thickness (i.e. formation voltage). Photocurrent Spectroscopy allowed to estimate the band gap, flat band potential and conductivity type of the investigated films, while their dielectric constant was estimated by differential capacitance measurements. The dependence of the photocurrent on the electric field and on the photon energy is studied taking into account the amorphous structure of the investigated films, and modelled on the basis of the Braun-Onsager theory.

Part of this work was realized in collaboration with research group of Prof. H. Habazaki (Hokkaido University, Japan). The results of this chapter are reported in refs. [5.10].

5.2 Experimental

Ti–6%Si alloy was prepared by co-sputtering of 99.5% titanium and 99.999% silicon using a dc magnetron sputtering method. The alloy was deposited, as a layer about 200 nm thick, on glass substrates [5.8-5.9]. The deposited layers were anodized to several final voltages (from 5 V to 40 V) at 5 mA cm^{-2} in phosphoric acid at room temperature.

The experimental set-up for the photo-electrochemical measurements has been described elsewhere [2.1]. The photoelectrochemical experiments were carried out in 1 M H_3PO_4 and 0.1 M $(NH_4)_2B_4O_7$ (ABE) aqueous solutions.

A silver silver-chloride electrode (0 V vs Ag/AgCl = 0.197 V vs SHE) was employed as reference electrode for all the electrochemical and photoelectrochemical experiments.

Differential capacitance curves were recorded in 1 M H_3PO_4 solution with $v_{a.c.}$ = 10 mV by using a Parstat 2263 (PAR)

5.3 Photoelectrochemical results

Photocurrent spectra were recorded for anodic films grown on Ti-6at.%Si as a function of the formation voltage (i.e. thickness). In Fig. 5.1 we report the photocurrent yield, I_{ph} (photocurrent corrected for the efficiency of the lamp–monochromator system, see ref. [2.1]) as a function of the irradiating wavelength relating to a 5 V anodic film, recorded by polarizing the electrode at 3 V (Ag/AgCl).

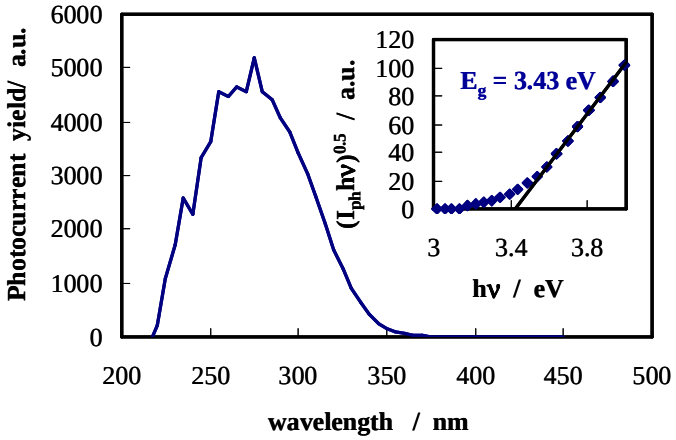

Fig. 5.1 Photocurrent spectrum relating to anodic films grown to U_F = 5V in 1 M H_3PO_4 at 5 mA cm^{-2} on Ti-6at.%Si alloy, recorded by polarizing the electrodes at 3 V vs. Ag/AgCl in 0.1 M ABE. Inset: Band gap estimate by assuming non direct optical transitions.

As shown in the inset, an optical band gap of 3.43 eV can be estimated for this oxide by extrapolating to zero the $(I_{ph}h\nu)^{0.5}$ vs hν plot, according to eqs. 2.31 and 2.38. Not appreciable differences were evidenced in the photocurrent spectra relating to thicker films for formation voltages ≤ 40 V (see Fig. 5.2).

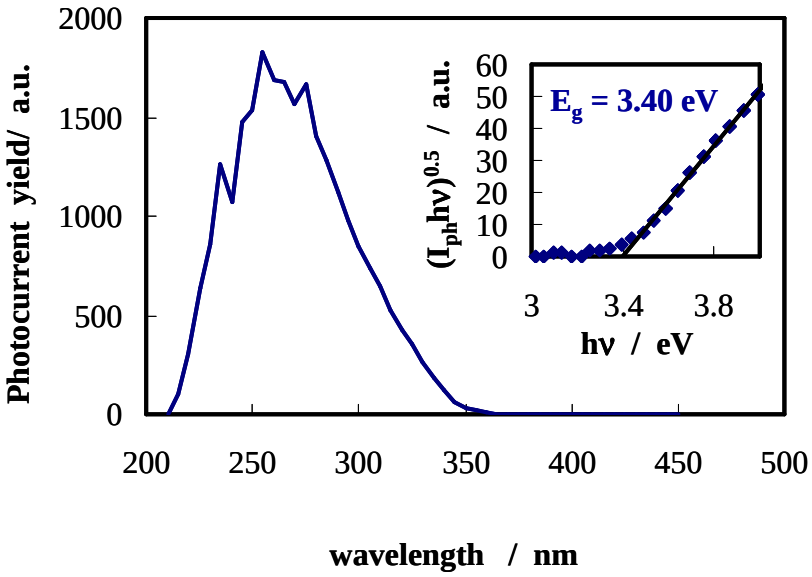

Fig. 5.2 Photocurrent spectrum relating to anodic film grown to U_F = 40V in 1 M H_3PO_4 at 5 mA cm^{-2} on Ti-6at.%Si alloy, recorded by polarizing the electrodes at 5 V vs. Ag/AgCl in 0.1 M ABE. Inset: Band gap estimate by assuming non direct optical transitions

If we anodize silicon free titanium in the same conditions (5 mA cm^{-2} in H_3PO_4) the optical band gap is ~ 3.40 eV for formation voltage ≤ 10 V (see Fig. 5.3a), while E_g = 3.30 eV can be estimated for 20 V and 40 V anodic film (see Fig. 5.3b). An appreciable tailing in the photocurrent spectra can be observed due to optical

transitions at energy lower than the band gap of the oxide, which interests a wider wavelengths range for thick films (see Fig. 5.3b).

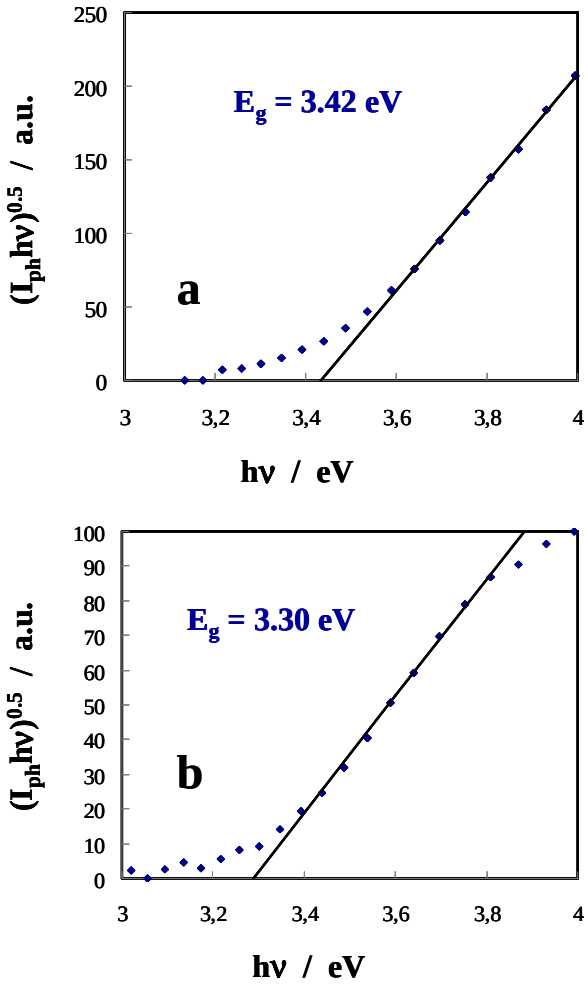

Fig. 5.3 Band gap estimate by assuming non-direct optical transitions for anodic films grown on Ti in 1 M H_3PO_4 at 5 mA cm^{-2}. a) U_F = 5 V and U_E = 3 V vs. Ag/AgCl in 0.1 M ABE and b) U_F = 40 V and U_E = 5 V in 0.1 M ABE.

It is interesting to stress that the measured band gap values for anodic films grown on both Ti and Ti-6at.%Si are higher than those reported for crystalline TiO_2 (i.e. 3.2 eV for anatase and 3.05 eV for rutile, see ref. [5.5]). As discussed in previous works [5.5, 2.1], this difference can attributed to the amorphous nature of the layers and, of relevance, it keeps constant as a function of the film thickness for Si containing films, while decreases for those grown on Ti.

In Fig. 5.4a and 5.4b we report the photocurrent vs potential curves (photocharacteristics), relating to the 5 V anodic films on Ti-6at.%Si and Ti, recorded at several constant irradiating wavelengths. In both cases the photocurrent decreases by decreasing the polarizing voltage, as expected for n-type SC materials, and goes to zero at ~ - 0.6 V (SSC). The zero photocurrent potential can be assumed as a proxy of the flat band potential [2.1].

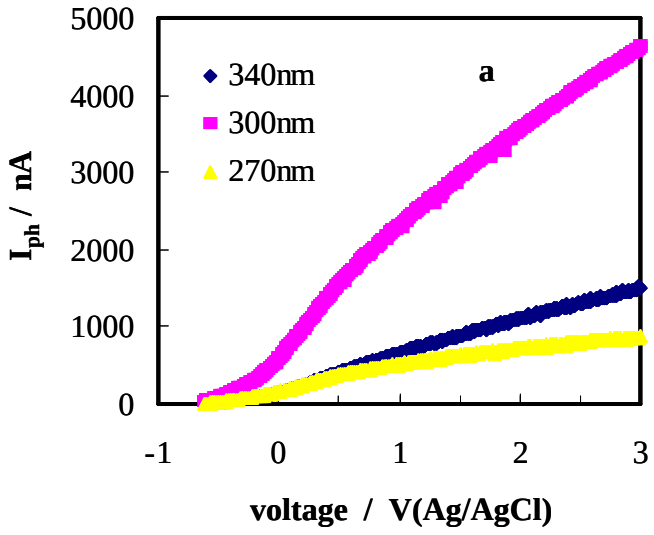

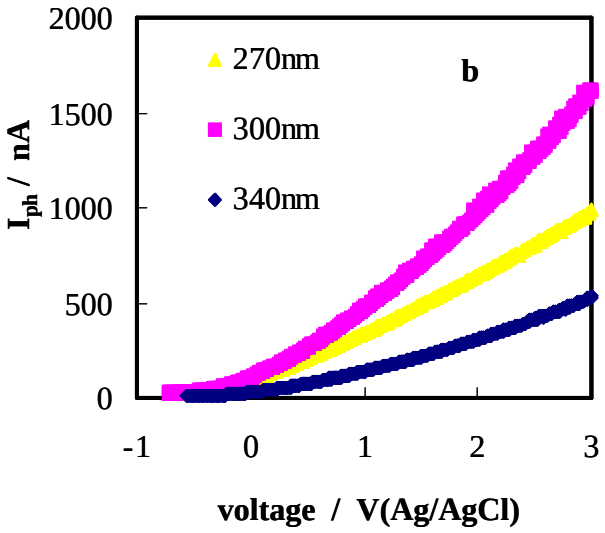

Fig. 5.4 Photocurrent vs potential curves relating to anodic films grown to 5 V in 1 M H_3PO_4 at 5 mA cm^{-2} on a) Ti and b) Ti-6at.%Si alloy Sol: 0.1 M ABE and scan rate of 10 mV s^{-1}.

Moreover, in both cases the transport equations usually employed to describe the behaviour of crystalline SC, based on the Gärtner-Butler model, seem to be not adequate, as evidenced, many years ago, in a previous paper on the photoelectrochemical behaviour of amorphous anodic film on W [5.11]. This model predicts the absence of any influence of the photon energy on the shape of the photocharacteristics, as well as a linear dependence of I_{ph}^2 on electrode potential, provided that surface and space charge recombination phenomena are negligible, as usually occurs at high band bending as long as the space charge region width (or film thickness for insulating materials) is much smaller than the light absorption length, α^{-1}. For amorphous materials we have to take into account the possible presence of initial recombination effects of injected photocarriers. According to models usually employed to describe the band structure of amorphous SC [2.1, 2.2, 2.36], localized states are present below the conduction band edge and above the

valence band edge, where the photocarriers show poor mobility so favouring the occurrence of initial recombination effects as well as a decrease of drift mobility and lifetime of photocarriers. Thus, for amorphous materials the photocharacteristics can be fitted according to power laws:

$$I_{ph}^{n} \propto (U_E - U_{FB}) \qquad (5.1)$$

where n is expected to decrease by decreasing photon energy. Lower initial recombination kinetic is expected, regardless of the microscopic mechanism of recombination, with increasing excess energy of injected photocarriers. As summarized in table 5.1, in spite of the almost coincident band gap value, the dependence of the I_{ph} on U_E is sensitively different for the Si containing and Si free oxides. A sublinear ($n > 1$) behaviour is shown by the anodic film on Ti, while a supralinear behaviour ($n < 1$) is evidenced for the anodic film on the alloy. In this last case an almost constant n value was derived from the best fitting of the photocharacteristics at different wavelength ($340 \leq \lambda \leq 270$ nm).

λ / nm	$n_{Ti\text{-}6at.\%Si}$	n_{Ti}
270	0.7	2.1
300	0.7	1.5
340	0.7	1.3

Table 5.1. Comparison between the exponent n estimated from the best fitting according to eq. 5.1 of the photocharacteristics relating to 5 V anodic films grown at 5 mA cm^{-2} on Ti and Ti-6at.%Si alloy.

By increasing the formation voltage to 10 V, not appreciable differences are revealed for Si containing film, while for thicker anodic oxides ($U_F \geq 20$ V) an inversion of the photocurrent sign is revealed by moving the polarizing voltage toward the cathodic direction (see Fig. 5.5a).

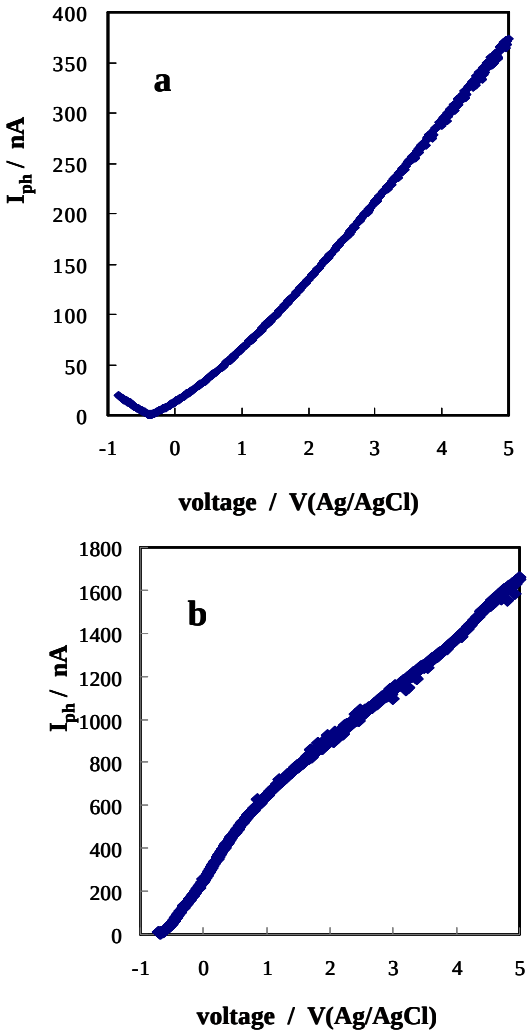

Fig. 5.5 Photocurrent vs potential curves relating to anodic films grown to 40 V in 1 M H_3PO_4 at 5 mA cm^{-2} on a) Ti-6at.%Si alloy and b) Ti. Sol: 0.1 M ABE, λ = 300 nm and scan rate 10 mV s^{-1}.

This is typical on insulating material, for which both anodic and cathodic photocurrent can be measured depending on the direction of the electric field, i.e. on the applied potential with respect to the flat band potential. Thus, for insulating layers the inversion photocurrent potential can be assumed as a proxy of the flat band potential, which results to be 0.15 V more anodic than that estimated for 5 V anodic films (compare Fig. 5.4b and 5.5a). It is interesting to mention that there is no evidence of the inversion of photocurrent sign for pure TiO_2 (Fig. 5.5b).

An analogous photoelectrochemical investigation was performed in 1 M H_3PO_4 solution, which allowed to further confirm the experimental E_g values estimated in 0.1 M ABE and the transition from n-type to insulating films with increasing formation voltage. The zero photocurrent potential for the semiconducting films and inversion photocurrent potential for the insulating films were found to be more anodic than those estimated in 0.1 M ABE, in agreement with the dependence of U_{FB} on pH reported in [3.16].

5.4 Differential capacitance results

In Fig. 5.6a we report the differential capacitance curves relating to anodic films grown to 5 V on Ti-6at.%Si, recorded in 1 M H_3PO_4 at different a.c. signal frequencies, f. The differential capacitance appears to be dependent on both potential and a.c. frequency: as expected for n-type amorphous semiconducting material showing both an increase in the C value, when the electrode potential decreases toward U_{FB}, and a frequency dependent value in the region of electrode potential where the space-charge region is smaller than the total film thickness [2.4b].

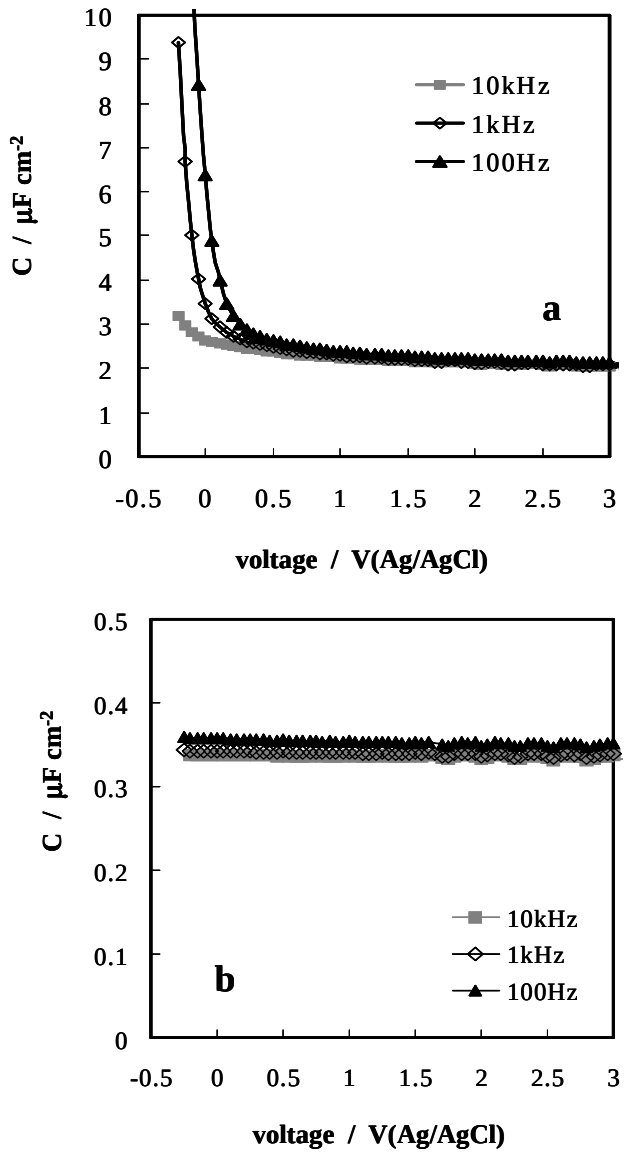

Fig. 5.6 Differential capacitance curves relating to anodic film grown on Ti-5at.%Si at 5 mA cm^{-2} in 1 M H_3PO_4. f = 1 kHz and sol: 1 M H_3PO_4. Formation voltage: a) 5 V and b) 40 V.

By increasing the formation voltage to 20 V, the measured capacitance changes slightly with the applied potential, and becomes almost potential independent for $U_F \geq 40$ V anodic oxides (see Fig. 5.6b). This behaviour can be ascribed to the insulating character of thicker films in agreement with the photoelectrochemical results, evidencing a change from n-type SC to insulator by increasing the film thickness. The dependence of the measured capacitance on frequency can be explained by the presence of localized states inside the mobility gap of the films, in agreement with their amorphous nature, as well as by the presence of electronic surface states.

According to the theory of amorphous semiconductor Schottky barrier (see chapter 2 and ref. [2.1, 2.4]), under high band bending ($e\psi_S > E_g/2 - \Delta E_F$) and high frequency ($\psi_C \rightarrow 0$), $C(\psi_S, \omega) \cong C(\psi_C, 0)$ we can assume that the space charge region width coincides with the whole oxide thickness. This allows to estimate the oxides' dielectric constant according to $C = \frac{\varepsilon\varepsilon_0}{d}$.

The film thickness during the anodizing of valve metals and valve metals alloys is directly proportional to the formation voltage, U_F, according to the following eq.

$$d = \tilde{A}(U_F - U_{eq}) \qquad 5.2$$

where $\tilde{A}$ is the anodizing ratio, i.e. the reciprocal of the electric field strength E_d, E_{eq} is the equilibrium potential corresponding to the oxide formation. Thus, a linear dependence of the reciprocal of the capacitance, C^{-1}, vs formation potential is expected with a slope:

$$\frac{dC^{-1}}{dU_F} = \frac{1}{\varepsilon\varepsilon_0 E_d} \qquad 5.3$$

In Fig. 5.7 we report the reciprocal of the capacitance as a function of the formation voltage i.e. film thickness. C^{-1} results to depend linearly on U_F with a slope of 0.073 $cm^2\ \mu F^{-1} V^{-1}$.

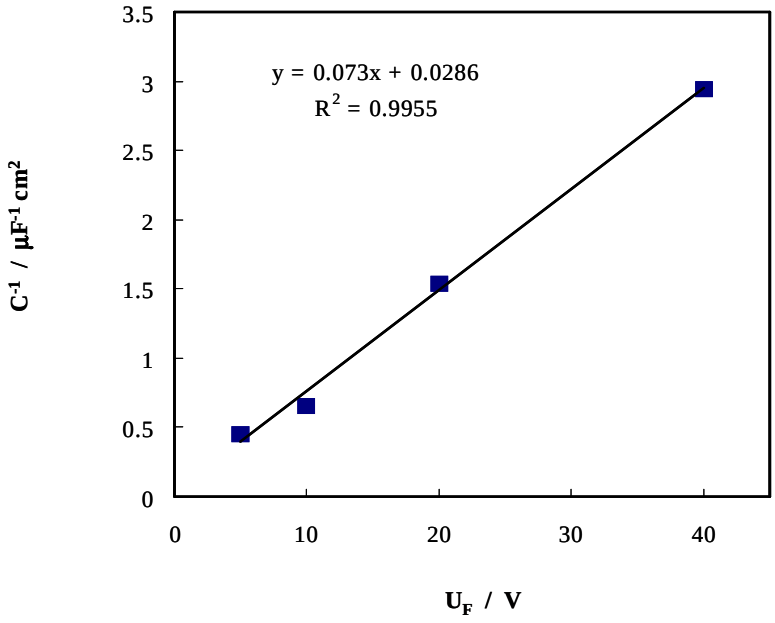

Fig. 5.7 Reciprocal of measured capacitance as a function of the formation voltage.

According to transmission electron micrographs of ultramicrotomed sections relating to anodic films grown on sputter deposited Ti-6at.%Si in 1 M H_3PO_4 at 5 mA cm^{-2}, an anodizing ratio of ~ 20 Å V^{-1} can be estimated, which allows to estimate for the films a dielectric constant of ~ 31. This value is quite far with respect to the dielectric constant previously estimated for anodic films on Ti [~ 50 according to refs. 5.3, 5.5], but almost coincident with that reported in ref. [5.9], estimated from the fitting of the electrochemical impedance spectra relating to 50 V anodic layers on sputtering-deposited Ti-6at.%Si. According to the GDOES compositional depth profiles the anodic films on Ti-Si alloys can be modelled as the series between a pure amorphous TiO_2 layer, corresponding to the 60 % of the whole thickness, and a Si containing TiO_2 layer for the remaining 40% enriched in Si with respect to the base alloy (i.e. 10at.%Si). However, the sensitive drop of the dielectric constant cannot be only explained by the presence of Si in the anodic film. If we assume that the dielectric constant of the inner layer can be estimated by averaging

for the cation fractions ε of SiO_2 (i.e. ~ 4) and ε of TiO_2, assumed unknown, we can estimate for the latter a value of ~ 32, thus in any case far from the value previously suggested for anodic TiO_2 grown on pure titanium.

5.5 – Discussion

In ref. [5.6] it was shown for anodic films grown on Ti in 0.5 M H_2SO_4 that the dependence of photocurrent on both the applied potential and irradiating wavelength could be explained in the frame of the Onsager's theory of geminate recombination, which calculates the probability of opposite ion recombination in presence of electric field developed for electrolytic solutions [5.12], by using the approach of Pai-Enck [5.13] to the initial recombination process of electron-hole pairs in amorphous material. As evidenced by these authors for amorphous selenium film, rather large separation distances as a function of photon energy were found to fit the experimental data with a poor accordance between theoretical and experimental estimates of thermalization distance. An improvement of this approach was achieved in 1993 [5.6], when the photocharacteristics relating to anodic film grown on Ti in H_2SO_4 solution were fitted in a rather large range of photon energy and electric field using as fitting parameters reasonable thermalization distances and a dielectric constant averaged between the high frequency (optical frequencies) and static values. However, the fitting of experimental data in the low band bending region was poor, even taking into account the shift in the U_{FB} under illumination.

In the case of the anodic films on Ti-6at.%Si the best fitting procedure of the photocharacteristics according to eq. 5.1 evidences a very scarce dependence of the exponent n on the photon energy in a rather large range of wavelengths (from 340 nm to 270 nm, see table 5.1) in spite of the expected appreciably different thermalization distances. This experimental finding is a further evidence that Pai-Enck approach to the thermalization process of geminate photocarriers is probably not able to fully account for the initial recombination processes of injected photocarriers in amorphous solids.

In order to overcome the above mentioned limitations and keeping in the equation of transport of photocarriers the field and photon energy dependence

necessary to account for the experimental behaviour of photocharacteristics, we employed a model proposed by Braun for the dissociation of excited photocarriers or charge transfer exciton (CTE) widely used with organic photoconductors.

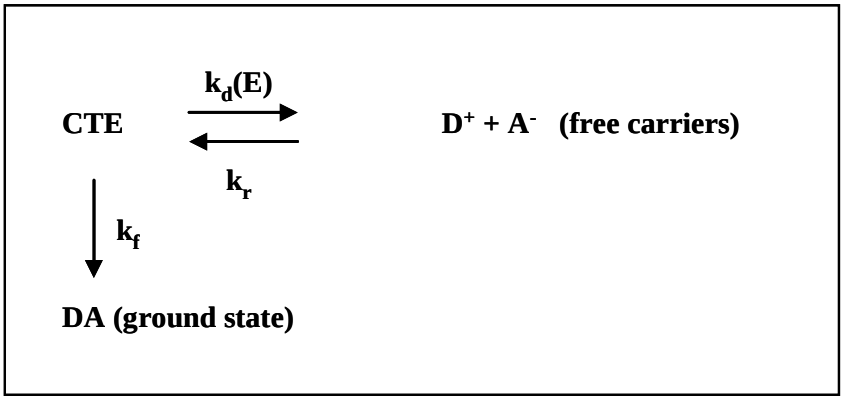

Fig. 5.8 Schematic representation of the kinetics for the dissociation of excited photocarriers or charge transfer exciton (CTE).

In 1984 [5.14] C.L. Braun posed the problem of the extension of the Onsager's theory to the photogeneration in solids containing electron donors and acceptors. According to Onsager [5.12], given the initial separation and orientation of a pair of ions, the probability that the pair will separate to infinity can be obtained solving a diffusion equation for the relative motion of two opposite charges in the net potential provided by their Coulombic attraction. Onsager's model assumes that if the distance between the charges is zero, the pair irrevocably disappears (geminate recombination). Braun poses the problem that this boundary condition cannot be straightforward used when free charge production involves bound exciton. He addressed the question of how a charge pair could evolve from an initial nearest-neighbour separation to the much larger thermalized-pair separation, suggesting the scheme of Fig. 5.8 to describe the kinetics of charge transfer dissociation. CTE can disappear either by dissociation into free carriers with an electric field dependent

rate constant, $k_d(E)$, or decaying to the ground state with rate constant k_f. One may imagine that during the lifetime of CTE, τ:

$$\tau(E) = [k_f + k_d(E)]^{-1} \qquad 5.4$$

many partial dissociations take place. In eq. 5.4 k_f is a decay rate constant of CTE to the ground state whilst $k_d(E)$ is the electric field dependent rate constant which accounts for the kinetics of separation of CTE into free carriers. The subsequent recombinations generate CTE, which might then later dissociate completely. This is in contrast to what expected on the basis of the conventional Onsager's theory [5.12] in which a recombining pair disappears from the system. According to the above reported schematic representation, the probability P(E) that CTE dissociates giving free carriers is:

$$P(E) = \frac{k_d(E)}{k_f + k_d(E)} = k_d(E)\tau(E) = \frac{1}{\frac{k_f}{k_d(E)} + 1} \qquad 5.5$$

The initial bound electron-hole pair can be viewed as a bound exciton with eq. 5.5 representing the field dependent separation probability in presence of an electric field and at fixed temperature. In the Braun's model the dissociation constant $k_d(E)$ is written by using the Onsager's theory of weak electrolyte dissociation which according to ref. [5.14] can be written as:

$$k_d(E) = k_d(0) J_1\frac{\left\lfloor 2\sqrt{2}(-b)^{0.5}\right\rfloor}{\sqrt{2}(-b)^{0.5}} \qquad 5.6$$

where J_1 is the Bessel function of order 1:

$$J_1\frac{\left\lfloor 2\sqrt{2}(-b)^{0.5}\right\rfloor}{\sqrt{2}(-b)^{0.5}} = 1 + b + \frac{b^2}{3} + \frac{b^3}{18} + \frac{b^4}{180}... \qquad 5.7$$

with $b = \frac{e^3 E}{8\pi\langle\varepsilon\rangle\varepsilon_0 k^2 T^2}$, whilst $k_d(0)$ can be considered as the zero field ionization rate for the generation of free carriers in absence of electric field. By following ref. [5.15] $k_d(0)$ can be written as:

$$k_d(0) = \omega_0 \exp\left(-\frac{E_b}{kT}\right) \qquad 5.8$$

where ω_0 is an "attempt to escape pre-factor" and E_b is "the binding energy of the CTE state with respect to well-separated polaron pair". According to the previous expressions we get:

$$k_d(E) = \omega_0 \exp\left(-\frac{E_b}{kT}\right) J_1\frac{\left[2\sqrt{2}(-b)^{0.5}\right]}{\sqrt{2}(-b)^{0.5}} \qquad 5.9$$

so that the field dependent CTE dissociation probability P(E) can be written as:

$$P(E) = \frac{1}{1 + \frac{k_f / k_d(0)}{J_1\frac{\left[2\sqrt{2}(-b)^{0.5}\right]}{\sqrt{2}(-b)^{0.5}}}} \qquad 5.10$$

which is a function of the electric field, trough the b term, as well as of the ratio between the recombination rate constant and zero electric field CTE dissociation constant. The electric field expression entering in the Bessel function was derived from the theory of amorphous semiconductor in the low and high band bending approximation [see chapter 2 and ref. 5.6, 2.4] by using the appropriate value of density of states in the case of semiconducting films, while for thick insulating film it was estimated as $\frac{(U_E - U_{FB})}{d_{ox}}$. The ratio $k_f / k_d(0)$ was left as adjustable parameter, together with the drift range $\mu\tau$.

In order to explain the dependence of the measured photocurrent on the applied potential, we used the following equation, according to equation 2.39:

$$I_{ph} = P(E)e\Phi_0(1-R)\left[1-\exp\left(-x_{SC}\frac{1+\alpha L_D}{L_D}\right)\right]\frac{\alpha L_D}{1+\alpha L_D} \qquad 5.11$$

where P(E) can be now written according to eq. 5.10, Φ_0 is the photon flux impinging the electrode surface, R is the reflection coefficient, α is the light absorption coefficient, L_D is the sum of drift lengths of injected (electron and hole) photocarriers , $L_D = (\mu_h\tau_h + \mu_n\tau_n)\cdot E_{el,av}$, with $E_{el,av}$ defined as the average electric field in the semiconductor according to the usual expression $E_{el,av} = \Delta\Phi_{SC}/x_{SC}$ with $\Delta\Phi_{SC} = (U_E - U_{FB})$ representing the band bending at the potential U_E and x_{SC} the space charge region width. The space charge region width, x_{SC} , in amorphous SC is expressed according to [2.1, 2.4] with $x_{SC} = x_{SC}^0 \ln\left(\frac{\Delta\Phi_{SC}}{k_BT/e}\right)$ in low band bending regime and $x_{SC} = x_{SC}^0 \ln\left(\frac{e\psi_g}{k_BT} - 1 + \sqrt{1+\frac{2}{\psi_g}\left(\Delta\Phi_{SC}-\psi_g\right)}\right)$ in high band bending regime with $x_{SC}^0 = \sqrt{\frac{\varepsilon\varepsilon_0}{e^2N(E_F)}}$ space charge region width at 1 volt of band bending. In the case of insulating film or when the space charge region reached the film thickness the usual expressions valid for insulating material were used, where necessary, by substitution of the space charge term with the oxide film thickness.

The reflection coefficient has been calculated by using a three layers model (i.e. solution/oxide/metal) under normal incidence and by including the effects of multiple reflections [5.16] with the optical constants for solution, oxide and metallic substrate taken from the literature [5.17, 5.18]. In order to reduce the number of adjustable parameters in the fitting procedure, the values of light absorption

coefficient, α, at different wavelengths (280 nm $\leq \lambda \leq$ 340 nm) were calculated with equation, according to equation 2.31 (see chapter 2 and ref. [2.1]):

$$\alpha h\nu = B(h\nu - E_g)^2 \qquad 5.12$$

with $B = 5.30 \cdot 10^5$ cm^{-1} eV^{-1} and $E_g = 3.40$ eV. B was chosen so that a value of α coincident with that reported for TiO_2 film in [5.19] at λ = 358 nm was obtained. Moreover this value is in the range of values usually reported for other amorphous semiconductors [2.1].

Owing to the mathematical entanglement between the light absorption coefficient and the drift length in the general expression of photocurrent, the value of $\mu\tau$ was not independently derived from the fitting procedure unless to have a contemporary measure of the extinction coefficient of the films in the optical region, where the photon energy was higher than E_g. However, from the fitting procedure for λ < 280 nm, α slightly lower than that derived from the above reported relationship was employed in order to keep the drift range of photocarriers constant. This choice is in agreement with usually observed trend in the light absorption coefficient of crystalline and amorphous materials, showing a tendency toward a saturation value at photon energies significantly higher than the optical band gap [2.1]. This general assumption is also supported from the experimental data on TiO_2 amorphous film reported in ref. [5.17]. In order to clarify such an aspect we like to mention that in our case for λ = 270 nm a decrease of ~ 20% in α with respect to the value derived from the above relationship was enough to keep the same $\mu\tau$ in the fitting procedure. In the case of thin films the percentage change in α was reflected in the value of $\mu\tau$, so that the values of drift for $\lambda \leq$ 270 nm contain an uncertainty of ~ 20%.

Eq. 5.11 has been used to fit the I_{ph} vs U_E curves for thin (5 V) semiconducting and thick (20 V and 40 V) insulating anodic oxide films grown on Ti-6at.%Si, after substitution of different expressions for all physical parameters embodied in the different term of eq. 5.11.

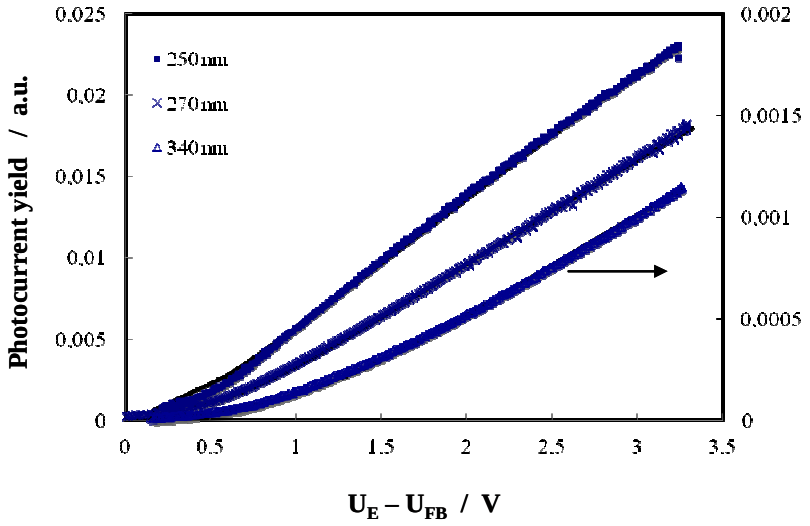

Fig. 5.9 Photocurrent vs band bending relating to anodic film grown to U_F = 5V on Ti-6at.%Si, recorded at different wavelengths in 1 M H_3PO_4. Continuous lines are plotted according to eq. 5.11 with the fitting parameters of Table 5.2

In Fig. 5.9 we report the photocharacteristics relating to the 5 V anodic films on Ti-6at.%Si at different photon energy, recorded in 1 M H_3PO_4. We have overlapped to the experimental points the curves obtained according to eq. 5.11 with the fitting parameters reported in table 5.2. Eq. 5.11 requires the knowledge of the flat band potential and, for n-type semiconducting films, of x_{SC}^0 . Both these parameters were estimated fitting the differential capacitance curves of Fig. 5.6a, which allowed to estimate U_{FB} = - 0.235 V(Ag/AgCl) and x_{SC}^0 = 48 Å, corresponding to a density of state N(E) ~ $7 \cdot 10^{19}$ cm^{-3} eV^{-1}. According to this it was calculated that a band bending $\Delta\Phi_{SC}$ = 300 mV is enough to make the space charge region coincident with the whole film thickness. For higher band bending the usual formula valid for insulating material was used to calculate the average electric field in analogous way as operated for thick (20 V and 40 V) anodic films in all potential range. The employed U_{FB} is very close to the zero photocurrent potential estimated from the photocharacteristics in the same electrolyte.

We have to mention that an influence of the photon energy of the experimental U_{FB} value is expected due to the presence of surface states, since light can affect the potential distribution at the oxide/electrolyte interface, due a change in the potential drop at the Helmholtz double layer on going from dark to irradiation [5.20]. This can be taken into account by inserting in table 5.2 the parameter ΔU_{FB}, which is expected to be sensitive for strongly absorbed light. At variance with film formed on pure Ti metal [5.6], this shift is negligible (well below the experimental uncertainty) for 5 V anodic films on Ti-6at.%Si in a large range of wavelengths (340 – 270 nm). At the lowest employed wavelength (λ = 250 nm) a shift of less than 0.075 V in U_{FB} was used for having a very good fitting for photocharacteristics recorded in both 1 M H_3PO_4 and 0.1 M ABE. This experimental finding suggests the presence of a much lower density of surface states in the film grown on magnetron sputtered Ti-6at%Si alloy. This fact could explain also the better agreement between theoretical and experimental curves in the low band bending region, but it is in our opinion that the Braun-Onsager model is also a more appropriate choice in modelling the low band bending region.

We like to mention that the value of dielectric constant used to calculate b was very important in obtaining a good fitting of the experimental curves. Too much lower values of $\langle\varepsilon\rangle$ as that employed previously ($\langle\varepsilon\rangle$ = 16) to fit the photocharacteristics of pure TiO_2 film, in the frame of the Pai-Enck-Onsager's model, did not allow to get a good agreement between experimental and theoretical curves in the low wavelength regions (i.e. 340 nm) where the Onsager approach to the calculation of initial separation of bound excitons is particularly necessary.

On the other hand at the shortest employed wavelengths (λ = 250 nm) a good fitting of the experimental curve was obtained also by inserting values of $\langle\varepsilon\rangle$ near to that reported in the optical frequency region where the $\langle\varepsilon\rangle$ is equal to the square of refractive index. However in this case large values of the $k_f/k_d(0)$ ratio were necessary to get a good fitting agreement.

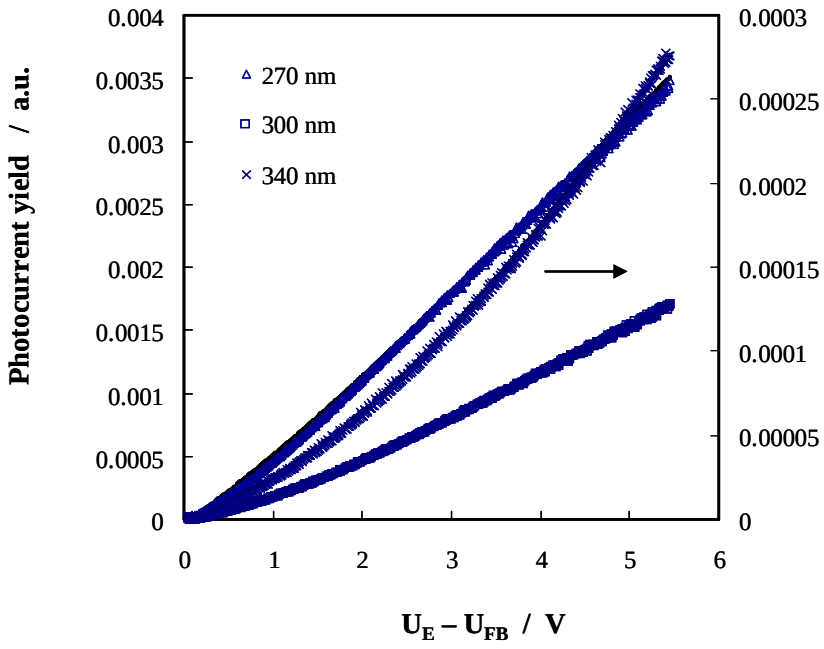

Fig. 5.10 Photocurrent vs band bending relating to anodic film grown to U_F = 40 V on Ti-6at.%Si, recorded at different wavelengths in 0.1 M ABE. Continuous lines are plotted according to eq. 5.11 with the fitting parameters of Table 5.3.

In Fig. 5.10 we report the fitted photocharacteristics for 40 V anodic films. Due the insulating character of this oxide, the electric field was estimated as $\frac{(U_E - U_{FB})}{d_{ox}}$, where U_{FB} was estimated as the inversion photocurrent potential (see Fig. 5.5a).

The inspection of the fitting parameters reported in Table 5.2 and Table 5.3 as a function of the incident wavelengths, shows in both cases a clear decrease of the $k_f / k_d(0)$ ratio with increasing photon energies whilst, interestingly, the ratio of $k_{d\ 250\ nm} / k_{d\ 340\ nm}$ changes slightly with increasing film thickness. By using the data relatively to the thin film we observed that such a ratio reaches a value of about 10. By recalling the expression of $k_d(0)$ reported in eq. 5.8 and by assuming for k_f and ω_0

the value of 10^9 s^{-1} and 10^{12} s^{-1} respectively we can calculate the binding energy, E_b, of CTE as a function of wavelength and for different film. Values of E_b in the order of 0.24 eV and 0.15 eV have been calculated by using eq. 5.8, from which the polaron pair radius can be estimated.

The data of Table 5.2 and Table 5.3 discloses another important aspect relating to the flat band potential as a function of the film thickness. A shift of ~ 0.15 V toward the anodic direction of U_{FB} on going from 5 V to 40 V anodic films is reported, in spite of the almost coincident band gap value (see Figs. 5.1 and 5.2). Moreover good fittings of the I_{ph} vs U_E curves in the case of thicker insulating film were obtained by using a shift in the U_{FB} value in the order of 0.025 - 0.075 V with the lowest value pertaining to the experiments carried out at longer wavelengths (340 nm). The small shift of U_{FB} (ΔU_{FB}) under illumination poses a limit to a density of surface states in the order of 10^{13} cm^{-2} eV^{-1}

On the other hand the more anodic U_{FB} value of thicker (20 V and 40 V) films is in agreement with their insulating behaviour evidenced by the presence of an inversion photocurrent potential in the photocharacteristics. This change in the electronic properties could be related to changes in the density of states distribution as well as to the stoichiometry owing to the film thickening. It is known that during the anodizing of Ti an amorphous to crystalline transition occurs even at low formation voltages (i.e. 10 V), which results in the formation of crystalline region with high electronic conductivity, where oxygen evolution occurs with consequent oxide breakdown. The formation of macro-voids due to O_2 evolution occurs mainly at the metal/oxide interface. According to refs. [5.8, 5.9], even small amounts of Si (i.e. 6at.%) can effectively delay the onset of crystallization processes keeping amorphous up to high formation voltages (65 V for aged alloys) the inner part of oxide grown at the alloy/film interface, which is expected to be more sensitive to oxygen evolution. Since the n-type semiconducting character of anodic titanium oxide is usually attributed to the formation of a non-stoichiometric TiO_{2-x} anodic film, the inhibition of O_2 evolution can bring to a reduction of oxygen vacancy concentration, with a consequent shift of the film Fermi level toward more anodic value. The increase in energy distance of E_F with respect to the conduction band

edge (higher ΔE_F value) can account for the insulating character of thicker layers as evidenced also by the flattening of differential capacitance curves even at low ac frequency.

λ□ / nm	α / cm^{-1}	μτ / cm^2 V^{-1}	k_f / k_d(0)	ΔU_{FB} / V
250	$1.62 \cdot 10^5$	$1.51 \cdot 10^{-13}$	1.35	0.075
270	$1.23 \cdot 10^5$	$1.51 \cdot 10^{-13}$	4.5	0.03
300	$6.74 \cdot 10^4$	$1.50 \cdot 10^{-13}$	10.5	0.02
320	$2.99 \cdot 10^4$	$1.50 \cdot 10^{-13}$	14	0.02
340	$8.42 \cdot 10^3$	$1.50 \cdot 10^{-13}$	14	0

Table 5.2 Fitting parameters relating to the photocharacteristics, recorded at different wavelengths in 1 M H_3PO_4, for anodic film grown to 5 V on Ti-6at.%Si. x_{SC}^0 = 48 Å, U_{FB} = -0.235 V (Ag/AgCl) and ε = 31

λ / nm	α / cm^{-1}	μτ / cm^2 V^{-1}	k_f / k_d(0)	ΔU_{FB} / V
270	$1.23 \cdot 10^5$	$1.0 \cdot 10^{-13}$	0.38	0.075
300	$6.74 \cdot 10^4$	$1.0 \cdot 10^{-13}$	1.45	0.025
340	$8.42 \cdot 10^3$	$1.5 \cdot 10^{-13}$	2.8	0

Table 5.3 Fitting parameters relating to photocharacteristics, recorded at different wavelengths in 0.1 M ABE at different wavelengths, for anodic film grown to U_F = 40 V on Ti-6at.%Si. U_{FB} = -0.45 V (Ag/AgCl) and ε = 31

5.6 Conclusions

A photoelectrochemical characterization of amorphous anodic film grown on Ti-6at.%Si was carried out as a function of film thickness in two different aqueous solutions, spanning a large pH range, allowing to get more insights on the solid state properties of the films as well as on the generation and transport of photocarriers.

A band gap of ~ 3.4 eV was estimated for Si containing film, higher that those reported for crystalline TiO_2. This difference is attributed to the amorphous nature of the oxide even at high formation voltages.

In spite the constant E_g value as a function of the film thickness, a change from n-type semiconducting material to insulating was evidenced by the photocharacteristics and by the capacitance measurements, together with a shift toward the anodic direction of the oxide flat band potential. These experimental findings suggest that a more stoichiomteric film (lower oxygen vacancy concentration) grows the higher the formation voltage is.

The absence of crystallization in a wide range of thickness due to the incorporation of Si species in the inner part of the film allowed to fit in a quantitatively way the behaviour of photocharacteristics as a function of the electric field and energy of incident photons. A very good quantitative agreement was observed by fitting the experimental photocurrent vs potential curves with a Braun-Onsager model previously used to explain the geminate recombination process in organic semiconductors. The use of Braun-Onsager model to explain the field dependence of photocurrent as a function of electrode potential in the frame of theory of amorphous semiconductor allowed to get a better fitting in the low band bending region where larger geminate recombination effects are expected. Smaller drift range ($\mu\tau$) for injected photocarriers into anodic films on Ti-6at.%Si alloy were measured if compared with films grown on pure Ti foil at the same final potential and under identical conditions. This finding is in agreement with the different photocurrent vs potential behaviour reported in the paper and it can be attributed to a weakening of the geminate recombinations of photocarriers in pure TiO_2 anodic films where a crystallization process start at lower potentials. The results of this investigation allow to reach a better insight on the influence of different experimental parameters on the crystallization process of TiO_2 anodic film by using in situ PCS technique.

REFERENCES

[5.1] D.B. Strukov, G.S. Snider, D.R. Stewart, R.Stanley Williams, Nature Letters 453, (2008), 80.

[5.2] D. Li, M. Li, F. Zahid, J. Wang, H. Guo, Journal of Applied Physics, 112, (2012), 075312.

[5.3] M. Schneider, S. Schroth, J. Schlim, A. Michaelis, Electrochimica Acta, 54, (2009), 2663.

[5.4] F. Di Quarto, K. Doblhofer , H. Gerischer, Electrochimica Acta, 23, (1978), 195.

[5.5] S. Piazza, L. Calà, C. Sunseri, F. Di Quarto, Berichte der Bunsengesellschaft/Physical Chemistry Chemical Physics, 101, (1997), 932.

[5.6] F. Di Quarto, S. Piazza, C. Sunseri, Electrochimica Acta, 38, (1993), 29.

[5.7] H. Habazaki, M. Uozumi, H. Konno, K. Shimizu , P. Skeldon, G.E. Thompson, Corrosion Science, 45, (2003), 2063.

[5.8] H. Habazaki, K. Shimizu, S. Nagata, P. Skeldon, G.E. Thompson, G.C. Wood, Corrosion Science, 44, (2002), 1047.

[5.9] M. Tauseef Tanvir, K. Fushimi, K. Shimizu, S. Nagata, P. Skeldon, G.E. Thompson, H. Habazaki, Electrochimica Acta, 52, (2007), 6834.

[5.10] F. Di Quarto, F. Di Franco, C. Monarca, M. Santamaria, H. Habazaki, Electrochimica Acta, 110, (2013), 517.

[5.11] F. Di Quarto, G. Russo, C. Sunseri, A. Di Paola, Journal of the Chemical Society, Faraday Transactions 1: Physical Chemistry in Condensed Phases, 78 ,(1982), 3433.

[5.12] a) L. Onsager, J. Chem. Phys., 2, (1934), 599; b) L. Onsager**,** Physical Review **,** 54, (1938), 554.

[5.13] D. M. Pai, R.C. Enck, Phys. Rev. B, 11, (1975), 5163.

[5.14] C. L. Braun, J. Chem. Phys., 80, (1984), 4157.

[5.15] R.A. Street, Physical Review B, 84, (2011), 075208.

[5.16] O.S. Heavens, Optical properties of thin solid films, Dover Publications, New York, 1965.

[5.17] Z. Zhao, B. K. Tay, G. Yu, Applied Optics, 43, (2004), 1281.

[5.18] D. R. Lide (Editor), Handbook of Chemistry and Physics, 89th edition, CRC Press, New York, 2008.

[5.19] F. Mollers, H. J. Tolle and R. Memming, J. Electrochem. Soc., 121, (1974), 1160.

[5.20] D. S. Kong, Langmuir, 24, (2008), 5324.

6 Photoelectrochemical polymerization of PEDOT on anodic films of magnetron sputtered Nb, Nb-Ta and Ti-Si alloys.

6.1 Introduction

A conventional electrolytic capacitor consists of a valve metal (e.g. aluminium or tantalum), covered by an anodic film, the dielectric, in direct contact with an electrolyte, the true counter electrode, which in turn is connected to a current collector, usually made by the same valve metal. In the so called "solid state" tantalum electrolytic capacitors, the liquid electrolyte has been substituted by a solid ionic conductor (β-MnO_2), whose conductivity is one of the drawbacks of the device. Thus, it has been recently proposed in the literature to replace manganese dioxide with a conductive polymer, which in principle can show a conductivity comparable to that of a metal [1.2a].

Since 1999 [1.2b], poly(3,4-ethylenedioxythiophene) has been successfully proposed as suitable conducting polymer for tantalum solid capacitor due to its excellent environmental stability. Usually, PEDOT is synthesized chemically in aqueous medium in presence of an oxidizer agent (i. e. ferric sulphate). However, this method can leave strongly acidic oxidant on the polymer chains, which can cause the degradation of the dielectric, thus the electropolymerization should be safer for preparing PEDOT to be employed as counter electrode in solid state capacitors [6.1]. To overcome the difficulty of performing such electrochemical process on dielectrics, Di Quarto et al. recently proposed a photoelectrochemical method [6.2] to grow polypyrrole on tantalum oxide. Such method has been successfully employed to synthesize PEDOT on Ta_2O_5 [6.1] and on Ti-Zr mixed oxides [6.3].

On the other hand, high cost and limited availability of tantalum natural resources are pushing capacitor technologists to replace Ta with Nb, which is more abundant in earth crust and whose oxide, i. e. Nb_2O_5, has a permittivity higher than that measured for Ta_2O_5. However, as far as we know, only a paper has been published reporting on the chemical polymerization of pyrrole and aniline on Nb_2O_5 to be employed in electrolytic capacitors [1.2c].

Organic field-effect transistors (OFETs) employing polymeric semiconductors have attracted great interest in the market of displays, sensors, inverters, and radio frequency identification tags [1.3, 6.4]. OFETs fabrication technology exhibits, however, several drawbacks, such as low output current and high operating voltage due to the low charge carrier mobility of organic semiconductors. A possible way to overcome these limitations is to find a good compromise between both gate oxide dielectric constant (ε_{ox}) and thickness (d_{ox}). Oxides with selected ε_{ox}/d_{ox} can be easily prepared by anodization, a room temperature wet electrochemical process, which gives the chance to tune the electronic properties of the films by an accurate selection of the alloy composition and of the anodizing conditions. It is proved how the alloying of Ti with small amount of Si allows to grow amorphous anodic oxides with high dielectric constant (see chapter 5 and refs. [5.8-5.10]). The presence of silicon is reported to hinder the occurrence of crystallization phenomena responsible of anodic TiO_2 breakdown. Because of the dielectric properties of these oxides, a low electronic current it is expected to circulate after the oxide formation. Therefore, in order to complete the OFET structure, a photoelectrochemical process can be designed to allow the growth of the semiconducting polymer.

In this chapter we report on the photoelectrochemical polymerization of PEDOT on anodic films grown on magnetron sputtered Nb, Ta-85at.%Nb and Ti-6at.%Si alloys. Photocurrent Spectroscopy was employed to study the optical properties of metal/anodic oxide/PEDOT/electrolyte interface in a large range of potential, while Scanning Electron Microscopy was used to get information of the morphology of PEDOT. The features of the photoelectrochemically grown polymer were also compared with those showed by PEDOT electropolymerized on gold conducting substrate. Finally, output transistor characteristics are recorded in order to test the performance of the junctions in the IOFET structure.

Part of this work was realized in collaboration with research group of Prof. C. Calì (Università di Palermo, Electronic Engineering Department).

Part of the results of this chapter are reported in refs. [6.5 – 6.6].

6.2 Experimental

Electro-polymerization was performed on gold electrode (rod 4 mm diameter or foils) in 0.1 M $LiClO_4$ propylene carbonate (PC, 99.8 Sigma-Aldrich) with 0.1 M 3,4-ethylenedioxythiophene (Edot).

Niobium films (300 nm thick) were magnetron-sputtered onto a glass substrate using a 99.9% pure niobium target of 100 mm diameter. The deposited niobium had a body-centred cubic structure with a 110 preferred orientation. These films were anodized at a constant current density of 50 A cm^{-2} in 0.1 mol dm^{-3} ammonium pentaborate at 293 K, the potential being kept constant for 1 h at the final cell voltage of 50 V [4.2].

Anodic films grown on Ta-85at.%Nb and on Ti-6at.%Si were prepared by anodizing as shown in Chapters 3 and 5.

The photo-electron-polymerization was performed in 0.1 M $LiClO_4$ propylene carbonate (PC, 99.8 Sigma-Aldrich) with 0.04 M 3,4-ethylenedioxythiophene (Edot) concentration under constant irradiation (λ = 310-320 nm).

The PEDOT morphology was investigated using a Philips XL30 ESEM scanning electron microscope. Some of the PEDOT films were detached from the substrate with copper conducting adhesive in order to allow the view of electrode side polymer and of its cross section.

Micro Raman analysis were performed through a Renishaw inVia Raman Microscope spectrometer equipped with a microprobe (50×) and a CCD detector with a Nd:YAG laser of 532 nm.

The metal/oxide/PEDOT/electrolyte junction was investigated by PCS (see chapter 2).

To fabricate a OFET structure (anodic films grown on Ti-6at.%Si), 100 nm-thick Au source and drain top contacts were deposited onto the polymer by thermal evaporation. A shadow mask was used to obtain a gate channel of about 150 μm and 4.5 mm width. The fabricated OFET devices were characterized at room temperature using a Keithley 6487 source-meter unit (Keithley Instruments, Inc.) under LabVIEW environment. More details on fabrication and characterization of the devices are reported in our previous work [6.7].

6.3 Electrodeposition and characterization of PEDOT on gold

In Fig. 6.1 we report the current density vs time curve recorded by polarizing a gold electrode at 1.2 V (Ag/AgCl) in 0.1 M $LiClO_4$ PC (Propylene Carbonate) solution containing 0.1 M Edot (3,4-ethylenedioxythiophene).

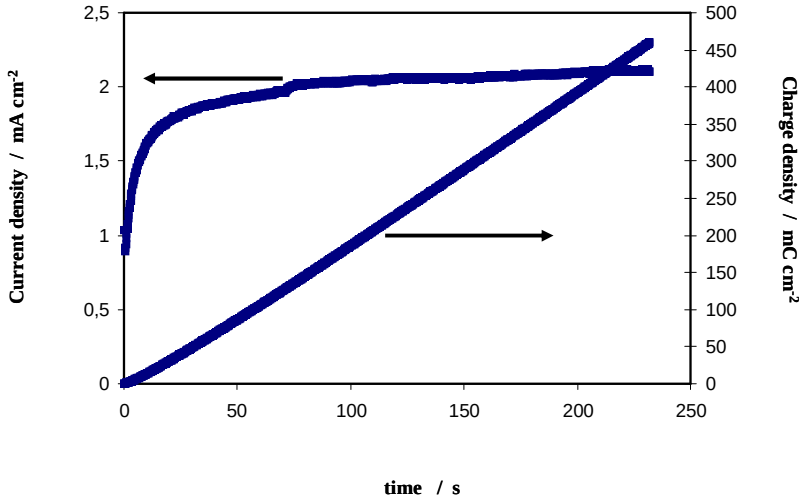

Fig. 6.1 Current density and charge density vs time recorded by polarizing the electrode (gold rod) at 1.2V (Ag/AgCl) in 0.1M $LiClO_4$ propylene carbonate solution containing 0.1 M Edot.

This potential value is more anodic than the oxidation potential of Edot/$Edot^+$ couple (E_{ox} = 1.1 V vs Ag/AgCl in PC, according to ref. [6.8]) but is lower than oxidation potential of propylene carbonate (E_{ox} = 1.8 V vs Ag/AgCl, according to ref. [6.9]). Thus, we can attribute the measured current to the oxidation of monomer and to its subsequent polymerization, according to the following processes:

$$nEdot(sol) \rightarrow nEdot^+ \cdot + ne^- \qquad (6.1a)$$

$$nEdot^+ \cdot + zClO_4^- \rightarrow (n-z)H^+ + \left[(Edot_n)^{z+}(ClO_4^-)_z\right] \qquad (6.1b)$$

where ne^- are n-electrons, nEdot are n-monomers of ethylene dioxythiophene, $nEdot^+$ are n-radical cations of Edot and z is a measure of the doping level of polymer. In eqs. (6.1a) and (6.1b), usually reported for the electropolymerization of pyrrole and thiophene on conducting substrates [6.10], the formation of Edot radical cations is the preliminary step toward the polymer growth and its simultaneous doping according to eq. (6.1b) [6.11]. The curve of Fig. 6.1 is analogous to those reported in the literature for the electropolymerization of 3-4 ethylene dioxythiophene performed in very similar experimental conditions [6.12-6.13]. After a very short induction time (~ 0.4 s), during which we suppose that the oxidation of monomers brings to the formation of soluble oligomers [6.13], the nucleation of the polymer on the gold surface begins with the subsequent thickening of the PEDOT layer. A careful SEM analysis of polymer cross sections (see Fig. 6.2a) allowed to estimate an average thickness of ~ 1.4 μm for PEDOT after circulation of 460 mC cm^{-2}, corresponding to a polarization time of 230 s (see Fig. 6.1). If we assume for PEDOT a density of 1.5 g cm^{-3} [6.1], it is possible to estimate an electropolymerization efficiency of 70 % by comparing the experimental thickness to that estimated according to Faraday law:

$$d = \frac{PM}{\mathrm{nF}\rho} q \qquad 6.2$$

where PM is the monomer molecular weight (i.e. 142 g mol^{-1}), ρ is the polymer density, q is the charged per unit surface in C cm^{-2} and n is assumed 2.25, since the polymerization of Edot is assumed to involve two electrons while the partial oxidation of already grown film (i.e. doping) is assumed to consume the excess 0.25 charge [6.14]. An efficiency lower than 100 % can be explained by the occurrence of coupling reactions between radicals bringing to formation of oligomers soluble in the electrolyte (not only during the induction time), the occurrence of doping process of already grown polymer, which reduces the charge effectively employed for the polymer thickening.

In Figs. 6.2 a-d we report the SEM micrographs relating to the morphology of the polymer surface after three different circulated charges.

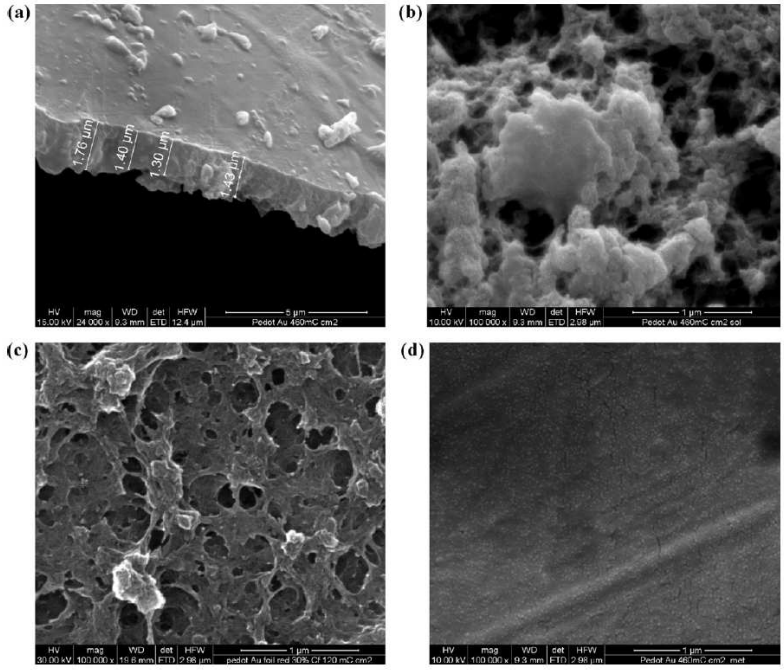

Fig. 6.2 SEM micrographs relating to PEDOT grown potentiostatically at Ue = 1.2V (Ag/AgCl) on gold. (a) Cross section of polymer after circulation of 460 mC cm^{-2}; solution-side surface morphologies after circulation of (b) 460 mC cm^{-2}, (c) 120 mC cm^{-2}, and (d) electrode side morphology.

By comparing the pictures, it comes out that PEDOT becomes more porous with increasing the circulated charge. The morphology is different with respect to that shown by PEDOT prepared in water [6.15] and in methyl benzoate solutions [6.16], but very similar to that shown by the film electropolymerized in propylene carbonate in spite of different supporting electrolyte and bath temperature [6.16]. This finding indicates a strong influence of the solvent on the morphology of the layer. A different morphology is shown by the polymer-electrode side (see Fig. 6.2d), which appears very compact. This is in agreement with a porosity increasing with increasing circulated charge.

In Fig. 6.3 we report the cyclic voltammetry recorded by sweeping the potential of the gold/polymer electrode at 10 mV s^{-1} in a 0.1 M $LiClO_4$ in PC.

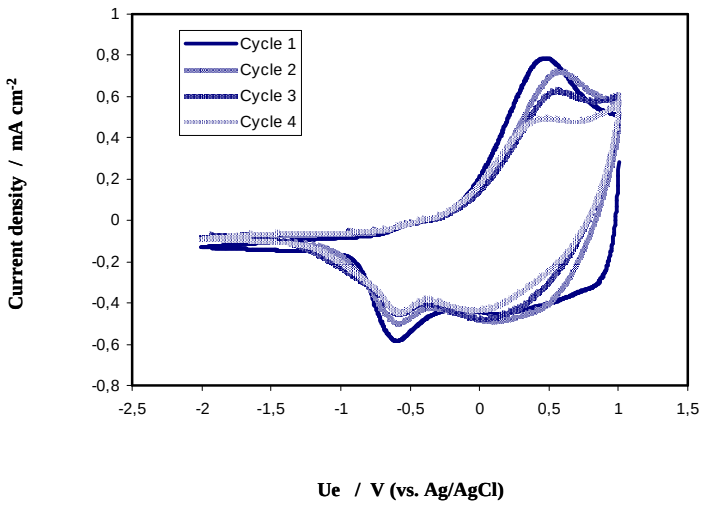

Fig. 6.3 Cyclic voltammetry relating to PEDOT film electrochemically grown after circulation of 460mC cm^{-2} on gold electrode, recorded at 10mVs^{-1} in 0.1 M $LiClO_4$ propylene carbonate solution.

During the forward scan an anodic peak is present at 0.5 V (Ag/AgCl), which can be attributed to the doping process of polymer chains, while in the reverse scan two cathodic peaks, at - 0.2 and - 0.6 V (Ag/AgCl), correspond to the de-doping process [6.8]. In the voltage range between - 2 V and - 0.6 V (Ag/AgCl) the polymeric film is stable and its electronic structure is not modified.

The grown polymer was not photoactive at the formation voltage, whilst cathodic photocurrent was observed under cathodic polarization. In Fig. 6.4a we report the photocurrent vs wavelength curve at constant potential (photocurrent spectrum) recorded by polarizing the polymeric film of Fig. 6.1 at – 2 V (Ag/AgCl) in 0.1 M $LiClO_4$ PC.

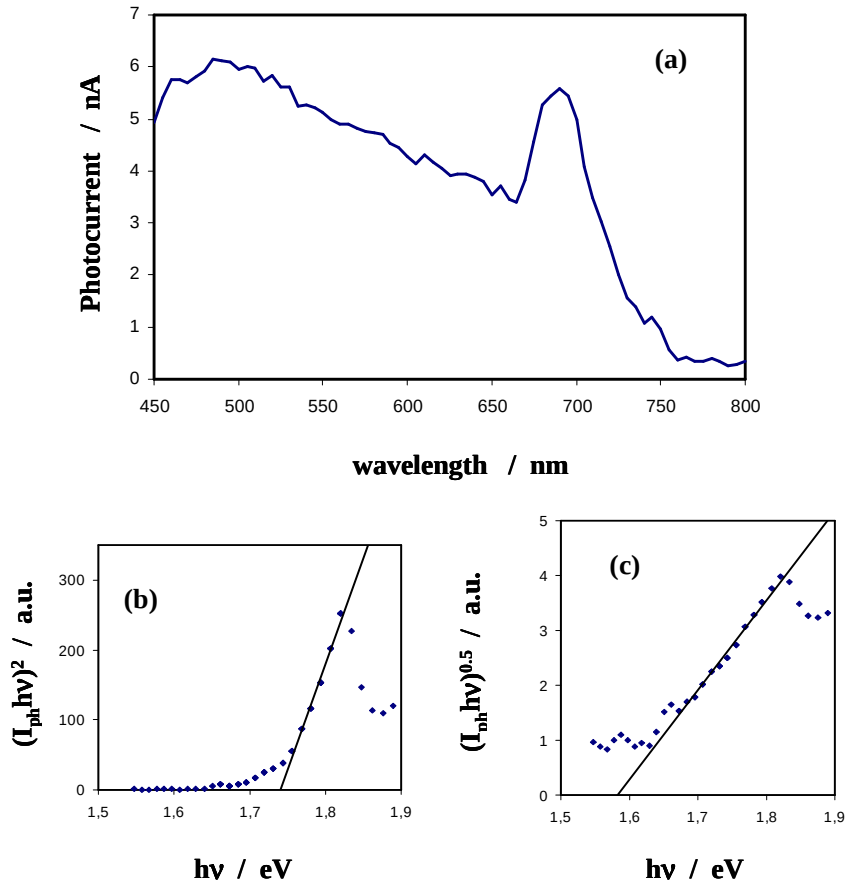

Fig. 6.4 (a) Raw cathodic photocurrent spectrum relating to PEDOT film electrochemically grown after circulation of 460 mC cm^{-2} on gold electrode, recorded by polarizing the Au/Pedot interface in 0.1 M $LiClO_4$ propylene carbonate at Ue = −2V (Ag/AgCl). Band gap estimate by assuming (b) direct and (c) non-direct optical transitions.

At this potential the photocurrent is cathodic as expected due to the p-type semiconductor nature of the polymer. From the photocurrent spectra for photon energy in the vicinity of the band gap, it is possible to estimate the optical band gap value of the polymer by following equation (according to the equation 2.31 and 2.38):

$$(I_{ph}h\nu)^n \propto (h\nu - E_g^{opt}) \qquad 6.3$$

where, I_{ph} is the photocurrent yield, assumed proportional to the light absorption coefficient, hν is the photon energy, E_g^{opt} , the optical band gap and an n value equal to 0.5 has been assumed for indirect optical transitions and n value equal to 2 has been assumed for direct optical transitions (see chapter 2 and ref. 2.36). As shown in Figs. 6.4b and 6.4c, a direct optical transition at 1.74 eV and an indirect one at around 1.58 eV were determined, both values being very close to those reported in previous works for PEDOT [6.8, 6.17]. Moreover, the direct optical band gap of PEDOT agrees quite well with the theoretically estimated HOMO-LUMO gap (1.68 - 1.83 eV) of oligomers extrapolated to infinite chain length [6.18]. The lower band gap measured in the hypothesis of indirect (or non-direct if amorphous) optical transitions could be attributed to the formation, near the valence band of PEDOT, of a band of defects (polaron and/or bipolaron) during the de-doping process [6.19].

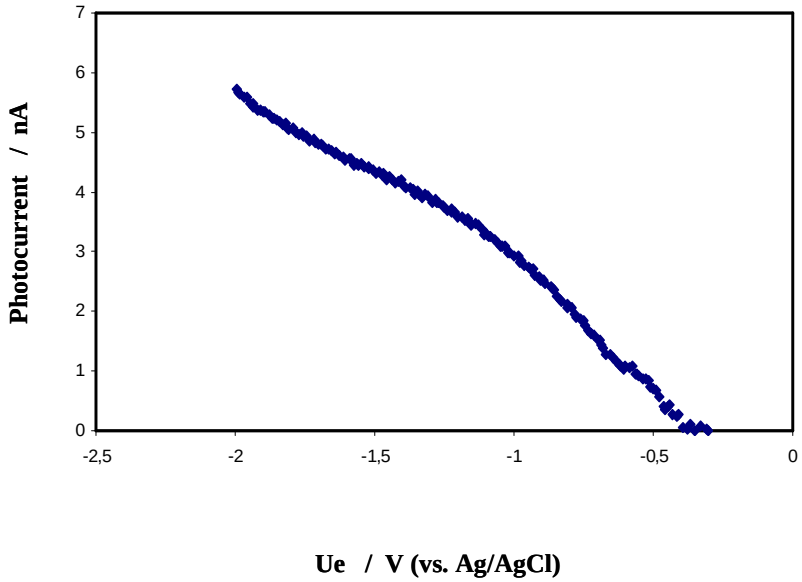

Fig. 6.5 Photocurrent vs potential curve relating to PEDOT film electrochemically grown after circulation of 460 mC cm^{-2} on gold electrode, recorded by irradiating the Au/PEDOT interface in 0.1M $LiClO_4$ propylene carbonate at 485 nm.

In Fig. 6.5 we report the photocurrent vs potential curve (photocharacteristic) recorded by irradiating the polymer surface at 485 nm in 0.1 M $LiClO_4$ PC electrolyte. By moving the polarizing voltage toward the anodic direction at 10 mV s^{-1}, the photocurrent decreases as typical of p-type semiconductors. It is interesting to mention that the photocurrent goes to zero at - 0.55 V (Ag/AgCl), that can be assumed as a rough estimate of the flat band potential in propylene carbonate. The occurrence of doping process at potential very close or more anodic with respect to this value (see Fig. 6.3) induces the metallization of the polymer and hinders the possibility to detect any photocurrent.

6.4 Photo-electrodeposition and characterization of PEDOT on anodic films on magnetron sputtered Nb and Ta-85at.%Nb alloy.

In Fig. 6.6a we report the photocurrent spectrum relating to the 50 V anodic film on magnetron sputtered Nb (grown galvanostatically), recorded by polarizing the electrode at 8 V vs (Ag/AgCl) in 0.1 M $LiClO_4$ PC electrolyte. According to eq. 2.31 and 2.38, a non-direct band gap value of 3.42 eV (see figure 6.6b) can be estimated, which is very close to that previously estimated in aqueous solution for films grown on Niobium in the same conditions [4.2]. The location of characteristic energy levels of the junction (flat band potential, U_{fb} ,conduction and valence band edges) was carried out by assuming the zero photocurrent potential, V*, derived from the photocurrent vs potential plot at 320 nm (Fig. 6.7), as a proxy of the flat band potential (U_{FB} = - 0.5 vs Ag/AgCl) of the oxide/organic electrolyte interface. If we assume that the organic electrolyte is equivalent to an aqueous solution at the niobium oxide isoelectric point (pH_{pzc}), this value compares well with the U_{FB} reported in ref. [4.2] estimated in strongly acidic electrolyte, according to the following equation:

$$U_{FB} = U_{FB\ pHpzc} - 0.059(pH - pH_{pzc}) \qquad 6.4$$

where pH_{pzc} = 4.1 for Nb_2O_5 [3.21]. From such estimate, after location of the conduction band mobility edge of oxide around 0.37 eV above U_{FB} [4.2], the energy

level of the valence band edge of anodic Nb_2O_5 was located at around 2.55 eV below the reference electrode, i.e. at about 0.75 eV below the oxidation potential of propylene carbonate (E_{ox} = 1.8 V vs Ag/AgCl, according to ref. [6.9]). This estimate of energy levels of the junction agrees with the observed anodic photocurrent, in absence of monomer, attributed to the photo-electrochemical oxidation of the solvent.

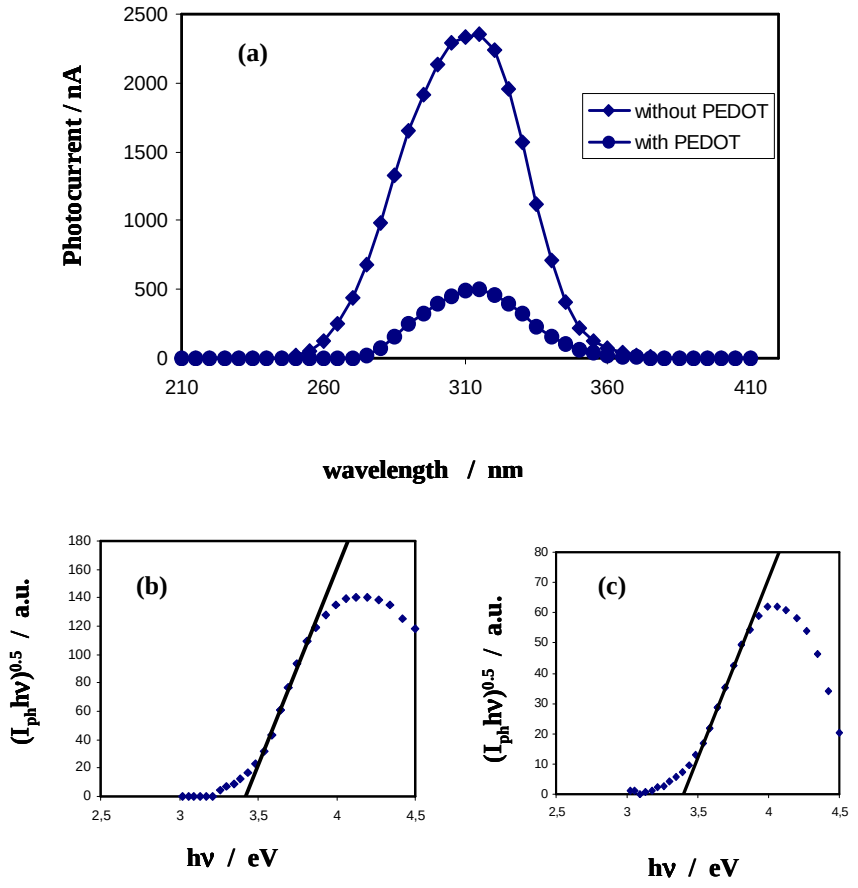

Fig. 6.6 (a) Raw anodic photocurrent spectrum relating to an anodic film of Nb_2O_5, without and with PEDOT on the irradiated surface, recorded by polarizing the electrode in 0.1 M $LiClO_4$ propylene carbonate at 3V (Ag/AgCl). $(I_{ph}h\nu)^{0.5}$ vs hν plots relating to the oxide (b) without and (c) with PEDOT.

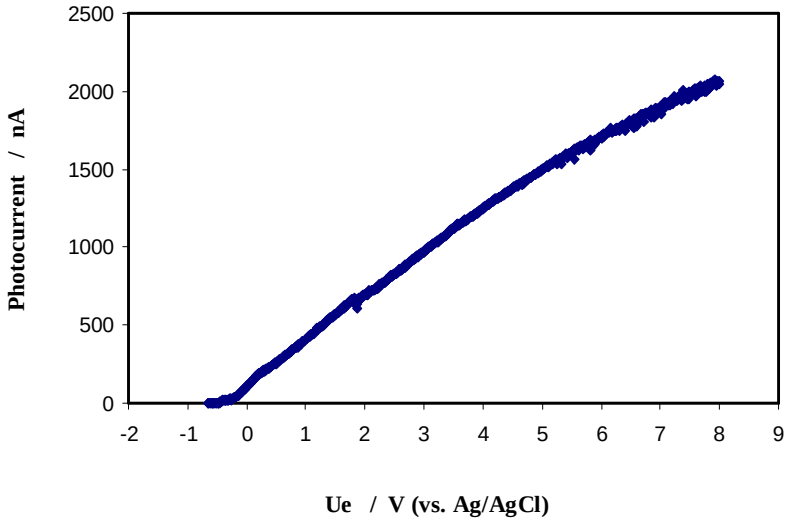

Fig. 6.7 Photocurrent vs potential curve relating to an anodic film of Nb_2O_5, recorded by irradiating the electrode in 0.1 M $LiClO_4$ propylene carbonate at 320 nm.

In Fig. 6.8 we show the schematic picture of the energetic levels at the oxide/organic interface.

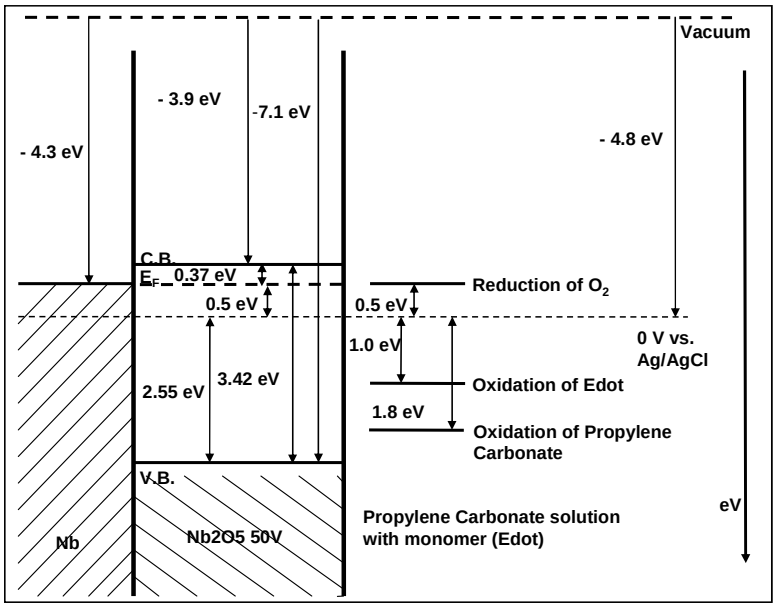

Fig. 6.8 Schematic picture of the energetic levels at the Nb/Nb_2O_5/organic solution (containing Edot) interface. The reported oxygen reduction potential is from Ref. [6.9]

In Fig. 6.9a we report the current vs. time curve recorded under irradiation (λ = 320 nm) by polarizing Nb_2O_5 at U_E = 8 V (Ag/AgCl), in 0.1 M $LiClO_4$ PC solution containing 0.04 M EDOT. By irradiating the anodic oxide surface with photon energy higher than the band gap of the anodic film (λ = 320 nm), the growth of polymer occurred according to the following processes:

$$Nb_2O_5 + h\nu \rightarrow e^-_{CB} + h^+_{VB} \qquad (6.5a)$$

$$nEdot(sol) + nh^+_{VB} \rightarrow nEdot^+ \cdot \qquad (6.5b)$$

$$nEdot^+ \cdot + zClO^-_4 \rightarrow (n-z)H^+ + \left[(Edot_n)^{z+}(ClO^-_4)_z\right] \qquad (6.5c)$$

where e_{CB}^- is an electron in the conduction band of oxide and h^+_{VB} is a hole in the valence band of oxide. Eqs. (6.5b) and (6.5c) are similar to eq. (6.1a) and (6.1b).

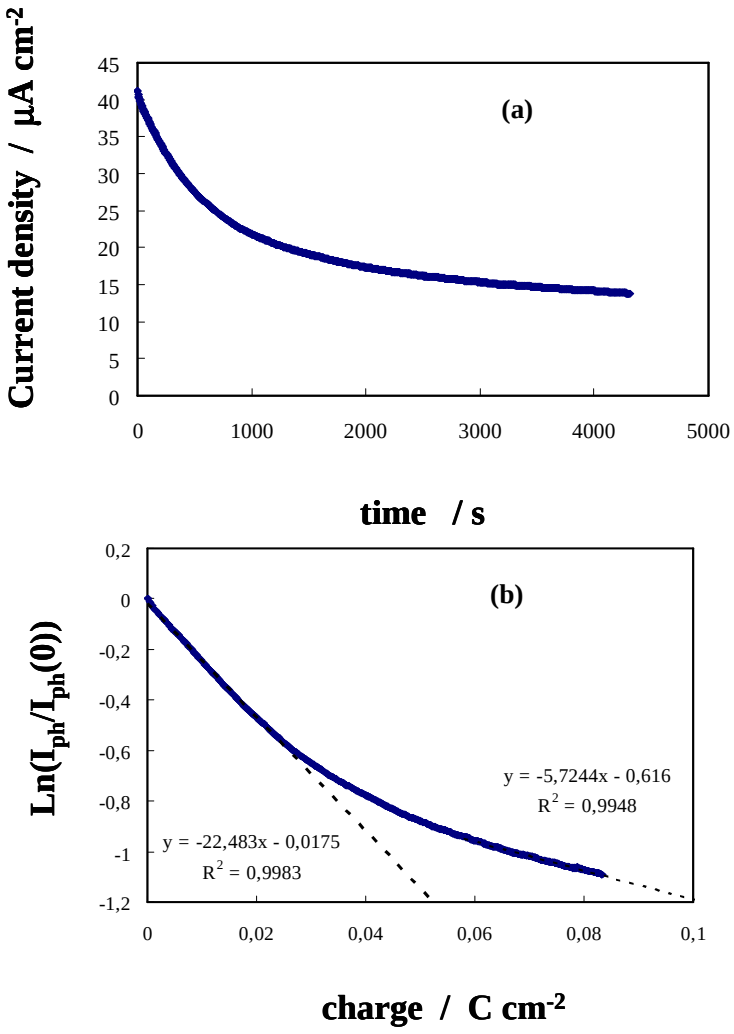

Fig. 6.9 (a) Current density vs time curve recorded by polarizing the electrode (Nb_2O_5) at 8V (Ag/AgCl) in 0.1 M $LiClO_4$ propylene carbonate solution containing 0.04 M Edot under irradiation at constant wavelength (λ = 320 nm). (b) Elaboration relating to the curve of (a) to determinate the α coefficient of PEDOT.

According to the energetics of the oxide/electrolyte interface of Fig. 6.8, it is evident that both the oxidation of Edot and of PC are thermodynamically possible. The occurrence of photo-electrochemical polymerization was confirmed by SEM analysis of the samples at short times or by direct visual inspection for longer photodeposition times.

As shown in Fig. 6.9b, during the early stages of photoelectrodeposition I_{ph} decreases almost exponentially as a function of the circulated charge, i.e. of polymer layer thickness. This behaviour can be explained by the reduced number of photons reaching the oxide surface with increasing polymer thickness. If we assume that the growing polymer behaves like an absorbing metallic layer with a constant light absorption coefficient, α, it is possible to fit the experimental curve according to the following eq.:

$$I_{ph}(q_{ph}) = I_{ph}(0) \exp(-4.9 \cdot 10^{-4} \alpha_{PEDOT} q_{ph}) \qquad 6.6$$

where I_{ph} is the photocurrent, α the light absorption coefficient of the growing polymer and q_{ph} the photocirculated charge per unit area. From the initial slope of the I_{ph} vs q_{ph} curve, a light absorption coefficient of ~ 4.8 10^4 cm^{-1} can be estimated by eq. 6.6, which is in agreement with the values reported in the literature and slightly lower than that estimated with the same procedure during the early stage of electropolymerization of polypyrrole on Ta_2O_5 but under irradiation of monochromatic light at shorter wavelength [6.2]. At longer photoelectropolymerization time a deviation from the linear slope is observed, that can be explained by considering that the photo oxidation occurs on a surface progressively larger with respect to the initial one owing to a spot light smaller that the whole exposed surface. A possible variation in the efficiency of the photo oxidation of Edot cannot be excluded although we have no experimental evidences supporting this hypothesis.

A morphological study of PEDOT photoelectrochemically grown on Nb_2O_5 electrodes was carried out. In Figs. 6.10 we report the SEM micrographs of solution-side and oxide-side PEDOT grown on niobium oxide. The morphologies in both

cases are really different with respect to those evidenced for electrochemically grown polymer (see Fig. 6.2).

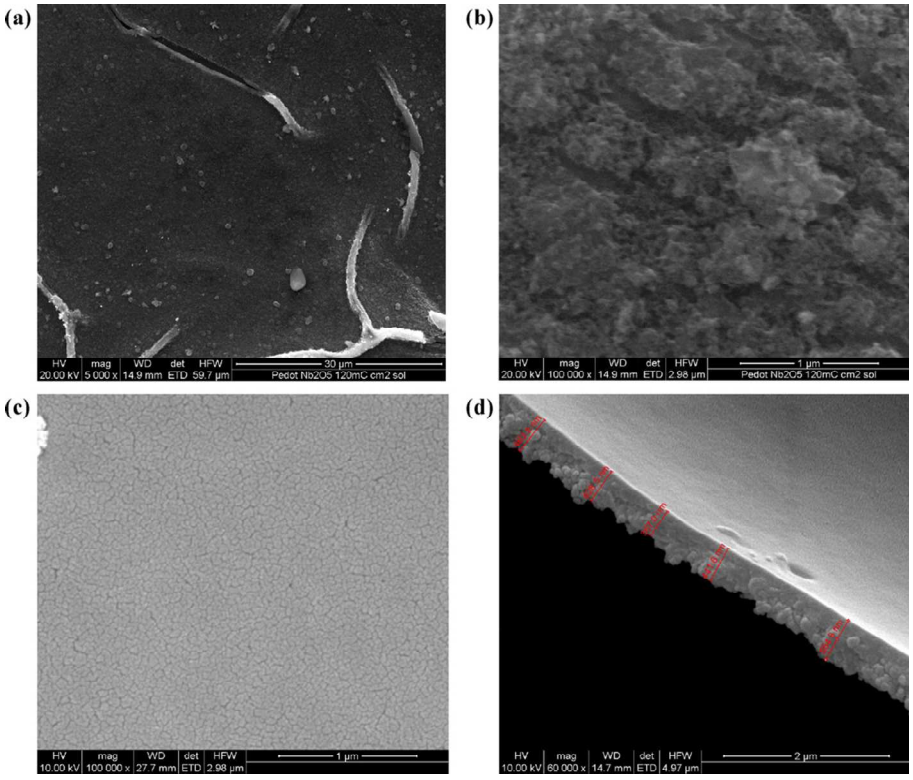

Fig. 6.10 SEM micrographs relating to PEDOT grown photoelectrochemically (λ = 320 nm) at U_e = 8V (Ag/AgCl) on Nb_2O_5 after circulation of 120 mC cm^{-2}. (a and b) Solution-side surface morphologies, (c) oxide side morphology and (d) cross section of polymer.

The solution side micrograph (Fig. 6.10a) reveals that the surface of the polymer is slightly corrugated, with the presence of compact and flat regions delimited by interconnected ridges of polymeric material, missing for electrochemically grown polymer even at higher circulated charges. Analogous morphology has been reported for Poly(3-hexylthiophene) grown by spinning coating on Li:ZnO film spin coated on ITO glass from sol-gel solution [6.20] as well for Polypyrrole film electrodeposited on ITO [6.21]. In this last work both the shrinkage and the drying of the polymer were discarded as possible source of wrinkles formation. According to our results these morphological features are rather independent from the method of growth of polymers so that the wrinkles seem originated during the growth process at the oxide/polymer interface and affected mainly by the polymer-oxide interaction governing the adhesion process. By comparing the morphological features of the polymer after doping and de-doping no appreciable differences were evidenced, thus suggesting that the morphology of the polymer is not strongly influenced by the anions incorporation.

At higher magnification an irregular morphology appears between the ridges on the solution side polymer but less porous than that shown by the electrochemically grown polymer after the same amount of circulated charge (compare Fig- 6.2c and 6.10b). A very uniform surface was observed on oxide side polymer formed by the cohesion of small polymer islands (Figs. 6.10c).

In Fig 6.10d we also report the SEM micrograph relating to the cross section of the photoelectrochemically grown polymer. By averaging the measured thickness on several areas of the same sample and on several samples, it was possible to estimate the efficiency of the process, as described in section 6.3, very close to that estimated for electrochemically grown polymer. In spite of the rough estimate, the efficiency is very close to that previously reported for the photo-electrochemical synthesis of polypyrrole on tantalum oxide in MeCN solution.

The presence of PEDOT in its metallic state on the surface of the anodic film does not modify appreciably the shape of the anodic photocurrent spectra with respect to those recorded in absence of polymer (see Fig. 6.6a), neither the value of measured optical band gap (see Fig. 6c). In fact its value (3.39 eV) is coincident

with that reported in Fig. 6b thus suggesting that the measured photocurrent is sustained by the photo-holes generated in the valence band of the niobium oxide.

The growth of polymer film partially absorbing the incident light accounts for the decreasing photocurrent intensity recorded under constant anodic polarization (see Fig. 6.9a). The formation of a metallic-like p-type degenerated semiconductor is suggested owing to the anion doping process described in eqs. (6.5c).

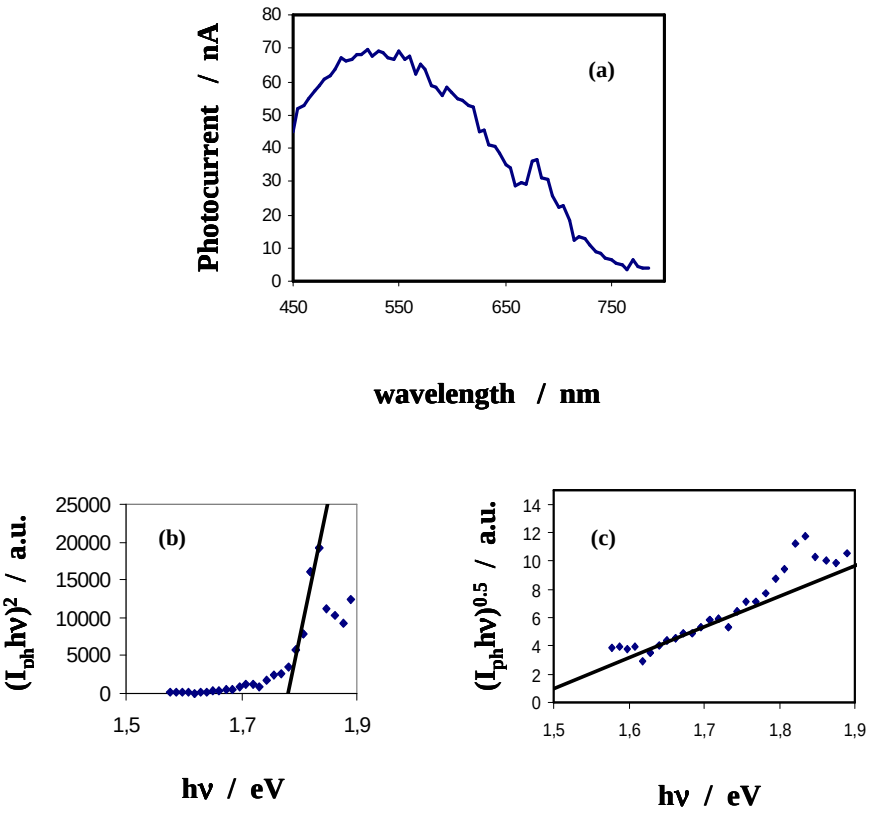

Fig. 6.11 (a) Raw cathodic photocurrent spectrum relating to PEDOT photoelectrochemically grown after circulation of 120 mC cm^{-2} on oxide (Nb_2O_5) electrode, recordedby polarizing the Nb/Nb_2O_5/PEDOT interface in 0.1M $LiClO_4$ propylene carbonate at U_e = − 2V (Ag/AgCl). Band gap estimate by assuming (b) direct and (c) non-direct optical transitions.

By polarizing the oxide/PEDOT/solution interface under cathodic potential, the de-doping process allows to evidence the p-type character of the polymer. In Fig. 6.11a we report the cathodic photocurrent spectrum of Nb_2O_5/PEDOT/solution junction recorded at - 2 V vs Ag/AgCl. A direct optical transition at 1.78 eV (Fig. 6.11b) and an indirect one at around 1.46 eV (Fig. 6.11c) were determined; both values being very close to those estimated for PEDOT grown on gold electrode.

In Fig. 6.12 we report the photocurrent vs potential curve recorded at 500 nm in 0.1 M $LiClO_4$ PC electrolyte relating to the polymeric film grown on Niobium oxide. From this figure it is possible to see that the potential of zero photocurrent is more cathodic than those measured for PEDOT grown on gold electrode; probably owing to an additional potential drop inside the niobium oxide absent for conducting substrate like gold.

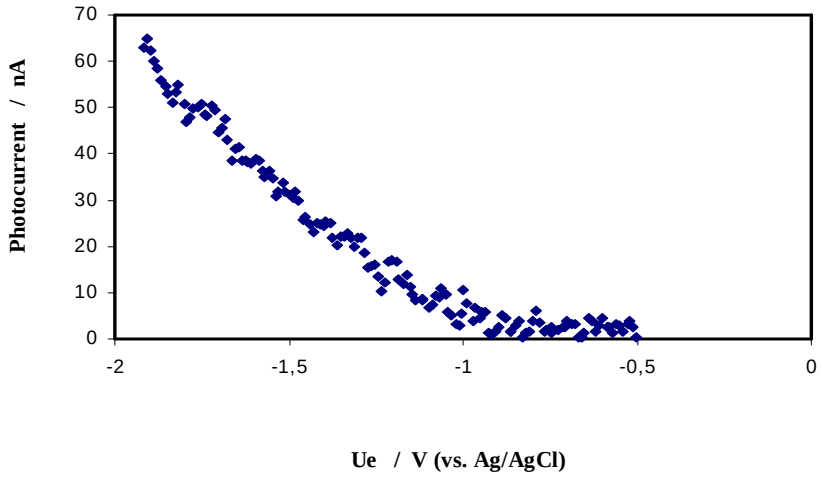

Fig. 6.12 Photocurrent vs potential curve relating to PEDOT film photoelectrochemically grown after circulation of 120 mC cm^{-2} on oxide (Nb_2O_5) electrode, recorded by irradiating the Nb/Nb_2O_5/Pedot/Solution interface in 0.1 M $LiClO_4$ propylene carbonate at 500 nm.

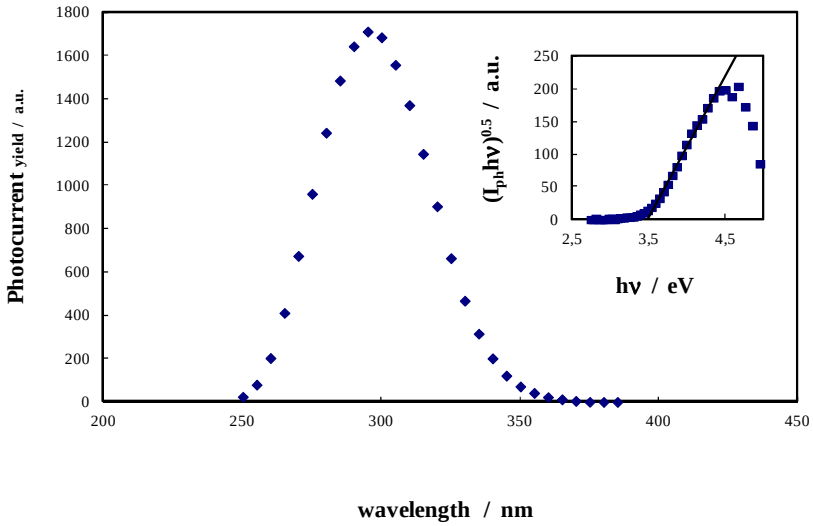

Fig. 6.13 Anodic photocurrent spectrum relating to an anodic film on Ta-85at.%Nb alloy (U_F = 10 V vs Ag/AgCl), recorded by polarizing the electrode in 0.1 M $LiClO_4$ propylene carbonate at 3V (Ag/AgCl). Inset: $(I_{ph}h\nu)^{0.5}$ vs hν plots relating to the oxide.

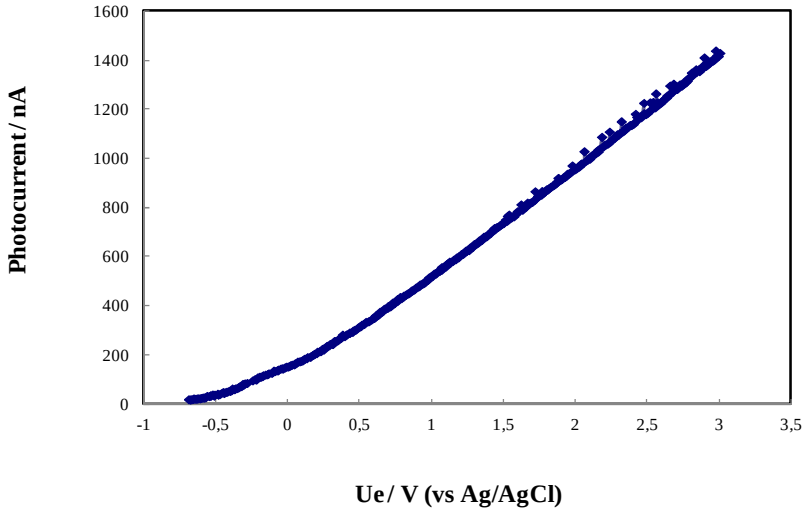

Fig. 6.14 Photocurrent vs potential curve relating to an anodic film on Ta-85at.%Nb alloy, recorded by irradiating the electrode in 0.1 M $LiClO_4$ propylene carbonate at λ = 280 nm.

In Fig. 6.15 we show the schematic picture of the energetic levels at the oxide/organic interface relating to anodic oxide grown on Ta-85at.%Nb until 10V vs. Ag/AgCl, potentiodinamically at 10 mV/sec in 0.1 M NaOH; band gap and flat band potential are estimated by photocurrent Spectrum (see fig. 6.13) and photocharacteristic (see fig. 6.14) as for Nb_2O_5. We locates the conduction band mobility edge of oxide around 0.37 eV above U_{fb} in agreement with ref. [4.1].

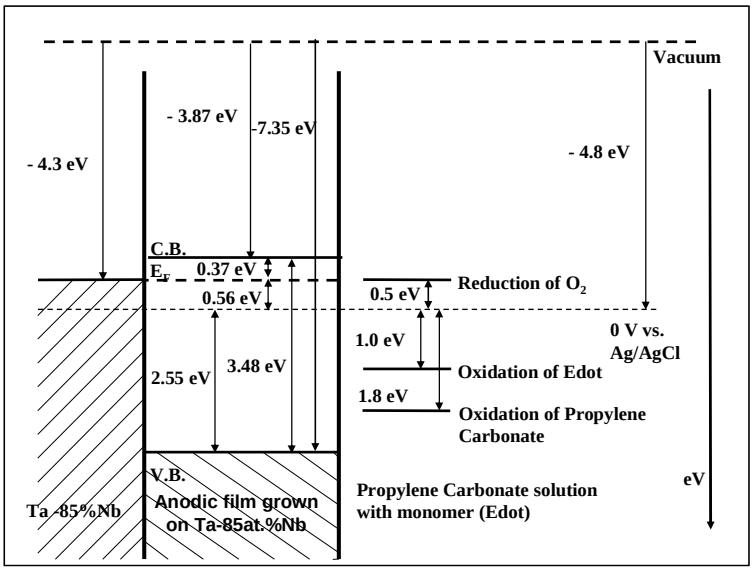

Fig. 6.15 Schematic picture of the energetic levels at the Ta-85at.%Nb/anodic oxide/organic solution (containing Edot) interface. The reported oxygen reduction potential is from Ref. [6.9]

As for Nb_2O_5, according to the energetics of the oxide/electrolyte interface of Fig. 6.15, it is evident that the oxidation of Edot on this anodic oxide is thermodynamically possible.

In fig. 6.16 we report the growth curve during photo-electropolymerization of Edot on anodic oxide grown on Ta-85at.%Nb. As in Fig. 6.9a, during the early stages of photoelectrodeposition I_{ph} decreases almost exponentially as a function of

the circulated charge, i.e. of polymer layer thickness. The exponential fitting of the curve allows estimating a PEDOT light absorption coefficient, α, very close to that estimated from Fig. 6.9b.

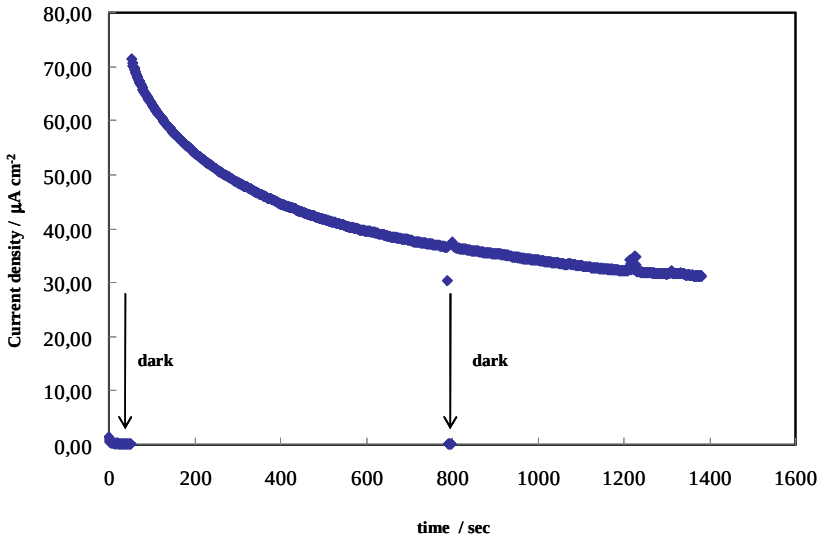

Fig. 6.16 Current density vs time recorded by polarizing anodic oxide grown on Ta-85at.%Nb (U_f = 10 V vs. Ag/AgCl) at 3V (Ag/AgCl) in 0.1 M $LiClO_4$ propylene carbonate solution containing 0.04M Edot under constant irradiating wavelength (λ = 310 nm).

The occurrence of photo-electrochemical polymerization was confirmed by SEM analysis (see micrographs of fig. 6.17).

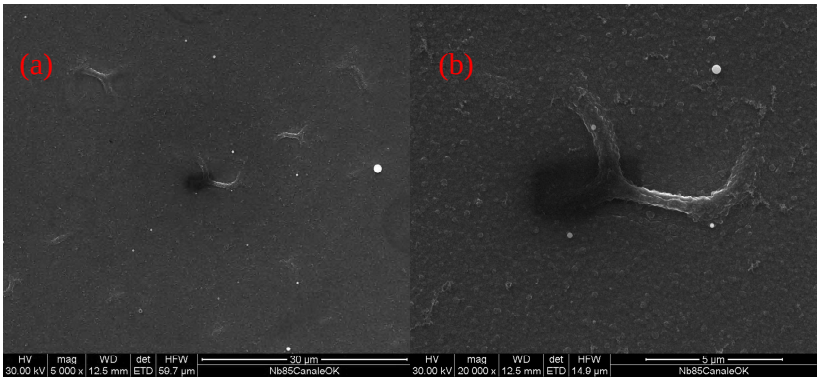

Fig. 6.17 SEM micrographs relating to PEDOT (solution-side) photoelectrochemically grown on anodic oxide on Ta-85at.%Nb.

The morphologies of Fig. 6.17 are similar to those of PEDOT photoelectrochemically grown on Nb_2O_5 (see Fig. 6.10 a).

6.5 Photo-electrodeposition and characterization of PEDOT on anodic films on magnetron sputtered Ti-6at.%Si alloys.

In Fig. 6.18a the formation voltage vs. time curve recorded during the anodizing process is reported. According to the high field mechanism (see chapter 5 and ref. [5.8-5.9]) a constant slope, $\frac{dV}{dt}$, is expected:

$$\frac{dV}{dt} = \frac{jE_dM}{zF\rho} \qquad 6.7$$

in which j is the measured current density, M is the molecular weight of the growing oxide, z the number of electrons circulating per mole of formed oxide, F the Faraday constant, ρ the film density and E_d is the electric field strength across the

growing layer. It is important to mention that a constant $\frac{dV}{dt}$ suggests that no breakdown phenomena occur during the film growth, in contrast to the behaviour of pure Ti [5.8]. From eq. 6.7 and assuming ρ = 3.7 g cm^{-3} (according to ref. [5.9]), E_d = 5.35 MV cm^{-1} can be estimated, corresponding to an anodizing ratio of ~ 19 Å V^{-1}. Thus, assuming an equilibrium potential for Ti oxidation to TiO_2 of ~ - 1.2 V (SHE) [3.12], formation voltages of 10 V and 50 V (vs. cathode) correspond to thickness of ~ 20 nm and ~ 100 nm, respectively in order to fabricate two OFETs with a bottom-gate/top-contact.

In Fig. 6.18b we report the capacitance vs. potential curves recorded in 1M H_3PO_4 solution superimposing to the continuous voltage a small alternative signal (v_{ac} = 10 mV) at f = 1 kHz. The measured capacitances were significantly influenced by the formation voltage, i.e. film thickness. As expected a lower value was measured for the thickest oxide but, more importantly, C resulted to increase by polarizing the 10 V anodic film toward the cathodic direction, as typical of *n*-type semiconducting material, while was almost potential independent for 50 V oxide, as typical of insulating material (see section 5.3.2 and ref. [6.6]).

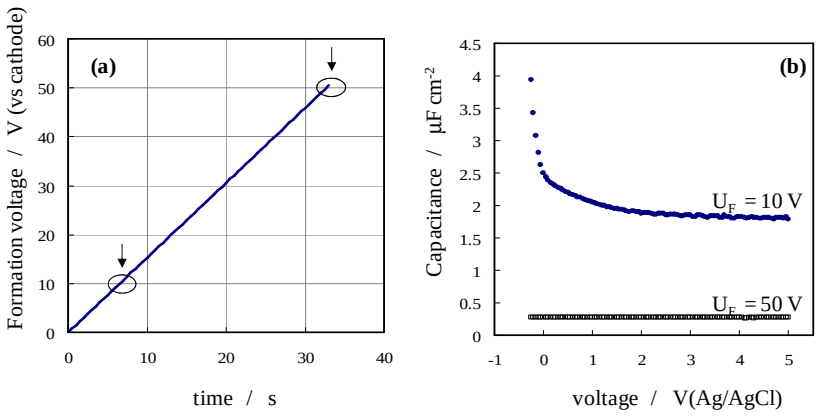

Fig. 6.18 a) Formation voltage vs. time curve recorded during the anodizing of Ti-6at%Si at 5 mA cm^{-2} in 1 M H_3PO_4. b) Capacitance vs. polarizing voltage curves relating to 10 V and 50 V anodic films. Sol: 1 M H_3PO_4, *vac* = 10 mV and f = 1 kHz.

In Fig. 6.19 we report the photocurrent versus wavelength curve at constant potential (photocurrent spectrum) relating to the anodic film grown to 50 V, recorded by polarizing the electrode at 8 V vs. Ag/AgCl in 0.1 M $LiClO_4$ in propylene carbonate. As shown in the inset of Fig. 6.19, an optical band gap of ~ 3.45 eV can be estimated by assuming non direct optical transitions. An almost coincident band gap was estimated for the 10 V film. These band gap values are in agreement with those estimated in aqueous solutions for oxide grown to several final formation voltages (see Chapter 5 and [ref. 5.10]).

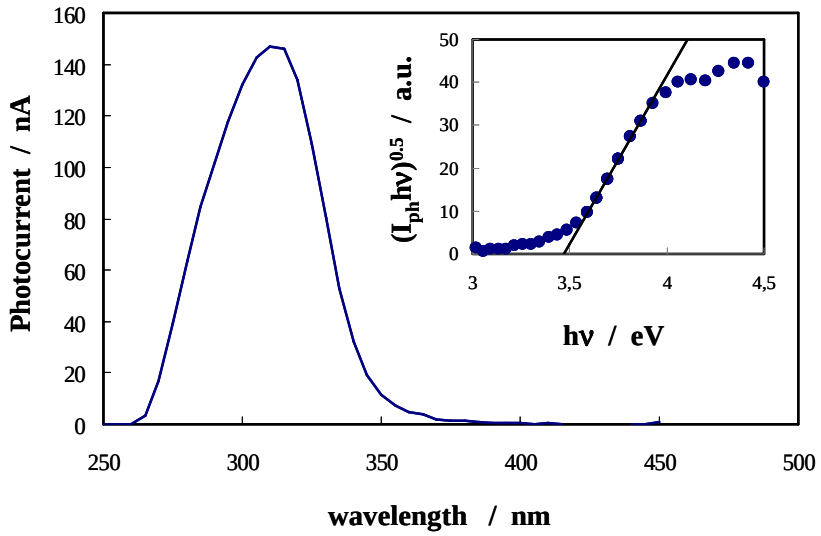

Fig. 6.19 Photocurrent spectrum relating to anodic film grown on Ti-6at%Si to 50 V at 5 mA/cm^2 in 1 M H_3PO_4, recorded by polarizing the electrode at 8 V in 0.1 M $LiClO_4$ in propylene carbonate. Inset: bandgap estimation by assuming non direct optical transitions.

In Fig. 6.20 we report the photocurrent vs potential curve (photocharacteristic) recorded by irradiating the anodic oxide grown on Ti-6at.%Si at λ = 340 nm in 0.1 M $LiClO_4$ PC electrolyte; an inversion of the photocurrent sign is revealed by moving the polarizing voltage towards the cathodic direction. This is typical on insulating material, for which both anodic and cathodic photocurrent can be

measured depending on the direction of the electric field, i.e. on the applied potential with respect to the flat band potential. The insulating behaviour of thick anodic films is in agreement with the experimental findings reported in Chapter 5 and ref. [5.10].

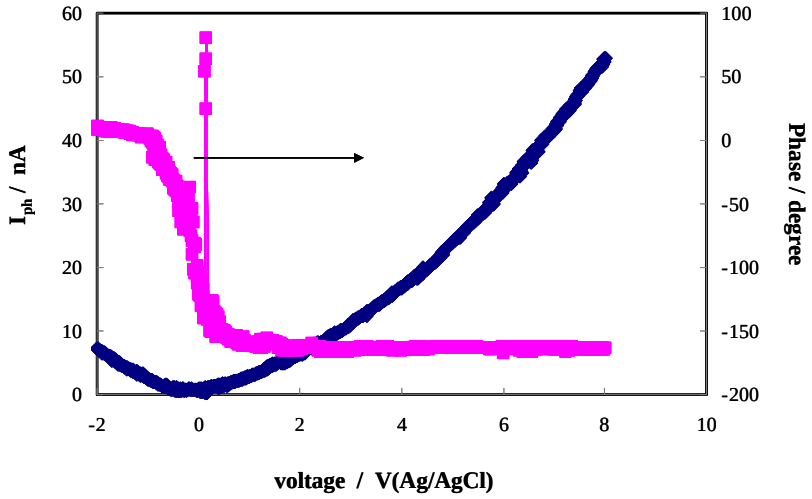

Fig. 6.20 Photocurrent vs potential curve relating to an anodic film on Ti-6at.%Si alloy, recorded by irradiating the electrode in 0.1M $LiClO_4$ propylene carbonate at λ = 320 nm.

The presence of cathodic photocurrent at potential more negative that U_{FB} allowed recording cathodic photocurrent spectra. In Fig. 6.21 we report the photocurrent vs wavelength curve recorded by polarizing the anodic oxide at -2 V vs. Ag/AgCl. As shown in the inset, an optical band gap of ~ 3.5 eV can be estimated for this oxide by extrapolating to zero the $(I_{ph}h\nu)^{0.5}$ vs $h\nu$ plot. This value is close to that estimated from anodic photocurrent spectrum of Fig. 6.19.

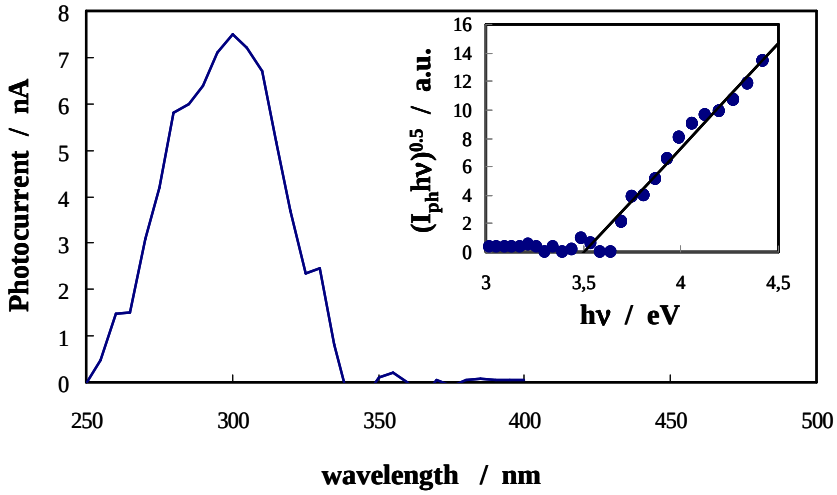

Fig. 6.21 Photocurrent spectrum relating to anodic film grown on Ti-6at%Si to 50 V at 5 mA/cm^2 in 1 M H_3PO_4, recorded by polarizing the electrode at - 2 V in 0.1 M $LiClO_4$ in propylene carbonate. Inset: bandgap estimation by assuming non direct optical transitions.

For insulating layers the inversion photocurrent potential can be assumed as a proxy of the flat band potential, which results (see Fig. 6.20) to be U_{FB} ~ - 0.2 vs Ag/AgCl. If we assume that the organic electrolyte is equivalent to an aqueous solution at the titanium oxide isoelectric point (pH_{pzc} ~ 5.8, see ref. [3.21]), this value compares well with the U_{FB} reported in chapter 5 estimated in 0.1 M ammonium biborate electrolyte (pH ~ 9). Knowing U_{FB}, locating the conduction band mobility edge of oxide at ~ 0.5 eV above U_{FB} (see Chapter 5 and ref. [5.10]) and knowing the band gap, the energy level of the valence band edge of anodic film on Ti-6at.%Si can be located at around 2.78 eV below the reference electrode, i.e. at ~ 0.98 eV below the oxidation potential of propylene carbonate. Thus, anodic photocurrent can be sustained by photo-electrochemical oxidation of the solvent in Edot free solution, while cathodic photocurrent is associated to O_2 reduction (see the energetic sketch of Fig. 6.22).

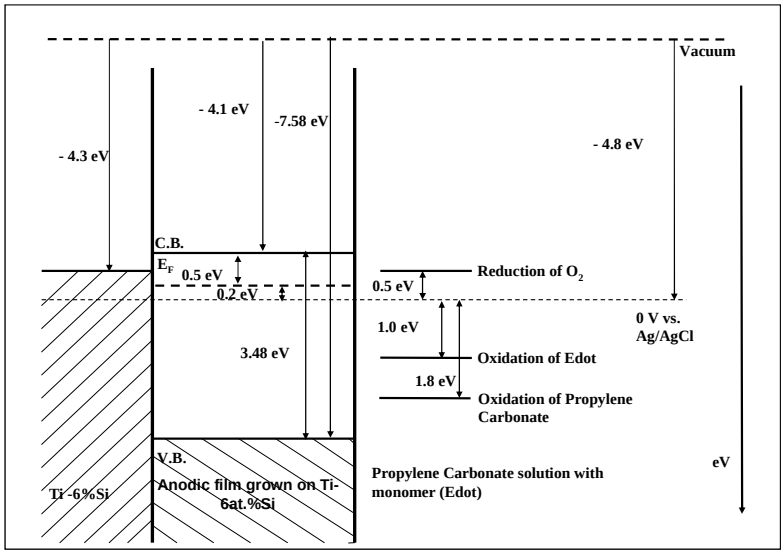

Fig. 6.22 Schematic picture of the energetic levels at the Ti-6at.%Si/anodic oxide/organic solution (containing Edot) interface. The reported oxygen reduction potential is from Ref. [6.9]

In Fig. 6.23 we report the current vs. time curve recorded under irradiation (λ = 320 nm) by polarizing the anodic oxide grown on Ti-6at.%Si at U_E = 8 V (Ag/AgCl), in 0.1 M $LiClO_4$ PC solution containing 0.04 M EDOT. By irradiating the anodic oxide surface with photon energy higher than the band gap of the anodic film (λ = 320 nm, i.e. 3.87 eV), the growth of polymer occurred according to photo-electropolymeric reactions above reported (see eqs. 6.5). The dependence of current on time is very similar to that already observed during the photoelectrochemical polymeriazation of Edot on anodic oxides on Nb (see Fig. 6.9) and Ta-85at.%Nb (see Fig. 6.16).

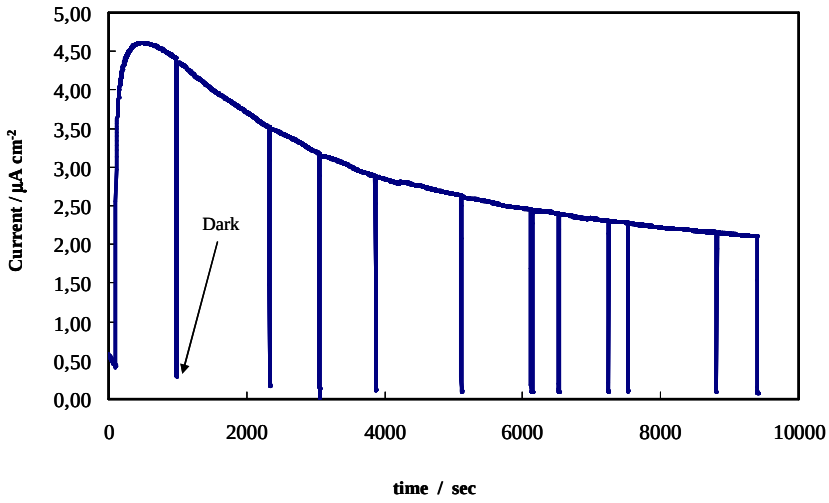

Fig. 6.23 Current density vs time recorded by polarizing anodic oxide grown on Ti-6at.%Si (U_f = 50 V) at 8V (Ag/AgCl) in 0.1M $LiClO_4$ propylene carbonate solution containing 0.04 M Edot under constant irradiating wavelength (λ = 320 nm).

According to the energetics of the oxide/electrolyte interface of Fig. 6.22, it is evident that both the oxidation of Edot and of PC are thermodynamically possible.

The control of the circulated charge allowed an estimation of polymer's thickness of roughly 200 nm.

A morphological study of PEDOT photoelectrochemically grown on anodic oxides on Ti-6at.%Si electrodes was carried out. The surface morphology is shown in Fig. 6.24a (solution-side) and Fig. 6.24b (oxide-side), while polymer, while polymer cross section of PEDOT is depicted in Fig. 6.24c. The morphologies in both cases are really different with respect to those evidenced for electrochemically grown polymer on gold (see section 6.3) but are similar with respect to those showed for photo-electrochemically grown polymer on anodic films (see section 6.4).

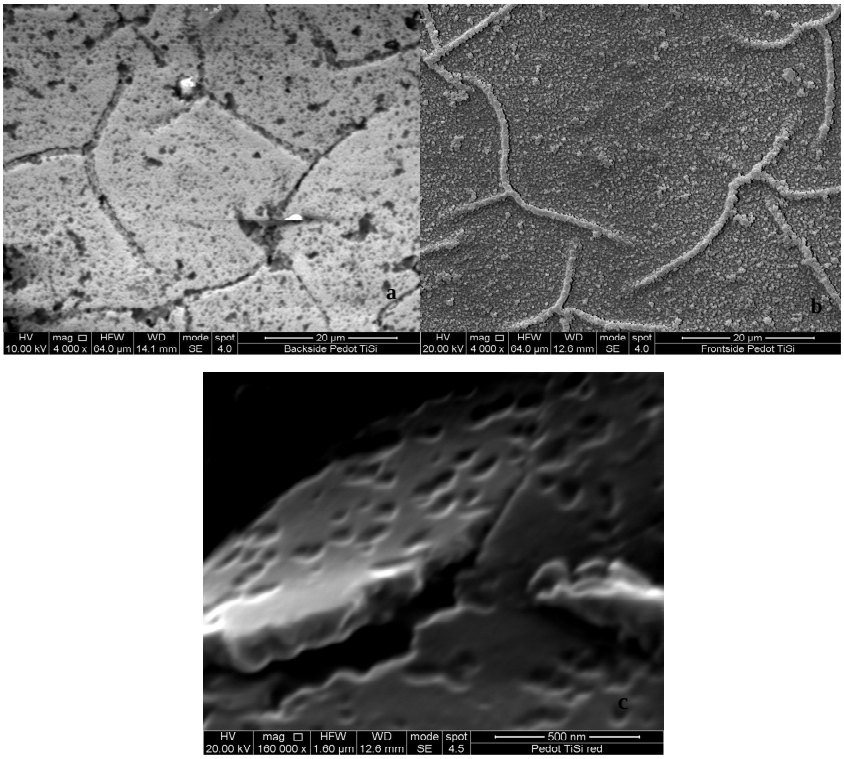

Figs. 6.24 SEM micrographs relating to PEDOT grown photoelectrochemically (λ = 320 nm) at Ue = 8V (Ag/AgCl) on anodic film on Ti-6at.%Si after circulation of ~ 60 mC cm^{-2}. (a) Oxide side morphology, (b) Solution-side surface morphologies and (c) cross section of polymer.

The as prepared PEDOT is in its metallic state, thus a reduction step is necessary to allow polymer de-doping, i.e. to bring PEDOT in its p-type semiconducting state. The redox potential for PEDOT reduction is at - 0.5 V vs Ag/AgCl in propylene carbonate, according to the results reported in section 6.3. Due to the large film thickness (i.e. high formation voltage), it was necessary to perform the de-doping process under strong cathodic polarization (- 3 V vs Ag/AgCl) in order to account for the potential drop across the insulating oxide.

In Fig. 6.25a we report the cathodic photocurrent spectrum of anodic oxide/PEDOT/solution junction recorded at - 3 V vs Ag/AgCl. A direct optical

transition at 1.78 eV (Fig. 6.25b) and an indirect one of ~ 1.46 eV (Fig. 6.25c) were determined; both values being very close to those estimated for PEDOT grown on gold electrode and on other anodic oxides (see section 6.3 and section 6.4). The photo-activity of PEDOT shows that the polymer is in its semiconducting behaviour and that de-doping process is occurred.

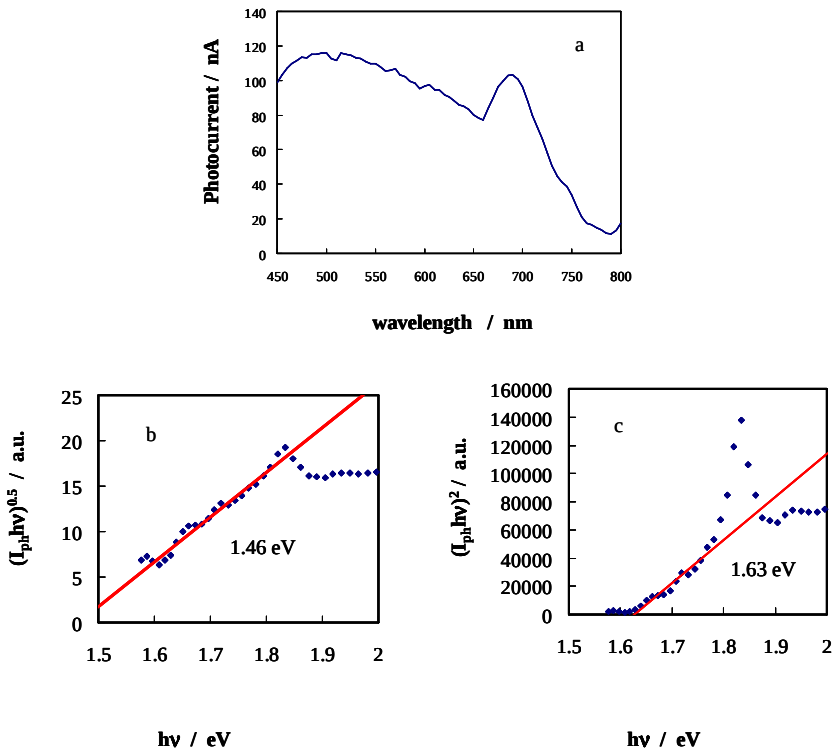

Fig. 6.25 (a) Raw cathodic photocurrent spectrum relating to PEDOT film electrochemically grown after circulation of ~ 60 mC cm^{-2} on anodic oxide of Ti-6at.%Si, recorded by polarizing electrode in 0.1 M $LiClO_4$ propylene carbonate at Ue = −3V (Ag/AgCl). Band gap estimate by assuming (b) non-direct and (c) direct optical transitions.

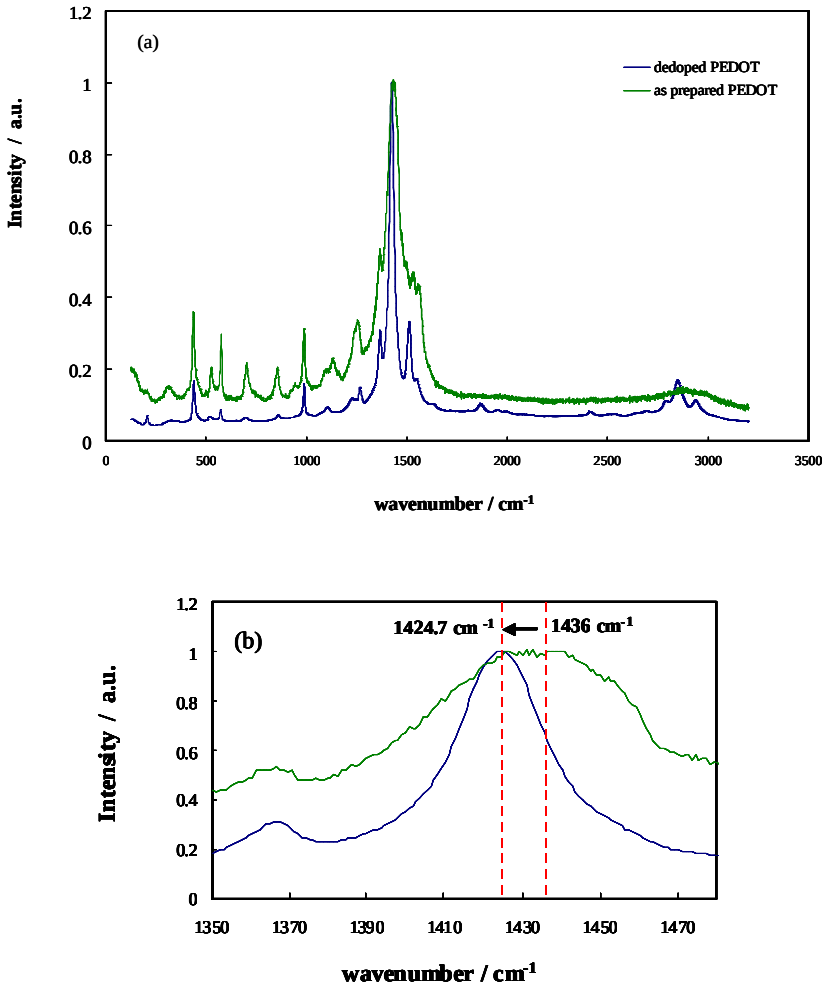

Fig. 6.26 a) Raman spectra relating to PEDOT photo-electrochemically grown (λ = 320 nm) at Ue = 8V (Ag/AgCl) on anodic film of Ti-6at.%Si, as prepared and after de-doping process. b) Magnification of Fig. (a).

The occurrence of de-doping process is also supported by the Raman analysis. In Fig. 6.26 we report the Raman Spectra relating to PEDOT soon after photoelectrodeposition and after occurrence of dedoping. According to ref. [6.22], a shift toward lower wavenumber of the symmetric Cα-Cβ bond mode is expected as a consequences of the dedoping process. As shown in the inset of Fig. 6.26, such band shifts from 1436 cm^{-1} for as prepared PEDOT to 1424.7 cm^{-1} for dedoped polymer. The latter value is higher than that reported in ref. [6.22], suggesting a not fully completed dedoping process.

6.5.1 Electronic characterizations in FET structure

Fig. 6.27 shows the I-V output characteristics of an OFET with a gate oxide fabricated by anodizing a Ti-6at%Si alloy to 10 V. The inset displays the bottom-gate/top-contact structure of the device.

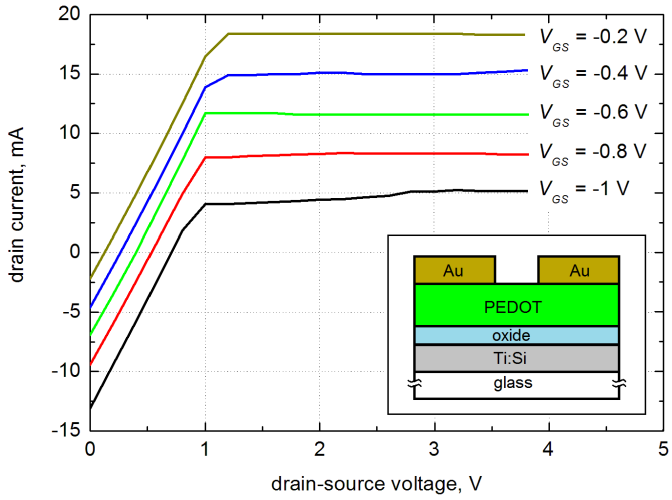

Fig. 6.27 I-V output characteristics of an OFET with a Ti94%-Si6% gate and 20 nm-thick oxide layer grown by anodization to 10 V. The inset shows the device structure.

The slope of each curve in the triode region did not change with the gate-source voltage V_{GS}, meaning that the channel resistance was not dependent on gate voltage. The behavior of the device is typical of an *n*-JFET. Furthermore, when the drain-source voltage V_{DS} equals 0 V, a negative current I_D flowed from drain to source and increased with $|V_{GS}|$. Clearly, the current at V_{DS} = 0 V was injected from the gate. This phenomenon can be explained considering that the 10 V anodic film behaves like n-type semiconductor, reminiscent of the TiO_2 behaviour (see chapter 5 and ref. [5.1]). Under negative bias, current can flow through the oxide due to a partial metallization of the film. The oxide performance was, in fact, improved by increasing the formation voltage to 50 V. Therefore, thick layers are reported to behave like insulating materials, as detailed described elsewhere (see chapter 5 and ref. [5.1] and section 6.5). Another device was then fabricated without changing any other parameter but the gate oxide thickness, and its *I-V* output curves are shown in Fig. 6.28. The inset shows the transfer characteristic calculated for V_{DS} = 4 V and fitted with a quadratic curve.

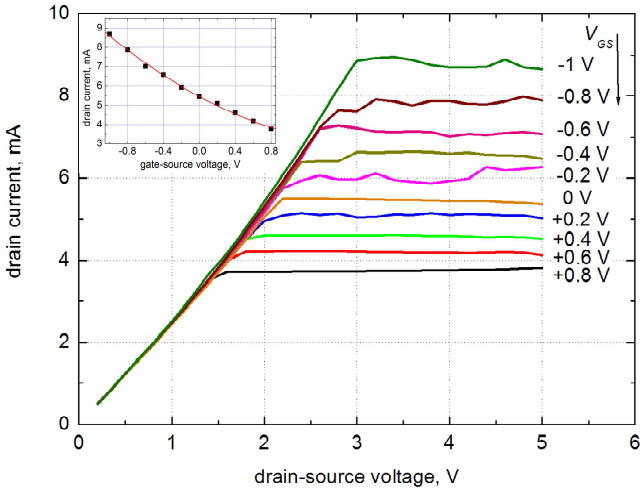

Fig. 6.28 I-V output characteristics of an OFET with a Ti94%-Si6% gate and 100 nm-thick oxide layer grown by anodization to 50 V. Inset: Transfer characteristic (I_D-V_{GS}) calculated for V_{DS} = 4 V and fitted with a quadratic curve.

Unlike the measurements reported in Fig. 6.27, it is possible to see that each curve crosses the origin of the *x*-*y* axes, meaning that the drain current is zero even when V_{DS} = 0. Consequently, no current was injected from the gate and the device behaved as a *p*-MOSFET. This improvement of the device may be then ascribed to the insulating character of the oxide.

Measurements reported in Fig. 6.28 confirmed that the OFET worked as a depletion device, due to an incomplete de-doping of the polymer. The threshold voltage V_t was calculated to be 2.7 V.

The slope of the characteristics in the triode region did not change with V_{GS}. Carrier mobility μ can be calculated from the expression of the drain current in the pinch-off region:

$$I_D = \varepsilon_{ox} \frac{W\mu}{2Ld_{ox}} (V_{GS} - V_t)^2 \qquad 6.8$$

where the oxide dielectric constant is $\varepsilon_{ox} = \varepsilon_0 \varepsilon$ with ε = 31 (see Chapter 5), the channel length is L ~ 150 μm, the channel width is W = 4.5 mm, and the oxide thickness is d_{ox} ~ 100 nm. After calculation, a value of 120 $cm^2/(Vs)$ was obtained. In order to find a model able to explain the behavior of the fabricated device, this value of mobility was substituted in the expression of drain current in the triode region:

$$I_D = \varepsilon_{ox} \frac{W\mu}{2Ld_{ox}} \left[2(V_{GS} - V_t)V_{DS} - V_{DS}^2\right] \qquad 6.9$$

The plot of the eq. 6.9 for different values of V_{GS} was a bundle of parabolas passing through the origin. In the triode region, the parabolas did not fit the measured curves, as shown in Fig. 6.29.

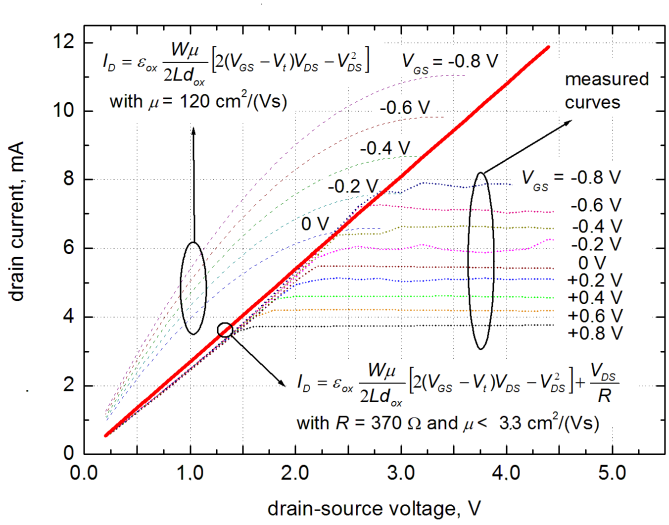

Fig. 6.29 Comparison between measured curves in the triode region and the theoretical model for the device with 100 nm-thick oxide layer. The standard MOSFET relations, plotted for an extrapolated mobility of 120 cm2/(Vs), lead to a bundle of parabolas which do not fit the experimental data. A proper fitting is obtained by adding a linear term to the standard MOSFET relations for μ ≤ 3.3 cm2/(Vs) and R = 370 .

Actually, the value of mobility calculated by eq. 6.8 was not the real one [6.23], since it was affected by the presence of ohmic currents flowing through the more conductive polymer layer, which are present in the film due to a de-doping process, i.e. polymer reduction, not uniform along the film thickness.

A more reasonable calculation should take into account these currents by adding an ohmic term to the expression 6.9:

$$I_D = \varepsilon_{\text{ox}} \frac{W\mu}{2Ld_{\text{ox}}}\left[2(V_{GS} - V_t)V_{DS} - V_{DS}^2\right] + \frac{V_{DS}}{R} \qquad 6.10$$

where R is the measured resistance between source and drain contacts when V_{GS} = 0 V. A value of R ~ 300 Ω was obtained by a two-probe resistance measurement.

Since in the triode region all the characteristics curves of the device were overlapped and were approximately linear, it is evident that the second term in the expression 6.10 is predominant with respect to the first one. By considering that the second term was at least one order of magnitude higher than the first one, it was possible to estimate an upper limit for the mobility of 3.3 $cm^2/(Vs)$, considerably lower than the one calculated by the expression 6.8. Assuming $\mu \leq 3.3$ $cm^2/(Vs)$, more physically reasonable [6.23], one could find a proper value for the resistance R to fit the experimental curves (in the triode region) with the theoretical model expressed by the eq. 6.10. As reported in Fig. 6.29, a suitable fitting was obtained for $R = 370\ \Omega$.

6.6 Conclusions

A photoelectrochemical method for the electropolymerization of Edot on wide band gap anodic anodic films on magnetron sputtered Nb, magnetron sputtered Ta-85at.%Nb alloy and magnetron sputtered Ti-6at.%Si was successfully realized. A SEM characterization was performed on both electrochemically and photoelectrochemically grown polymers for comparing their morphological features.

Soon after fabrication polymers were dedoped by a reduction step in order to change their conductivity type (from metallic to p-type semiconductor). The occurrence of dedoping process was confirmed by Raman analysis.

A photoelectrochemical investigation was performed in order to get information on the solid state properties (band gap, flat band potential, conductivity type) of the polymer and, thus, on the energetics of the metal/oxide/electrolyte interface. The comparison of the photoelectrochemical properties of PEDOT prepared on anodic oxides with those of the polymer electrochemically grown on gold did not evidence appreciable differences.

Finally, output transistor characteristics were recorded in order to test the performance of the junctions in the IOFET structure.

Devices performances resulted to depend on oxide electronic properties, which are in turn influenced by the oxide composition and formation voltage. A transistoric effect was evidenced when 50 V anodic film on Ti-6at.%Si was employed as dielectric. However, problems relating to a not uniform polymer de-doping were

modelled in order to trace the route for further improvements in the electrochemical fabrication process of OFETs.

The described method allowing for the polymerization of conducting polymers on non conducting substrates can play an important role for the fabrication of large area metal/oxide/conducting polymer composites not only for solid state capacitors but also, more generally, for organic/inorganic electronic devices.

REFERENCES

[6.1] K. Ueno, L. Dominey, H. Uchi and R. S. Alwitt, Journal of The Surface Finishing Society of Japan, 60, (2009) 179.

[6.2] F. Di Quarto, V. Figà, P. Bocchetta, M. Santamaria, Electrochem. Solid State Letters, 10, (2007) H305.

[6.3] F. Di Franco, P. Bocchetta, M. Mosca, C. Calì, M. Santamaria, F. Di Quarto, Electrochimica Acta, 56, (2010), 737.

[6.4] C. D. Dimitrakopoulos and D. J. Mascaro, *IBM J. Res. Dev.*, 45, (2001), 11.

[6.5] F. Di Franco, P. Bocchetta, M. Santamaria, and F. D. Quarto, *Electrochim. Acta*, 56, (2010), 737.

[6.6] M. Mosca, R. Macaluso, G. Randazzo, M. Di Bella, F. Caruso, C. Calì, F. Di Franco, M. Santamaria, F. Di Quarto, ECS Solid State Letters, 2, (11), (2013), N205.

[6.7] 5. F. Di Franco, P. Bocchetta, C. Calì, M. Mosca, M. Santamaria, and F. Di Quarto, *J. Electrochem. Soc*., 158, (2011), H50.

[6.8] M. Dietrich, J. Heinze, G. Heywang and F. Jonas, Journal of Electroanalytical Chemistry, 369, (1994), 87.

[6.9] A J. Bard, L. R. Faulkner, Electrochemical Methods: fundamentals and applications, John Wiley & Sons, (2000).

[6.10] B.L. Funt and A.F. Diaz, Organic Electrochemistry: an Introduction and a Guide, p. 1337, Marcel Dekker, New York (1991).

[6.11] E.M. Genies, G. Bidan and A.F. Diaz, J. Electroanal. Chem.,149, (1983) 101.

[6.12] H. Randriamahazaka, V. Noel and C. Chevrot, Journal of Electroanalytical Chemistry, 472, (1999), 103.

[6.13] A.L. Melato, A.S. Viana, L.M. Abrantes, Electrochimica Acta, 54, (2008), 590.

[6.14] R.J. Waltman, J. Bargon and A.F. Diaz, J. Phys. Chem., 87**,** (1983), 1463.

[6.15] S. Patra, K. Barai, N. Munichandraiah, Synth. Met., 158, (2008), 430.

[6.16] R. Kiefer, G.A. Bowmaker, R.P. Cooney, P.A. Kilmartin, J. Travas-Sejdic. El. Acta, 53, (2008), 2593.

[6.17] M. Kertesz, C.H. Choi and S. Yang, Chem. Rev., 105, (2005), 3448.

[6.18] S.S. Zade and M. Bendikov, Organic Letters, 8**,** (2006), 5243.

[6.19] Z.V. Vardeny and X. Wei, in Handbook of Conducting Polymers, 2nd ed., T. E. Skotheim, R. L. Elsenbauner and J. R. Reynolds editors, p. 639 Marcell Decker, New York (1998).

[6.20] M. T. Lloyd, Y-J Lee, R. J. Davis, E. Fang, R. M. Fleming, J. W. P. Hsu, R. J. Kline, M. F. Toney, J. of Phys. Chem. Letters, 113, (2009), 17608.

[6.21] M. J. Miles, W. T. Smith, J.S. Shapiro, Polymer, 41, (2000), 3349.

[6.22] W.W. Chiu, J. Travas -Sejdic , R. P. Cooney and G. A. Bowmaker, J. Raman Spectrosc., 37, *(*2006), 1354.

[6.23] Y. Harima, T. Eguchi, and K. Yamashita, Synthetic Met., 95, (1998), 69.

7 Summary, conclusions and perspectives

In this PhD work we studied the possibility to use a fully electrochemical route to fabricate metal/oxide/conducting polymer junctions to be employed in several electronic devices such as electrolytic capacitors and inorganic-organic thin field effect transistors.

The first part of the research activity was devoted to the fabrication and characterization of high k oxides with good dielectric properties. We selected anodizing as versatile low temperature wet electrochemical process to grow anodic films of valve metals and valve metal alloys (more specifically, magnetron sputtered Nb-Ta, Nb-Al, Ti-Si alloys). The selection of the partner metals and of their relative amount in the base alloys as well as the choice of the anodizing conditions allowed for tuning the solid state properties of the oxides

All the three listed systems, i.e. Nb-Ta, Nb-Al and Ti-Si mixed oxides, were characterized by in situ electrochemical, photo-electrochemical and impedance measurements and by ex situ techniques, such as Glow Discharge Optical Emission Spectroscopy, X-ray Photoelectron Spectroscopy and Rutherford Back Scattering, in order to get information on the solid state properties (band gap, flat band potential, conductivity type, dielectric constant) of the mixed oxides as a function of the base alloy composition and anodizing conditions (formation voltage, growth rate, anodizing solution). Such information, which are of primarily importance in view of possible application of the oxides in electronic devices, resulted to be very useful to assess some theoretical aspects relating to the dependence of the band gap of mixed oxides on their composition as well as to influence of the amorphous nature of the film on their photo-electrochemical behaviour and on their impedance.

In the second part of this work, the deep knowledge of the solid state properties of the investigated oxides was used to design a photoelectrochemical process able to allow the electro-polymerization of Edot on a not conducting substrate (more specifically anodic films on magnetron sputtered Nb, Ta-85at.%Nb and Ti-6at.%Si alloys). Photocurrent Spectroscopy was employed to study the optical properties of metal/anodic oxide/PEDOT/electrolyte interface in a large range of potential, while

Scanning Electron Microscopy was used to get information on the morphology of PEDOT. A Raman analysis also performed to study the de-doping process of the polymer. The features of the photo-electrochemically grown polymer were also compared with those showed by PEDOT electro-polymerized on gold conducting substrate.

In order to test the fabricated junctions in Organic/Inorganic Field Effect Transistor (FET), PEDOT was electrochemically de-doped (i.e. reduced) to work as p-type semiconducting material. In the case of anodic film on Ti-6at.%Si, the electrical characterization revealed a transistoric effect, and its performance was studied as a function of thickness and solid state properties of the anodic oxide. By modeling the current-voltage output curves, we estimated some typical parameters of the device, such as threshold voltage, V_t, and carrier mobility, μ. Since μ was found to be higher than the value usually reported in the literature for PEDOT, we suggested as possible explanation the occurrence of a not uniform polymer de-doping process, which induces the formation of more conductive paths across the film and, thus, the presence of high ohmic currents.

The research activity developed during this three years PhD work shows that we were able to accomplish the main aim of this project, as stated in the title. However, it leaves a few open questions on the possible optimization of both fabrication process and devices' performance. More specifically, further tests can be done with conducting polymers other than PEDOT. In this case, the knowledge of the energetics of the metal/oxide/electrolyte interface will guide in the selection of monomers, whose oxidation potential must be less noble than the oxide valence band edge. Finally, it will be necessary to better design the de-doping process, which requires a strong cathodic polarization, that can cause oxide litiation and consequent oxide electric properties degradation. Work is now in progress to design a photoelectrochemical reduction step, that can induce polymer de-doping under low cathodic overvoltage.

Scientific Output

Publications in International Journals

1. F. Di Franco, G. Zampardi, M. Santamaria, F. Di Quarto, H. Habazaki, *Characterization of the Solid State Properties of Anodic Oxides on Ta-Nb Alloys as a Function of the Anodizing Conditions*, ECS Transaction, Volume 41, Issue 3, (2011) , 293-310, Boston, MA Physics and Technology of High-k Materials 9, Editor(s): S. Kar, M. Houssa, S. Van Elshocht, D. Misra, K. Kita

2. F. Di Franco, G. Zampardi, M. Santamaria, F. Di Quarto, H. Habazaki, *Characterization of the Solid State Properties of Anodic Oxides on Magnetron Sputtered Ta, Nb and Ta-Nb Alloys*, Journal of The Electrochemical Society, 159, (2012), C33-C39.

3. F. Di Franco, M. Santamaria, F. Di Quarto, E. Tsuji, H. Habazaki, *The Influence of Nitrogen Incorporation on the Optical Properties of Anodic* Ta_2O_5, Electrochimica Acta, 59 , (2012), 382-386.

4. M. Santamaria, F. Di Franco, F. Di Quarto, P. Skeldon and G.E. Thompson, *Tailoring of the Solid State Properties of Al-Nb Mixed Oxides: a Photoelectrochemical Study*, Journal of Physical Chemistry C, 117, (2013), 4201-4210.

5. F. Di Quarto, F. Di Franco, C. Monarca, M. Santamaria, H. Habazaki, *Photoelectrochemical Characterization of Amorphous Anodic Films on Ti-6at.%Si*, Electrochimica Acta, 110, (2013), 517-525.

6. F. Di Franco, M. Santamaria, F. Di Quarto, F. La Mantia, A. I. De Sà, C. M. Rangel, *Dielectric Properties of Al-Nb Amorphous mixed oxides*, ECS Journal of Solid State Science and Technology, 2, (11), (2013), N205-N210.

7. R. Macaluso, M. Mosca, C. Calì, F. Di Franco, M. Santamaria, F. Di Quarto, J.L. Reverchon, *Erroneous p-type assignment by Hall effect measurements in annealed ZnO films grown on InP substrate*, Journal of Applied Physics, 113, (2013), art. no. 164508.

8. M. Mosca, R. Macaluso, G. Randazzo, M. Di Bella, F. Caruso, C. Calì, F. Di Franco, M. Santamaria, F. Di Quarto, *Anodized Ti-Si alloy as gate oxide of electrochemically-fabricated organic field-effect transistors*, ECS Solid State Letters, 3, (1), (2014), P7-P9.

National Conference Contributions

1. F. Di Franco **(Presenting author)**, H. Habazaki, M. Santamaria, F. Di Quarto, *Tuning of the Optical and Dielectric Properties of Anodic Films on sputtered*

deposited Ta-Nb Alloys, XXIV Congresso Nazionale della Società Chimica Italiana Divisione di Elettrochimica September 11 - 16, Lecce, 2011 (Oral Communication).

2. F. Di Franco (**Presenting Author**), M. Santamaria, F. Di Quarto, R. Macaluso, M. Mosca, C. Calì, *Electrochemical Fabrication of High K Niobium-Tantalum Mixed Oxides/Poly 3-4 Ethylene Dioxythiophene Junctions*, GEIERA 2012, June 17 – 22, 2012, Santa Marina Salina, Messina, Italy. (Oral Communication).

3. F. Di Quarto, F. Di Franco, M. Santamaria, *Spettroscopia di fotocorrente e ammettenza differenziale per lo studio delle proprietà elettroniche e di stato solido di film passivi e ossidi anodici di interesse tecnologico*, Giornate Nazionali Sulla Corrosione e Protezione (GNC 2013) July 10 - 12, 2013, Napoli, Italia. (Plenary Lecture).

4. F. Di Franco (**Presenting Author**), M. Santamaria, F. Di Quarto, G. Randazzo, R. Macaluso, M. Mosca, C. Calì, *Photo-Electrochemical deposition of Poly-3,4 Ethylenedioxythiophene on Anodic Films on Ti-Si Alloys*, GEIERA 2013, September, 22 - 27, 2013, Pavia, Italy. (Poster Communication).

5. G. Conigliaro, M. Santamaria, F. Di Franco, F. Di Quarto, *Redshift of absorption threshold of TiO_2 Nanotubes due to Cu_2O electrodeposition*, GEIERA 2013, September, 22 – 27, 2013, Pavia, Italy. (Oral Communication).

6. F. Di Quarto, F. Di Franco, C. Monarca, M. Santamaria, M.V. Diamanti, MP. Pedeferri, *Physicochemical Characterization of anodic film on Titanium prepared by Pedeferri's Treatment*, Pietro Pedeferri e la scuola di corrosione e protezione dei materiali al Politecnico di Milano**,** Milano, September 26 - 27, 2013. (Invited Lecture)

International Conference Contributions

1. F. Di Franco **(Presenting author)**, H. Habazaki, M. Santamaria and F. Di Quarto, *The influence of electrolyte composition on the solid state properties of anodic films on Ta-Nb alloys*, 10th International Symposium on the Passivation of Metals and Semi-Conductors and the Properties of Thin Oxide Layers April 10 - 14, Florianopolis, Brazil, 2011 (Oral Communication)

2. F. Di Franco, G. Zampardi, M. Santamaria, F. Di Quarto and H. Habazaki, *Characterization of the Solid State Properties of Anodic Oxides on Ta-Nb Alloys as a Function of the Anodizing Conditions*,
220th ECS Meeting Boston October 9 - 14, USA, 2011 (Oral Communication)

3. F. Di Quarto, M. Santamaria, F. Di Franco, P. Skeldon, G. E. Thompson, C. M. Rangel, *The Influence of Composition in Determining the Solid State Properties of*

Al Mixed Oxides, VI International Symposium on Aluminium Surface Science and Technology May 27 – 31, 2012, Sorrento, Italy. (Oral Communication)

4. F. Di Quarto, F. Di Franco, M. Santamaria, *A Chemical Approach to the Estimate of the Optical Band Gap and Bowing Parameter in Mixed d,d-Metal Oxides*, Frontiers in Electronic Materials, Nature Conferences (Nature Materials) June 17-20, 2012, Aachen, Germany. (Poster Communication)

5.F. Di Franco (**Presenting Author**), M. Santamaria, F. Di Quarto, *Photoelectrochemical Polymerization of 3-4 Ethylene dioxythiophene on Anodic Niobium- Tantalum Mixed Oxides*, Corrosion - Aqueous Gordon Research Seminar, Corrosion Research: A Multidisciplinary Approach to Science July 7-8, 2012, Colby-Sawyer College New London, USA. (Poster Communication)

6. F. Di Franco (**Presenting Author**), M. Santamaria, F. Di Quarto, *Photoelectrochemical Polymerization of 3-4 Ethylene dioxythiophene on Anodic Niobium- Tantalum Mixed Oxides.* Corrosion – Aqueous Gordon Research Conference July 8-13, 2012, Colby-Sawyer College, New London, USA. (Poster Communication)

7. F. Di Quarto, F. Di Franco, M. Santamaria, M.V. Diamanti, C. Monarca, H. Habazaki, *Amorphous to Crystalline Transition in Anodic Oxide on Ti and Ti-Si alloys: A Photoelectrochemical Study*, The 63st annual meeting of International Society of Electrochemistry, Prague (Czech Republic) August 19 -24, 2012. (Oral Communication)

8. F. Di Franco (**Presenting Author**), M. Santamaria, F. Di Quarto, P. Skeldon, G.E. Thompson, C. M. Rangel, *Tuning of Solid-sate Properties of Al Mixed Oxides Grown on Sputter-deposited Al Alloys*, The 63st annual meeting of International Society of Electrochemistry, Prague (Czech Republic) August 19 -24, 2012. (Poster Communication)

9.F. Di Franco (**Presenting Author**), M. Santamaria, F. Di Quarto, R. Macaluso, M. Mosca, C. Calì, *Photoelectrochemical Polymerization of 3-4 Ethylenedioxythiophene on High k Niobium-Tantalum Mixed Oxides*, The 63st annual meeting of International Society of Electrochemistry, Prague (Czech Republic) August 19-24, 2012. (Oral Communication)

10. F. Di Franco (**Presenting Author**), M. Santamaria, F. Di Quarto, P. Skeldon, G.E. Thompson, C. M. Rangel, *Characterization of the Solid State Properties of Anodic Oxides Grown on Sputter-deposited Al-Nb Alloys*, 6th European Summer School on Electrochemical Engineering September 16-21, 2012, Zadar, Croatia. (Poster Communication).

11. F. Di Quarto, M. Santamaria, F. Di Franco, P. Skeldon, G.E. Thompson,C. Rangel; F. La Mantia, *Physico-chemical characterization of anodic films on sputter-deposited Al-Nb alloys.*
EUROCORR 2013 1-5 September, 2013, Estoril, Portugal. (Oral Communication).

12. F. Di Franco (**Presenting Author**), M. Santamaria, F. Di Quarto, G. Randazzo, R. Macaluso, M. Mosca, C. Calì, *Electrochemical fabrication of amorphous TiO_2/Poly-3,4 Ethylenedioxythiophene (PEDOT) hybrid structures for electronic devices*, The 64st annual meeting of International Society of Electrochemistry, Queretaro (Mexico) September 8 -13, 2013. (Oral Communication).

13. R. Macaluso, M. Mosca, C. Calì, F. Di Franco (**Presenting Author**), M. Santamaria, F. Di Quarto, and J.-L. Reverchon, *Electrochemical methods for carrier type identification of ZnO films grown by pulsed laser deposition on InP,* The 64st annual meeting of International Society of Electrochemistry, Queretaro (Mexico September 8-13, 2013. (Poster Communication).

14. G. Conigliaro, M. Santamaria, F. Di Franco (**Presenting Author**), F. Di Quarto, *Electrochemical fabrication of Cu_2O/TiO_2 nanotubes junctions with visible light photoactivity,* The 64st annual meeting of International Society of Electrochemistry, Queretaro (Mexico September 8 -13, 2013. (Poster Communication).

PhD Schools

1. GRICU PhD National School 2011, Santa Margherita di Pula (CA) 26 September-1 October 2011

2. Corrosion - Aqueous Gordon Research Seminar, Corrosion Research: A Multidisciplinary Approach to Science July 7-8, 2012 Colby-Sawyer College New London, USA.

3. 6th European Summer School on Electrochemical Engineering September 16-21, 2012, Zadar, Croatia.

4. GRICU PhD NATIONAL SCHOOL 2013 Free radical polymerization kinetics, statistical thermodynamics and engineering aspects and Advanced topics in sustainable Chemical Engineering. September 16 - 20, 2013, Salice Terme (PV), Italy.

Other activities

Visiting PhD Student in the *Zentrum für Elektrochemie of Ruhr-Universität Bochum (Bochum, Germany),* 22 June - 30 July 2013.